Oceanic Tide Maps and Spherical Harmonic Coefficients from Geosat Altimetry

D.E. Cartwright, R.D. Ray,
and B.V. Sanchez

July 1991

NASA

Oceanic Tide Maps and Spherical Harmonic Coefficients from Geosat Altimetry

D.E. Cartwright and R.D. Ray
ST Systems Corporation
Lanham, Maryland

B.V. Sanchez
Goddard Space Flight Center
Greenbelt, Maryland

Summary

This report presents maps and tables for the global ocean tides, 69°N to 68°S, derived from two years of Geosat altimetry. It supplements a paper by Cartwright and Ray which examines the energetics implied by the same data. Global maps of local and Greenwich admittance of the (altimetric) ocean tide, and maps of amplitude and Greenwich phase lag of the ocean tide are shown for M_2, S_2, N_2, O_1, and K_1. Larger scale maps of amplitude and phase are also shown for regional areas of special interest. Spherical harmonic coefficients of the ocean tide through degree and order 8 are tabulated for the six major constituents.

Contents

1   Introduction

The oceanic tide maps and spherical harmonic coefficients depicted or listed in this report were all derived from an improved (1990) analysis of two years of Geosat altimeter data, using techniques that are basically described in *Cartwright and Ray* (1990), a paper whose work was completed early 1989. The material herein forms a complement to a recent paper by the same authors (*Cartwright and Ray*, 1991), which examines the energetics of the ocean tides implicit in the maps and compares dissipation rates with those derived from recent gravimetric analyses of satellite orbits, such as *Marsh et al.* (1990). The two papers by Cartwright and Ray will be referred to here as CR90 and CR91, respectively.

CR90 was based on an analysis of the first year (1986–1987) of Geosat's Exact Repeat Mission (ERM), and was restricted to latitudes between 60°N and 60°S. CR91 and the present compilation result from an improved processing of about twice the amount of ERM data and include extensions into the following sea areas which were not well covered, if at all, in CR90:

(a) high latitude oceans between 68°N and S, including most parts of the Southern Ocean and of the Bering, Labrador, and Greenland-Norwegian Seas not permanently covered by ice;

(b) marginal tidal seas omitted from or only partially represented in CR90, including the Mediterranean, Caribbean, Okhotsk, and Japan Seas, the South and East China Seas, and the broader part of the North Sea.

2   Improved Data Analysis

Our basic analysis of the altimetric sea surface with retention of basin-scale wavelengths is similar to that described in CR90. Here we give only a brief summary. We work exclusively with the variable

$$\Delta\zeta(P_i, t) = \zeta(P_i, t) - \zeta(P_i, t + \tau), \tag{1}$$

where ζ is the estimate at time t of the sea surface elevation at a dense network of earth positions P_i, and $\tau \approx 34.1$ days is twice the orbital repeat period of Geosat. The elevations ζ are computed from the altimetry in

the usual manner, except that the computed "ocean tide" correction is not subtracted. The altimetric signal together with the "body tide" of the solid earth are subtracted from the orbital radius, computed to high precision, with corrections for ionospheric and tropospheric variability and for biases due to sea-state and atmospheric loading. The mission requirement that the Geosat groundtrack repeat to within ±1 km (*Born et al.*, 1987) ensures elimination in (1) of all geographically fixed variables, including principally the geoid (*Brenner et al.*, 1990). The constancy of τ to about 1 s imparts a simple constant transformation to every harmonic component of the tide, easily compensated for by imposing the same transformation on the tide-potential functions with which $\Delta\zeta$ is correlated.

Each estimate of ζ is associated on the data tape supplied by NOAA with a nominal "ocean tide" ζ_{model}, computed from the Naval Surface Weapons Center (NSWC) model due to *Schwiderski* (1983). Denoting by $\Delta\eta$ the sequence of height-differences similar to (1) but with ζ replaced by $\eta = \zeta - \zeta_{\text{model}}$, we approximate the major part of the residual orbital radius error by least-squares adjustment of the function

$$E(t) = A(t)\cos\omega t + B(t)\sin\omega t + C(t) \tag{2}$$

to long time-sequences of $\Delta\eta$ covering many orbital revolutions. In (2), ω is the orbital frequency, about 89.91 rad.day^{-1}, t is referred to an ascending node, and A, B, C are slowly varying, modulatory functions, expressed as low-order polynomials in t. Finally,

$$\Delta\zeta'(P_i, t) = \Delta\zeta(P_i, t) - E(t) \tag{3}$$

is analyzed for its intrinsic tidal signal in time and surface position. This signal (apart from uncorrected errors and oceanographic noise) is what is usually called the "ocean tide," slightly modified by elastic yielding of the sea bed, that is, by the "load tide" of the solid earth.

Our procedure for tidal analysis is unorthodox but accurate in its specification of the tidal potential and of a generally smooth admittance at every location. The interested reader is referred to CR90 for details. In brief, all values of $\Delta\zeta'(P_i, t)$ are collected in bins, 1° in latitude by $360/244 = 1.4754°$ in longitude, the latter being the spacing of adjacent ERM ground-tracks. Within each bin the data are convoluted with an array of 12 "orthotide" functions (*Groves and Reynolds*, 1975), 6 representing the diurnal part of the tide

2

potential, 6 representing the semidiurnal part. The resulting 12 coefficients define smooth complex admittances in frequency space to the two species of potential. Maps of real and imaginary parts of the admittance at specific frequencies, after some spatial smoothing between adjacent bins, define the spatial distribution of amplitude and phase of each Darwinian harmonic constitutent through use of the tables of *Cartwright and Edden* (1973).

For the present study, the following improvements to the above scheme were carried out:

1. The orbital radii were re-computed by Bruce Haines (University of Colorado) and Ron Williamson (STX) using the GEM-T2 gravity field, giving a global rms radial orbit error of about 49 cm (*Haines et al.*, 1990), much lower than many previous computations for the Geosat orbit. The 6-day arcs used defined limits of the continuous sequences of $\Delta\zeta$ (equation 1) which varied from 0.5 to 4.5 d without discontinuity. Over such time limits the modulatory functions A, B, C of our once-per-revolution correction E (equation 2) could be adequately parameterized by linear forms $A_0 + A_1 t$, etc.

2. The total time span of the data series in t, starting 1986 November 8.0 was increased from 341 d to 685 d plus the additional 34 d required to complete the definition of $\Delta\zeta$. This span includes a few short lacunae totalling 16 d but covers more than twice the alias-period (317 d) of the leading tide harmonic M_2 at each grid position. The scatter of all tide parameters about smooth variations in longitude were thereby demonstrably reduced by a factor of about 1.5.

   Figures 1 and 2 illustrate this reduction in scatter for the particular case of the quadrature component of the N_2 tide along a 1° zonal strip. Random scatter is most notably reduced in the quiet Pacific sector, 170° 270°, but also in the noisy region of the Agulhas current system, 15° 30°. An obvious outlier in the western South Atlantic at 317° was replaced later by interpolation between adjacent data.

3. A number of important altimeter corrections were improved, as follows:

   (a) We used an improved empirical formula for sea-state bias, involving both wave height and wind speed (*Ray and Koblinsky*, 1991).

3
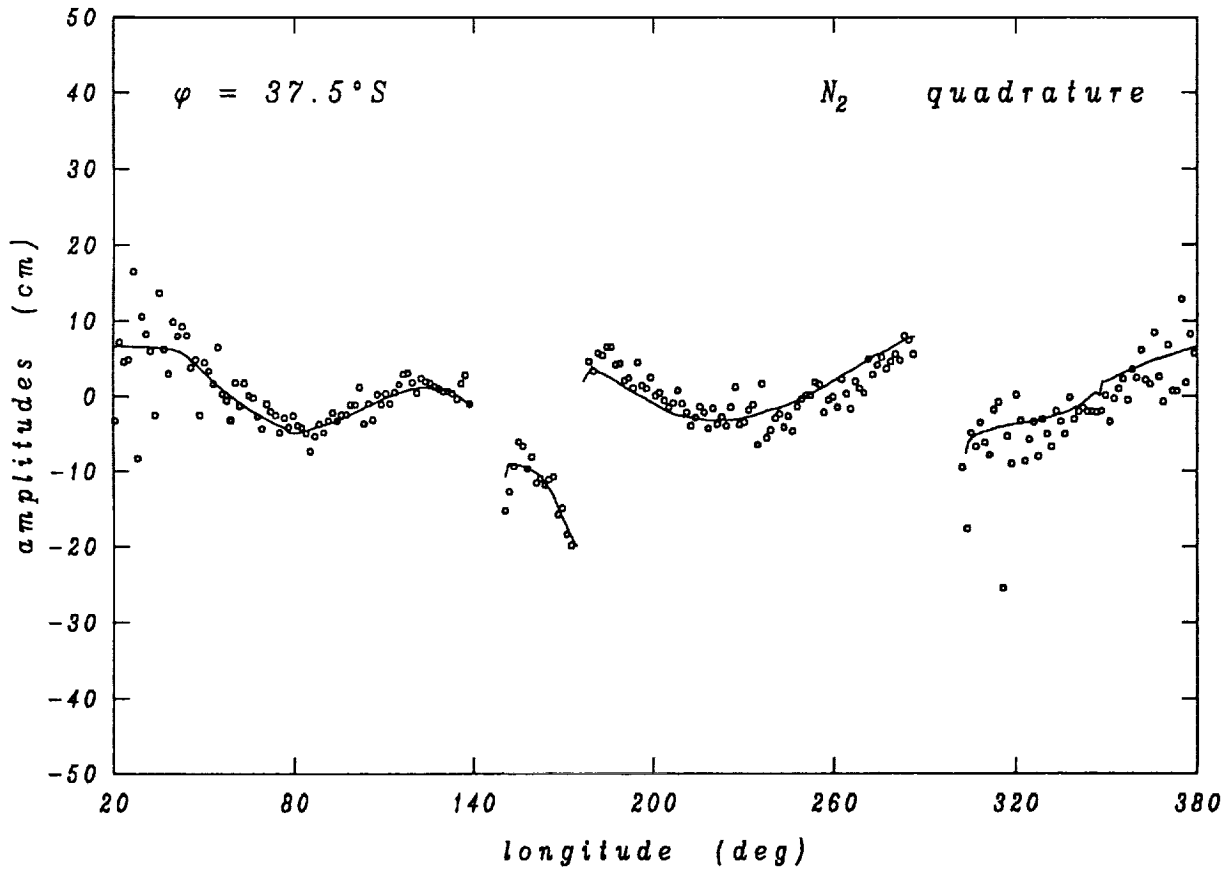
Figure 1: Raw tidal estimates of the quadrature component ($H \sin G$) of the N_2 tide, along a 1° global strip centered at latitude 37.5°S, based on only the first year of Geosat ERM data. Each circle represents a separate tidal determination in a particular 1° × 1.475° bin. The solid line represents the *Schwiderski* (1983) model. The large scatter near longitudes 15°–30° is presumably induced by the high mesoscale variability associated with the Agulhas Retroflection; similarly, scatter near longitude 310° reflects the presence of high variability at the confluence of the Brazil and Falkland Currents.

4
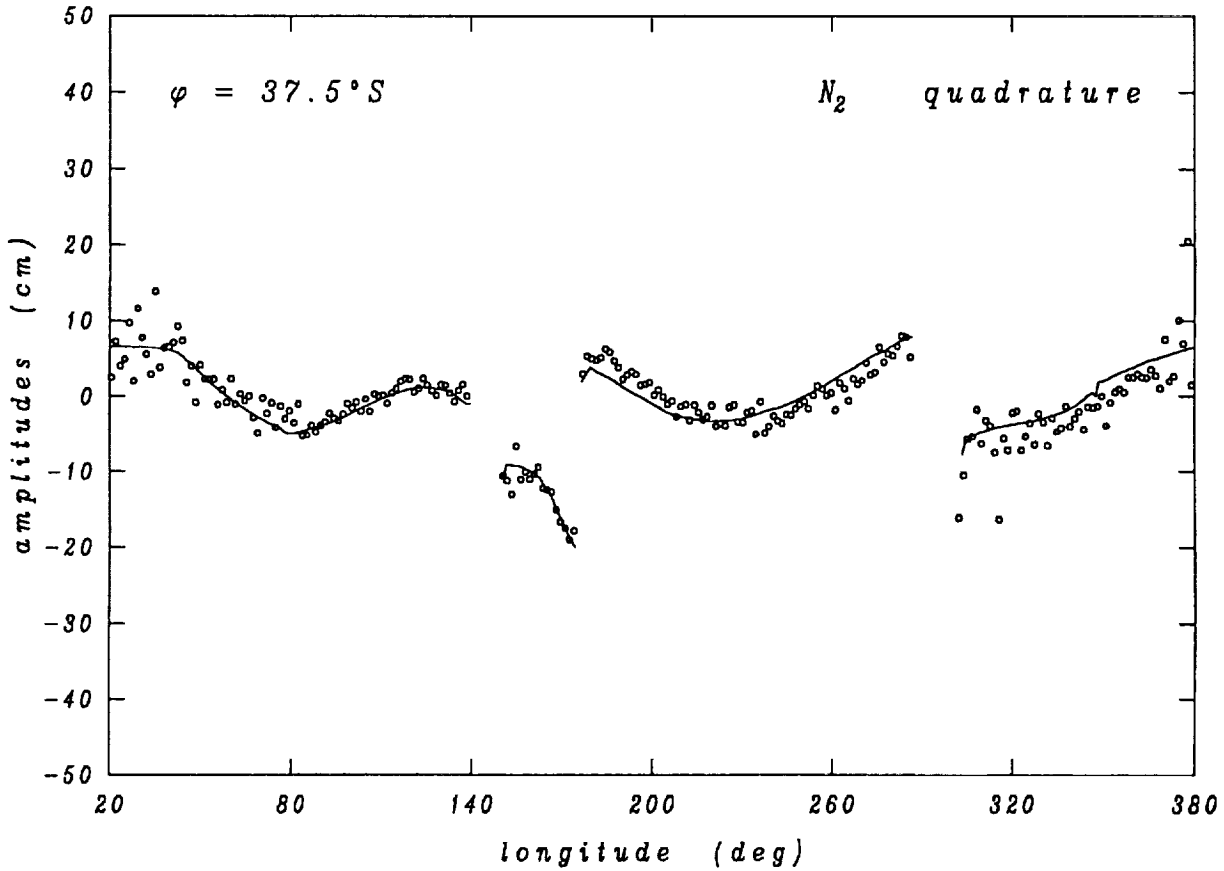
Figure 2: Similar to Figure 1, except based on two years of Geosat ERM data. The scatter is markedly reduced by the additional data, including the high scatter still somewhat present near the Agulhas and Patagonian high-mesoscale areas. These raw tidal estimates are spatially smoothed by methods discussed in CR90 before they are combined into grids to produce the maps shown below, e.g. Figure 5.2. A visual smoothing of the circled data shows that our N_2 component is several cm higher than *Schwiderski's* (1983) estimates along the Pacific east of New Zealand and several cm below west of Chile. It is also 3-5 cm below Schwiderski across nearly the breadth of the South Atlantic at this latitude.

(b) We consistently applied the "inverse barometer" correction, which had been omitted from some areas of CR90. This correction was based on the Fleet Numerical Oceanography Center (FNOC) atmospheric surface pressure data, which are provided on global grids every 12 hours. The corresponding Nyquist period of 1 day implies that atmospheric tides are not directly incorporated into the inverted barometer correction. The derived S_2 ocean tide showed marked improvement after this correction, but other constituents seemed little affected.

(c) The use of water-vapor corrections from the FNOC model, instead of from the climatological model derived from Nimbus-7 data, gave us more comprehensive data access in marginal seas (see Introduction, item b).

After our data processing was completed, new sources for pressure and water vapor fields have become available, and some are thought preferable to the FNOC fields (*Ray et al.*, 1991). But all atmospheric corrections are somewhat controversial; the robustness of tidal analysis relies as always on low correlation of residual errors with the tide potential.

4. In order to reduce loss of data due to ice cover at latitudes above 60°, the collecting bins there were widened in longitude by a factor of 2 or 3. During each satellite pass over a bin we characterized the several pulses by a median-filter instead of a straight mean value, to minimize the occasional effect of outliers. These procedures, together with the longer duration, greatly increased the number of usable passes for tidal analysis (above a practical minimum of 20 passes), resulting in fewer gaps and spatially smoother tide parameters.

3 Tidal Admittances

As in CR90 and CR91, and earlier work, we have found it convenient to organize the analysis and mapping of the tides in terms of complex *admittance* functions of frequency, defined as follows: Let a harmonic constituent of the tide potential of species $m = 1$ (daily) or 2 (half daily) at a surface point of latitude φ (N positive), east longitude λ be expressed as

$$V(\varphi, \lambda, t) = g\widetilde{H}_\sigma \alpha_2^m P_2^m(\varphi) \cos(A_\sigma + \sigma t + m\lambda), \tag{4}$$

where A_σ is the appropriate combination of classical mean (astronomical) longitudes at an arbitrary time origin, $P_2^m(\varphi)$ is the associated Legendre function, and $\widetilde{H}_\sigma$ is one of a set of known amplitudes in meters associated with a normalizing factor α_2^m. In the normalization used for the tables of $\widetilde{H}_\sigma$ by *Cartwright and Edden* (1973), we have

$$\alpha_2^m = -\sqrt{(5/24\pi)}, \quad \sqrt{(5/96\pi)},$$

$$P_2^m = 3\cos\varphi \sin\varphi, \quad 3\cos^2\varphi,$$

for $m = 1, 2$ respectively. A tidal variation at P of the same frequency, expressed as

$$h_\sigma(t) = \widetilde{H}_\sigma \left[X(\sigma) \cos(A_\sigma + \sigma t) - Y(\sigma) \sin(A_\sigma + \sigma t) \right] \tag{5}$$

is said to have an admittance $Z(\sigma) = X(\sigma) + iY(\sigma)$ to the tide potential at the (Greenwich) origin of longitude. Its harmonic amplitude is

$$H = |Z(\sigma)| \widetilde{H}_\sigma \tag{6}$$

and its Greenwich phase lag is

$$G = m\pi - \arg(Z(\sigma)), \tag{7}$$

where the $m\pi$ arises from the negative sign of α_2^1.

The above reference to Greenwich transits is as arbitrary as the Greenwich meridian itself. In some applications, such as in CR91 where we were mostly concerned with calculations of the work done by gravity on the tides, it is more convenient to refer phases to *local* transit at the meridian of P, longitude λ', say. In order to effect this we 'rotate' the admittance $Z(\sigma)$ to

$$Z'(\sigma) = Z(\sigma) \exp(-im\lambda'), \tag{8}$$

so that

$$X'(\sigma) = X \cos m\lambda' + Y \sin m\lambda'$$
$$Y'(\sigma) = Y \cos m\lambda' - X \sin m\lambda'.$$

Replacing Z by Z', the amplitude relationship (6) still holds while the Greenwich phase lag G is replaced by the *local* phase lag κ, as originally defined by Kelvin and Darwin—see, for example, *Schureman* (1940, §§ 144–146). Thus,

$$\kappa = G + m\lambda' = m\pi - \arg(Z'). \tag{9}$$

We shall call $Z'(\sigma)$ the *local* admittance in distinction to the *Greenwich* admittance $Z(\sigma)$. Its real part X' represents that part of the ocean tide at P which is in phase with the potential V at P; its imaginary part Y' represents the part in quadrature with V at P.

Finally, in this survey of basic principles we must distinguish between the ocean surface tide as deduced directly from altimetry (minus the solid 'body tide'), which we shall call the 'altimetric tide,' and the 'ocean tide' relative to the local sea bed as measured by *in situ* instruments. The altimetric tide consists of the sum of the ocean tide and the 'load tide' of the solid earth induced by the ocean loading. In oceanic locations the altimetric tide is about 89–94 percent of the ocean tide, depending on the wavelength scale considered, but exact relationship requires an explicit Green's function or high-degree spherical harmonic calculation. If the ocean tide is defined globally, the load tide and hence the altimetric tide may be computed for both ocean and land areas by multiplying the spherical harmonics of the ocean tide by a set of Love numbers (*e.g., Ray and Sanchez*, 1989). The reverse procedure is not so straightforward, because we do not know *à priori* the altimetric tide over land. An iterative procedure is then necessary to derive the ocean tide, as discussed in an appendix to CR91. (The iterative procedure converges so rapidly that, in fact, only one iteration is required.) We have applied this procedure to our altimetric tide solutions for all major harmonic constituents. The results, therefore, pertain correctly to the true ocean tide.

True ocean tide maps are required for calculations of energetics and comparison with hydrodynamic models. Altimetric tide maps are required for corrections to satellite altimetry prior to general oceanographic analysis.

Load tide maps are required for corrections to the positions of tracking stations and similar precise geodetic applications. Examples of all three types of map will be presented in the following pages, but maps of the true ocean tides will be most comprehensive. Digital files containing arrays of all tidal types are available on request.

An algorithm has been coded to compute the full diurnal plus semidiurnal altimetric tide (embodying all constituents through some 60 spectral lines) for any specified ocean position and time. It is also available on request.

4 Global Maps

On the global scale, Figures 3.1–3.4 show four pairs of maps for the M_2 constituent, describing:

3.1 contours of the *local* admittances X' and Y' of the altimetric tide;

3.2 contours of the *Greenwich* admittances X and Y of the altimetric tide;

3.3 contours of amplitude H and Greenwich phase lag G of the ocean tide;

3.4 contours of amplitude H_l and Greenwich phase lag G_l of the load tide.

Figures **4.1–4.4** show similar information for S_2; Figures **5.1–5.4** show N_2; Figures **6.1–6.4** show O_1; and Figures **7.1–7.4** show K_1. In addition, the color Plate 1 depicts the differences in the in-phase $H1 = H \cos G$ and quadrature $H2 = H \sin G$ components of our latest M_2 map (Figure 3.3) and the corresponding values from Schwiderski's numerical model. Color Plate 2 depicts similar information for O_1.

The local admittances X', Y' were also shown in CR91, and are repeated here for direct comparison with the Greenwich admittances X, Y, whose maps are similar to those of CR90 from the earlier analysis. Readers may find it interesting to compare the two types of representation, neither of which is common in the literature. In both types, nodes (amphidromes) occur at the intersection of zero contours of the real and imaginary parts, antinodes occur in areas of maximum modulus. The relation to (altimetric) amplitude and phase lag are

$$H = \widetilde{H} (X^2 + Y^2)^{1/2} = \widetilde{H} (X'^2 + Y'^2)^{1/2},$$

$$G = m\pi - \arg(X + iY), \qquad \kappa = m\pi - \arg(X' + iY'),$$

where $\widetilde{H}$ is the normalized potential amplitude from *Cartwright and Edden* (1973) (0.632 m for M_2, 0.294 for S_2, 0.121 for N_2, 0.262 for O_1, 0.369 for K_1), and $m = 1$ or 2 is the tidal species number. Note that the altimetric amplitudes are on average some 7 percent less than the true ocean tide for features of typical horizontal scales. As discussed in CR91, $-Y'P_2^m(\varphi)$ is directly proportional to the rates of working of tidal forces.

The maps of amplitude and phase (H, G) correspond to conventional ocean tide maps as produced by hydrodynamic models, such as those of

10

Schwiderski (1983) and *Parke and Hendershott* (1972). Differences from ground-truth at 80 selected stations, of order 2–4 cm, are discussed in CR91.

The load tide maps (H_l, G_l) may be compared with similar maps computed by *Parke and Hendershott* (1980) from their own model, and with load tides maps computed from Schwiderski's ocean tide models by *Ray and Sanchez* (1989) and by *Francis and Mazzega* (1990). The maps shown here were computed directly from the altimetric tides as described in the appendix to CR91. The methodology exploits "fast" numerical transforms to decompose the tide into a high degree and order series of spherical harmonics (in this case, to degree and order 122—see Section 6). The loading coefficients h'_n required for these computations were taken from *Farrell* (1972); *Ray and Sanchez* (1989) note that the load tides are rather insensitive to the choice of h'_n coefficients. The differences between the load tide maps given here and those in *Parke and Hendershott* (1980) and *Ray and Sanchez* (1989) stem primarily from differences in the underlying ocean tide models.

The color prints in Plate 1 are presented for comparison with similar representations in CR90 from our earlier (less accurate) model. Note that the CR90 model was strictly altimetric, without correction for the load tide, whereas the present maps properly compare the ocean tide version from CR91 with Schwiderski's ocean tide. The discrepancies for O_1 (Plate 2) have not been shown before in any form. Both M_2 and O_1 from the CR91 model have lower rms residuals than Schwiderski's models in comparison with the CR91 ground-truth stations. S_2 and K_1, on the other hand, had slightly greater rms residuals than Schwiderski, so no color plates are shown for these solar constituents.
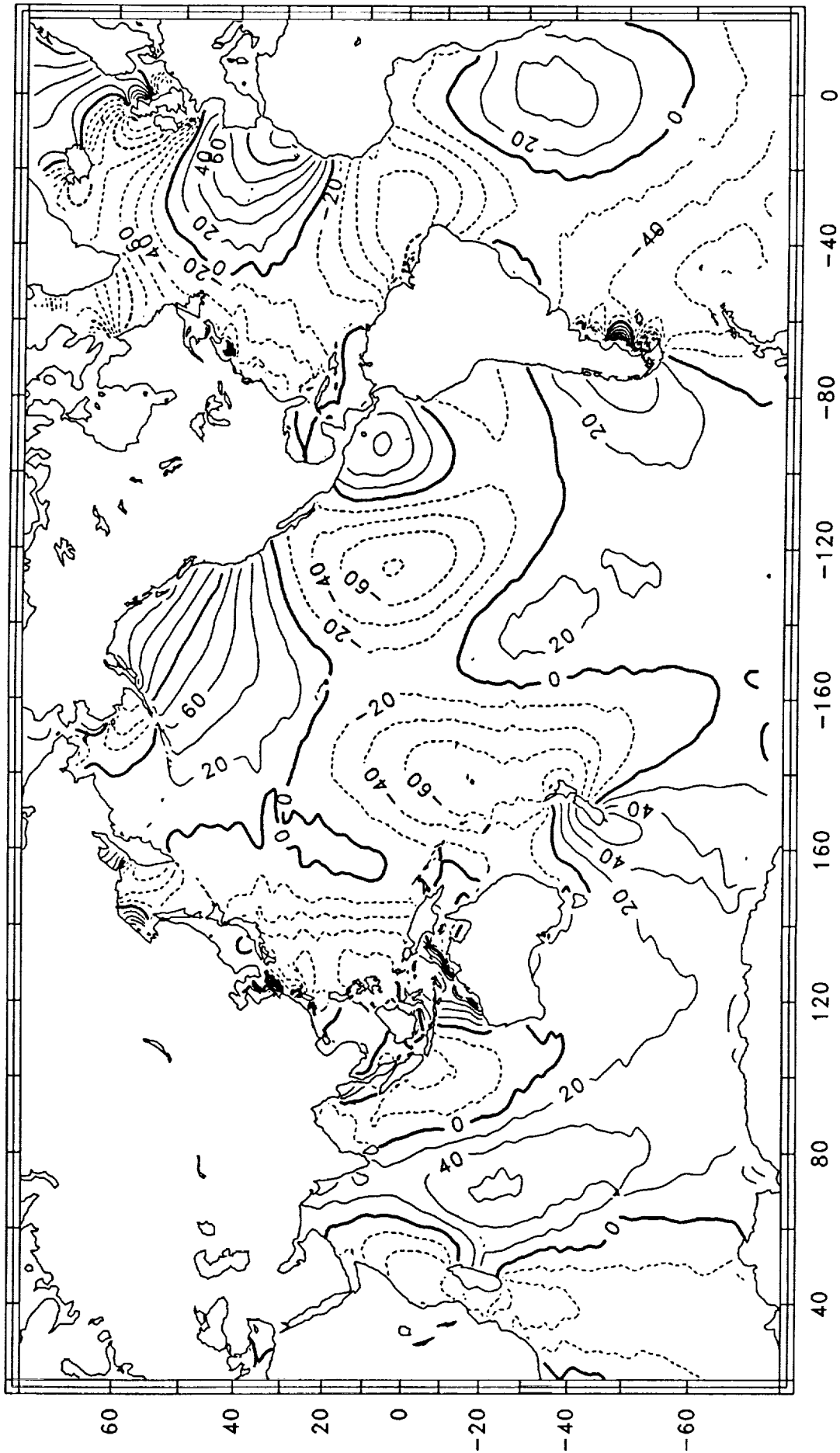
Figure 3.1a: Real component X' of the local admittance of the M_2 altimetric tide, in percent. Dashed contours are negative.
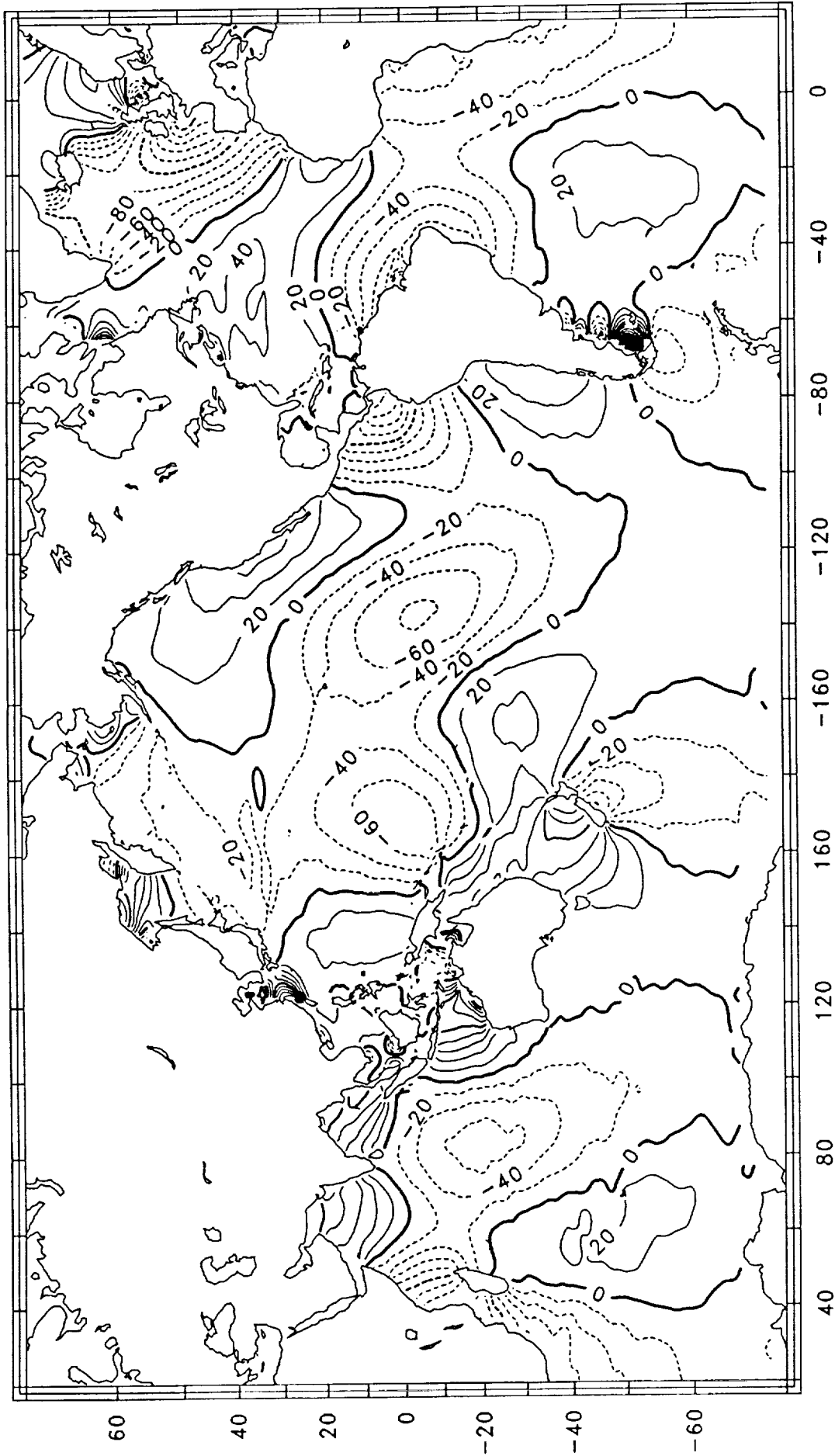
Figure 3.1b: Imaginary component Y' of the local admittance of the M_2 altimetric tide, in percent. Dashed contours are negative.
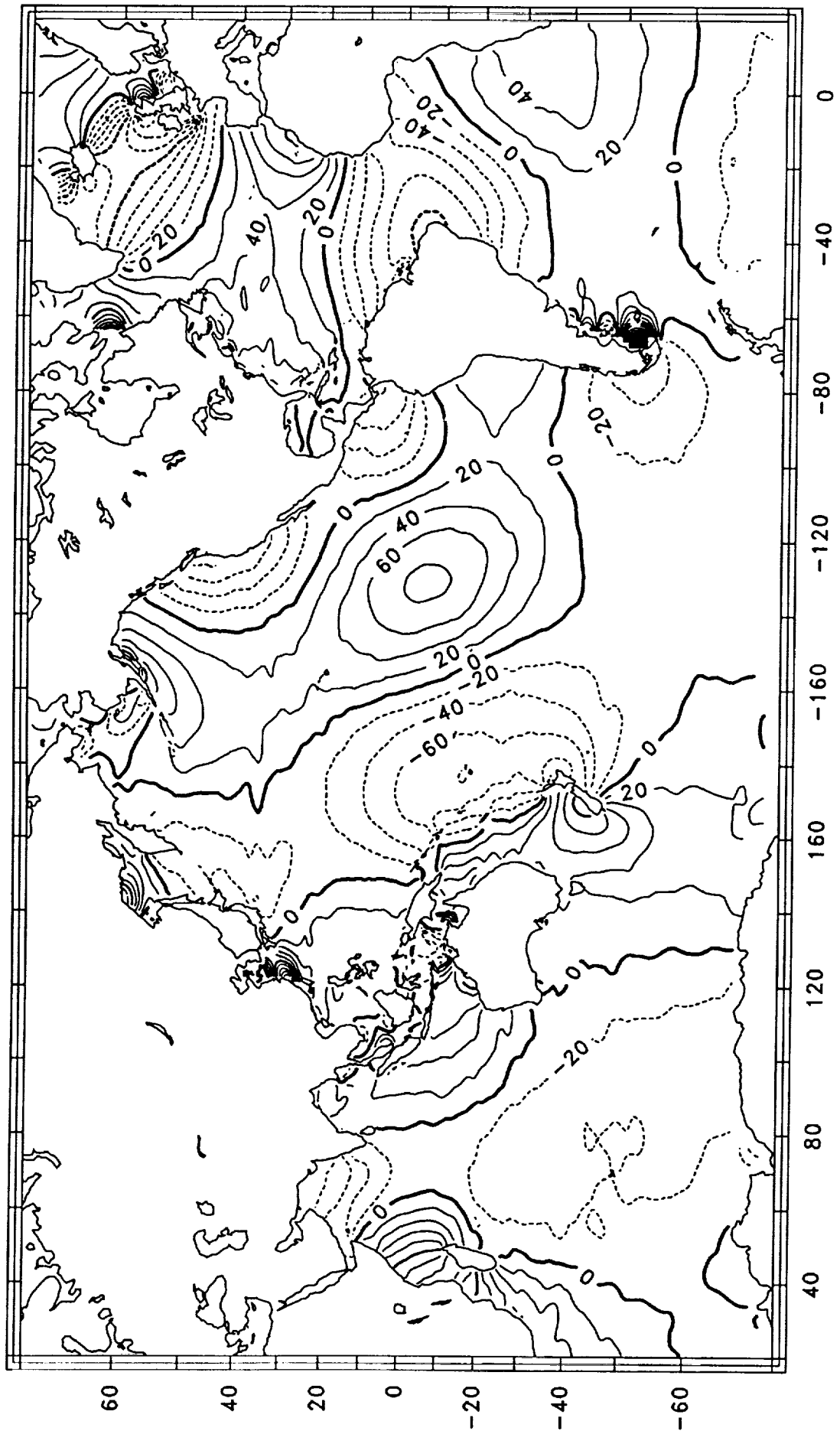
Figure 3.2a: Real component X of the Greenwich admittance of the M_2 altimetric tide, in percent. Dashed contours are negative.

14
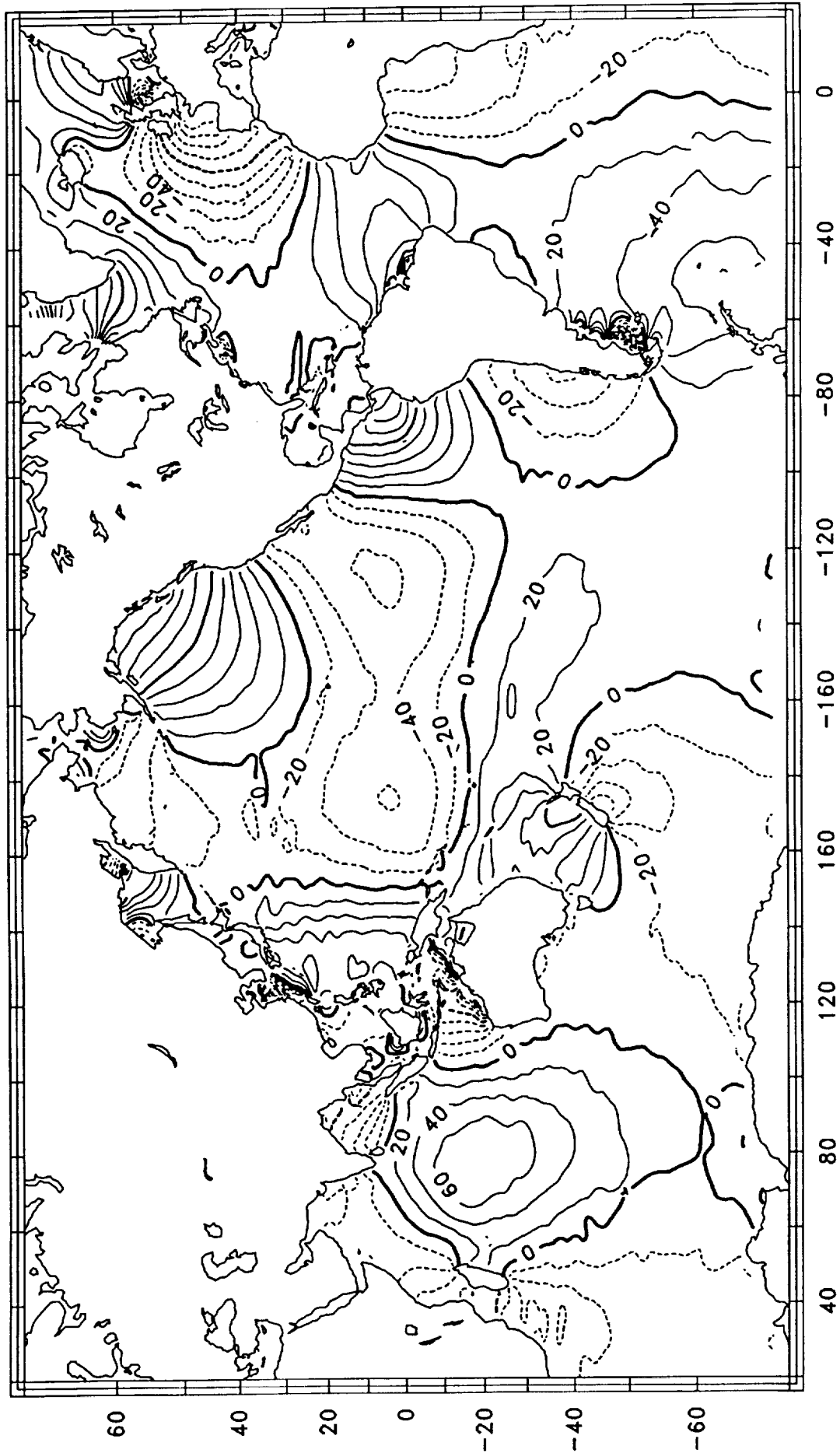
Figure 3.2b: Imaginary component Y of the Greenwich admittance of the M_2 altimetric tide, in percent. Dashed contours are negative.
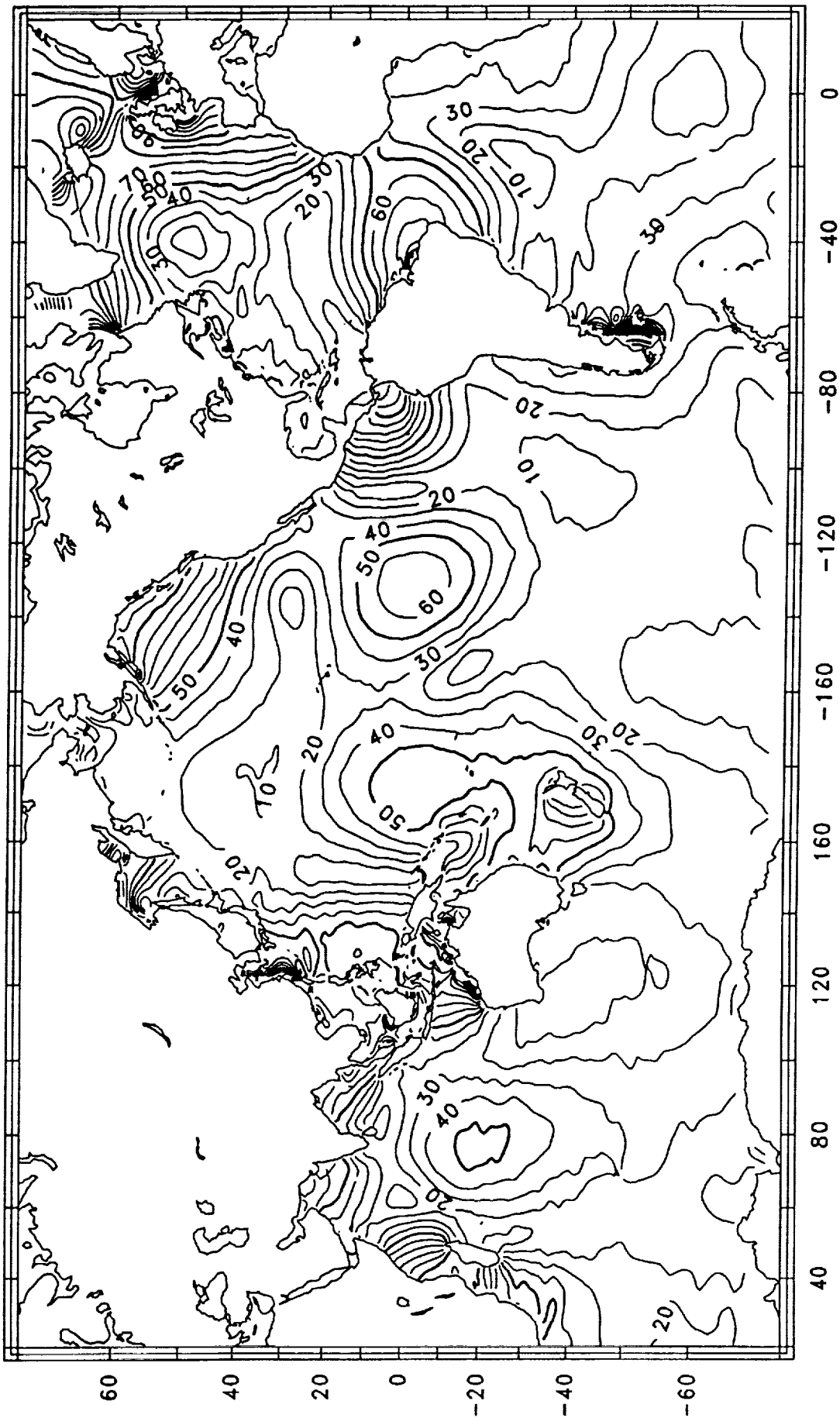
Figure 3.3a: Amplitude H of the M_2 ocean tide. Contour interval 10 cm.
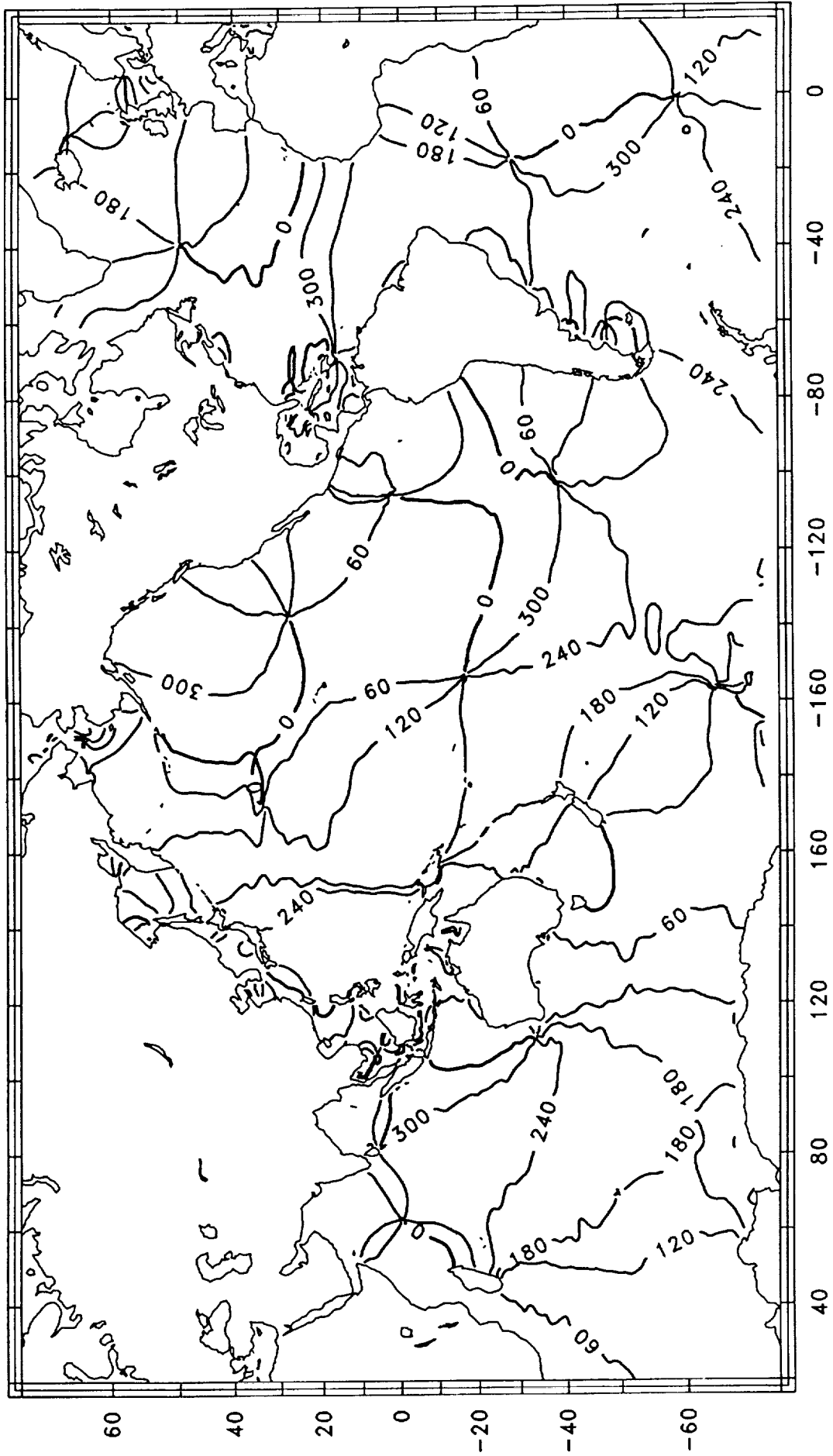
Figure 3.3b: Greenwich phase G of the M_2 ocean tide. Contour interval $60°$.
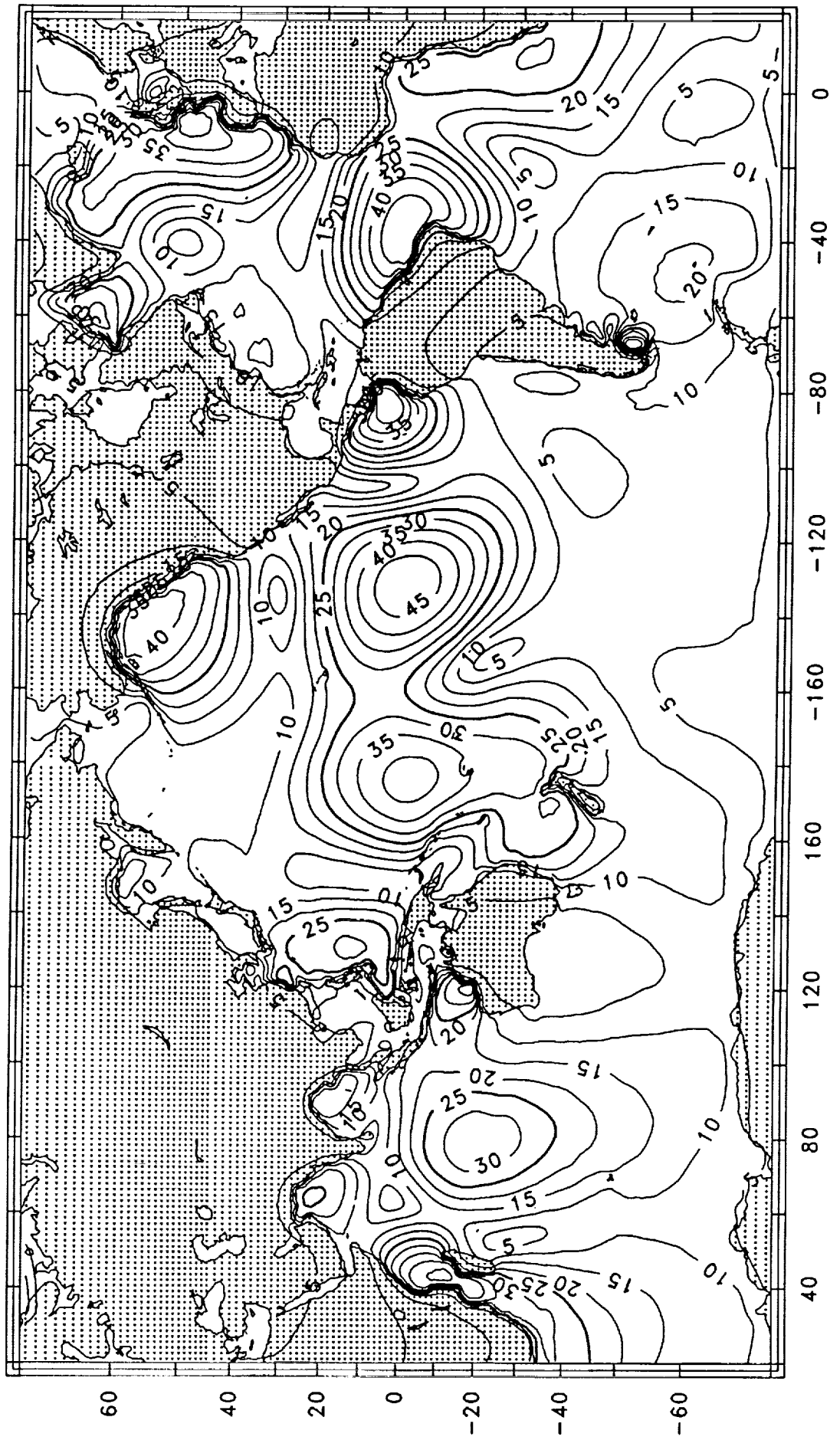
Figure 3.4a: Amplitude H_l of the M_2 load tide. Contour interval 5 mm.

18
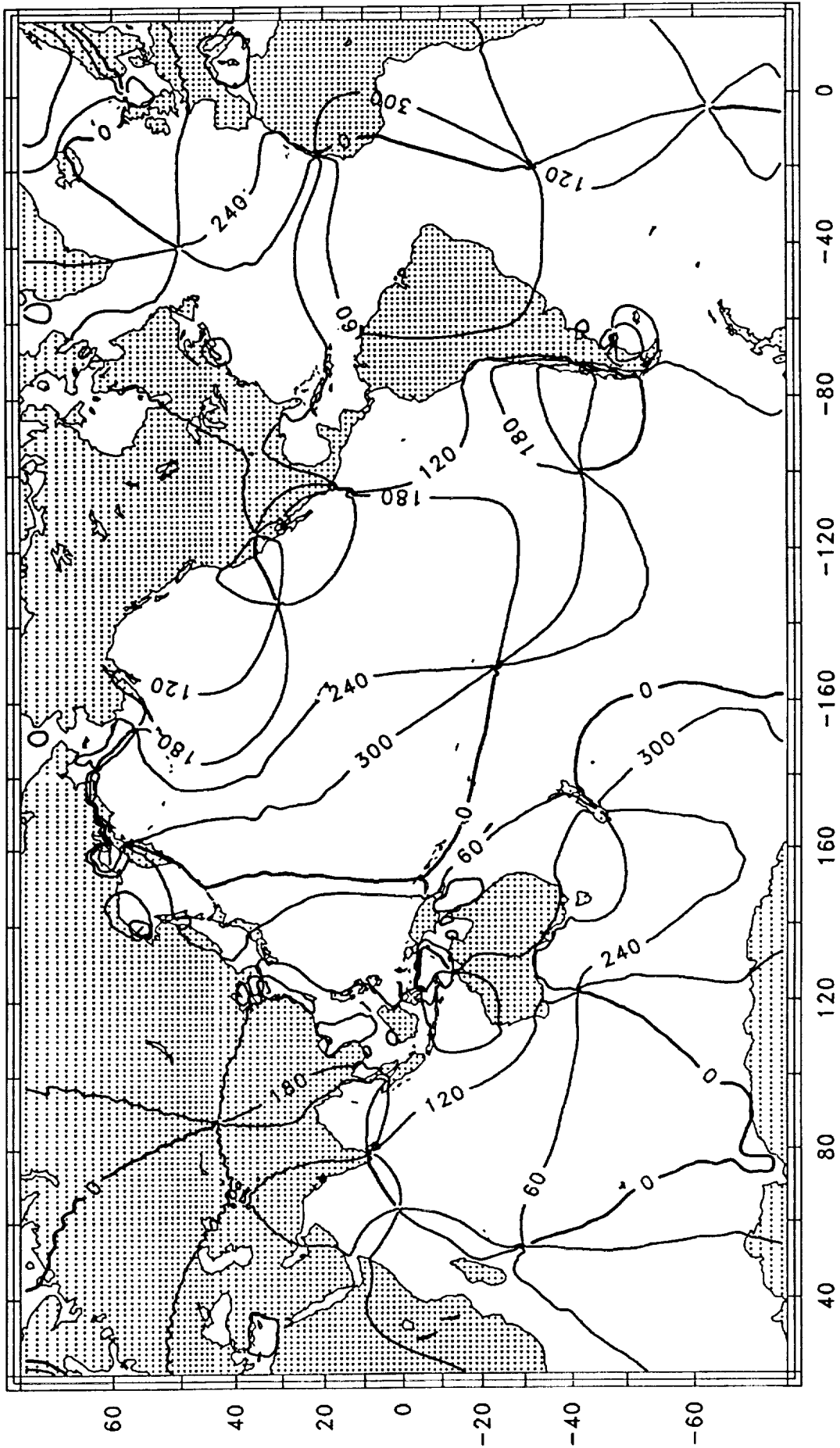
Figure 3.4b: Greenwich phase G_l of the M_2 load tide. Contour interval 60°.
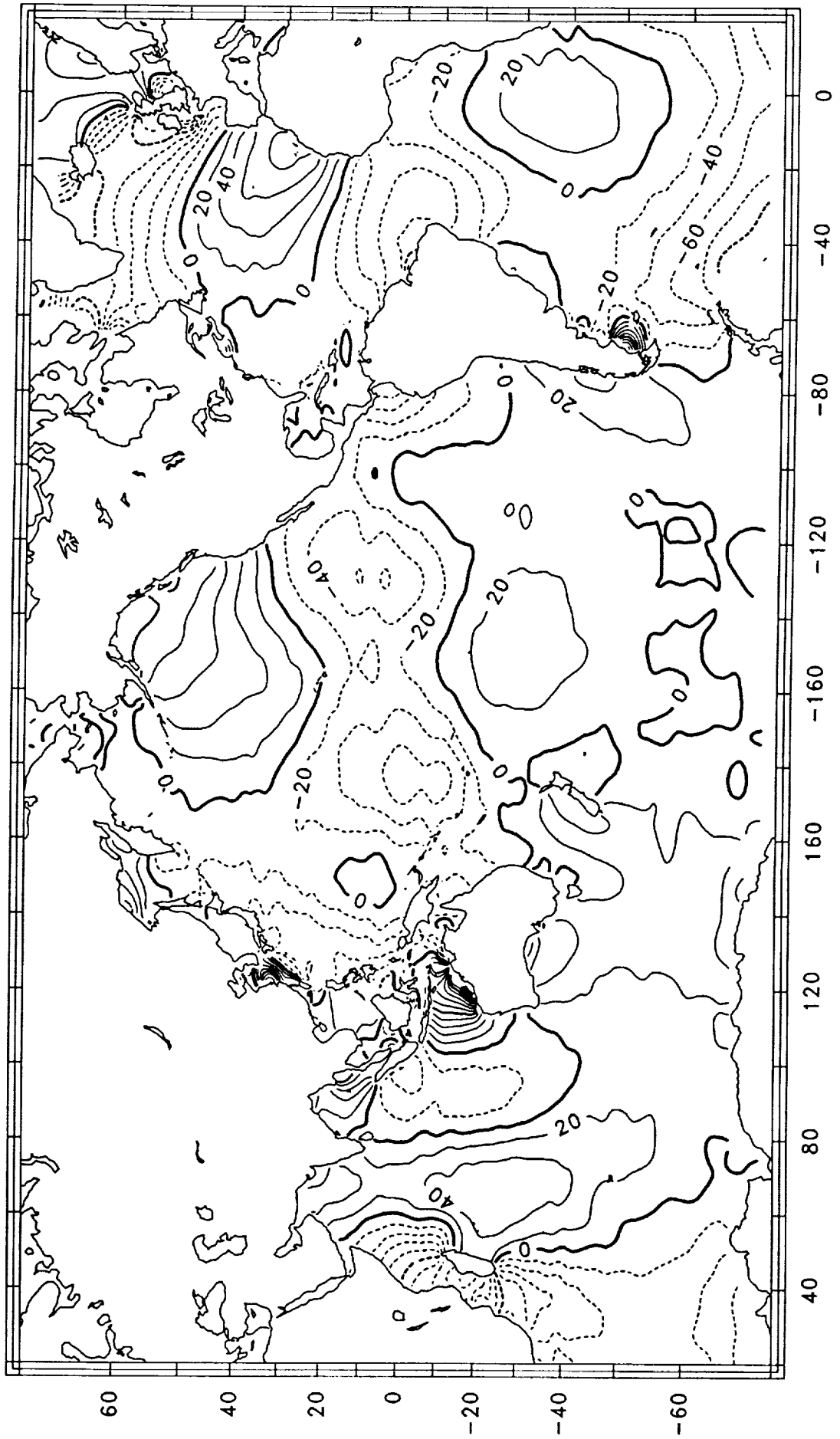
Figure 4.1a: Real component X' of the local admittance of the S_2 altimetric tide, in percent. Dashed contours are negative.

20
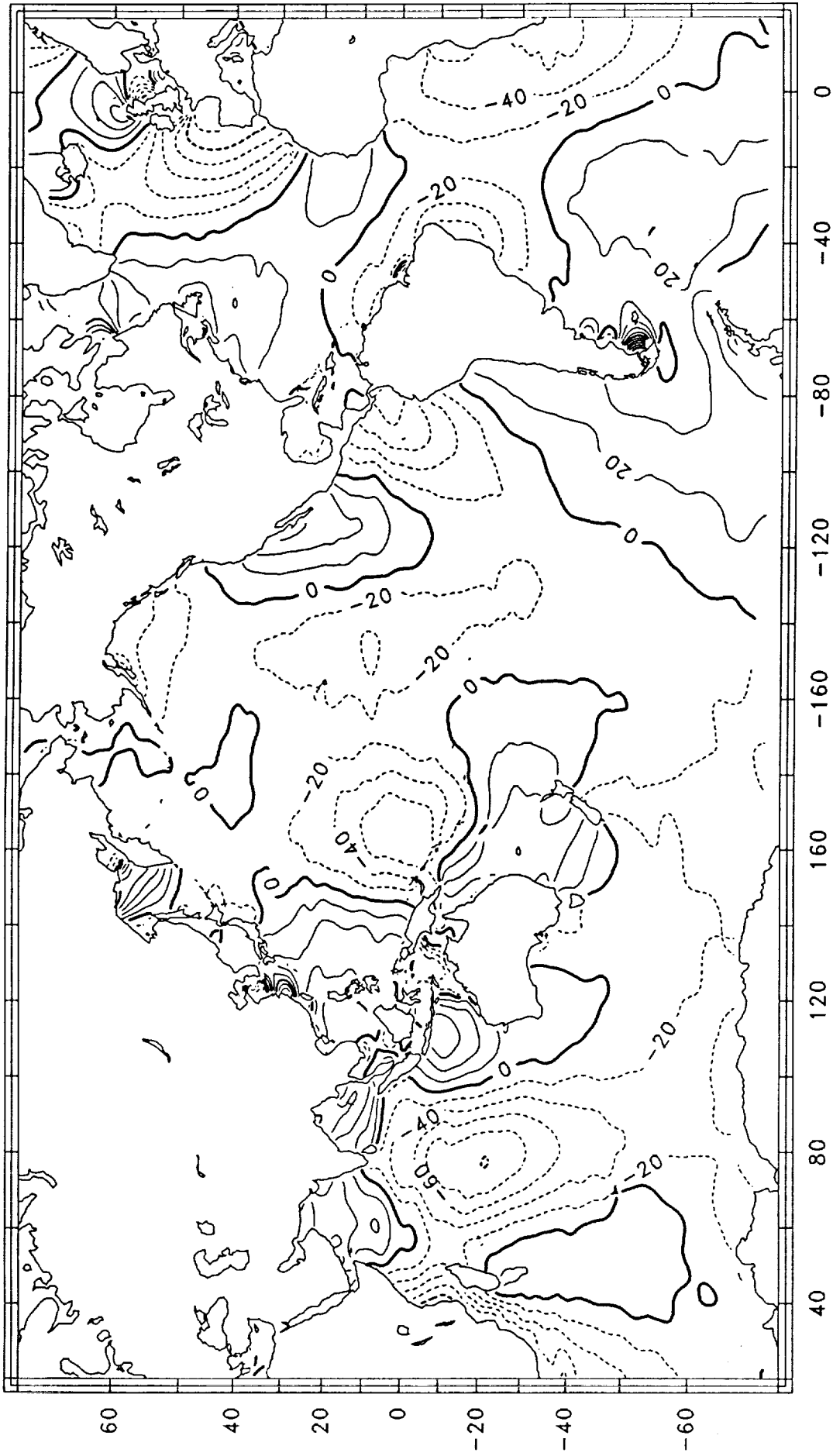
Figure 4.1b: Imaginary component Y' of the local admittance of the S_2 altimetric tide, in percent. Dashed contours are negative.

21
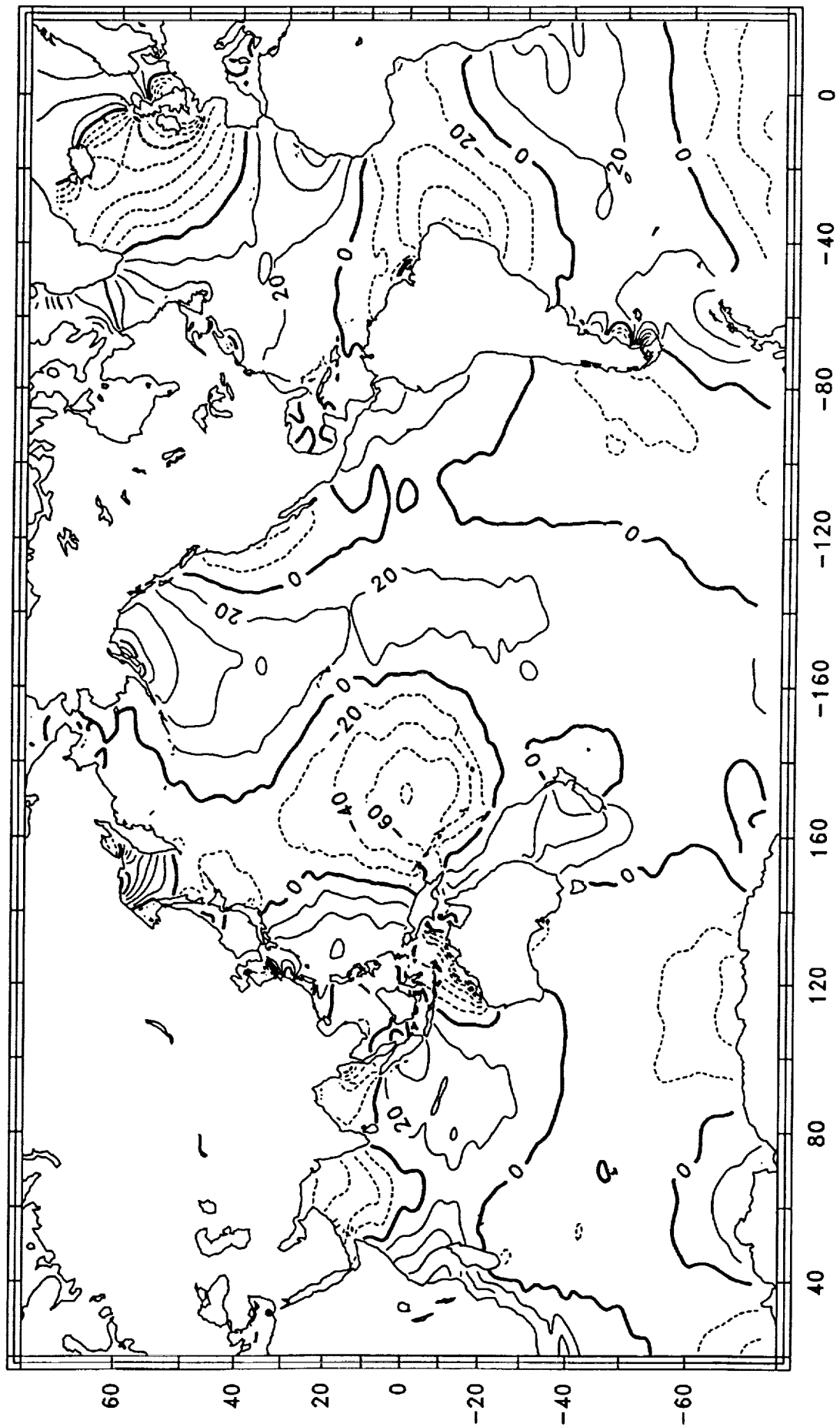
Figure 4.2a: Real component X of the Greenwich admittance of the S_2 altimetric tide, in percent. Dashed contours are negative.

22
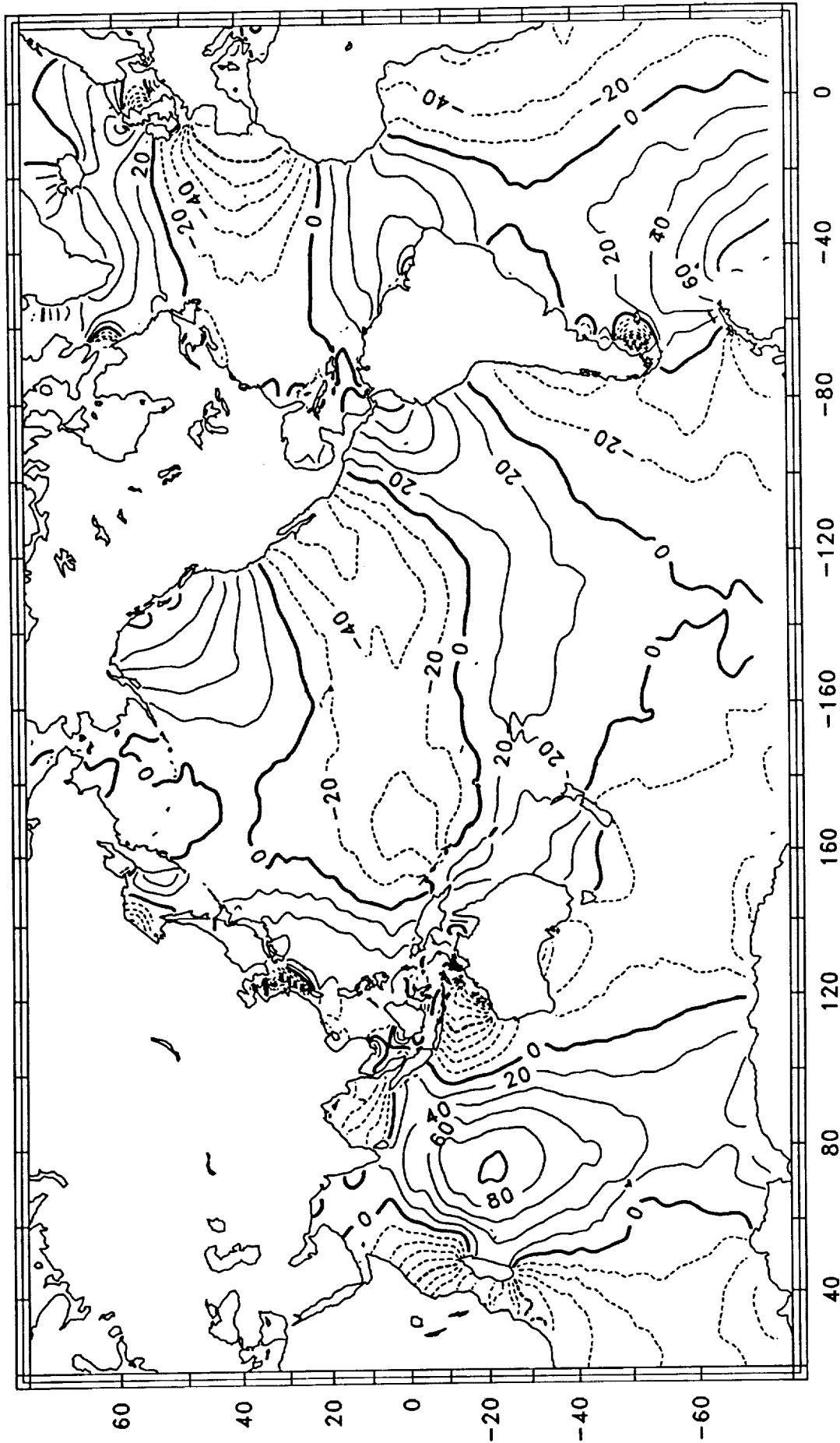
Figure 4.2b: Imaginary component Y of the Greenwich admittance of the S_2 altimetric tide, in percent. Dashed contours are negative.
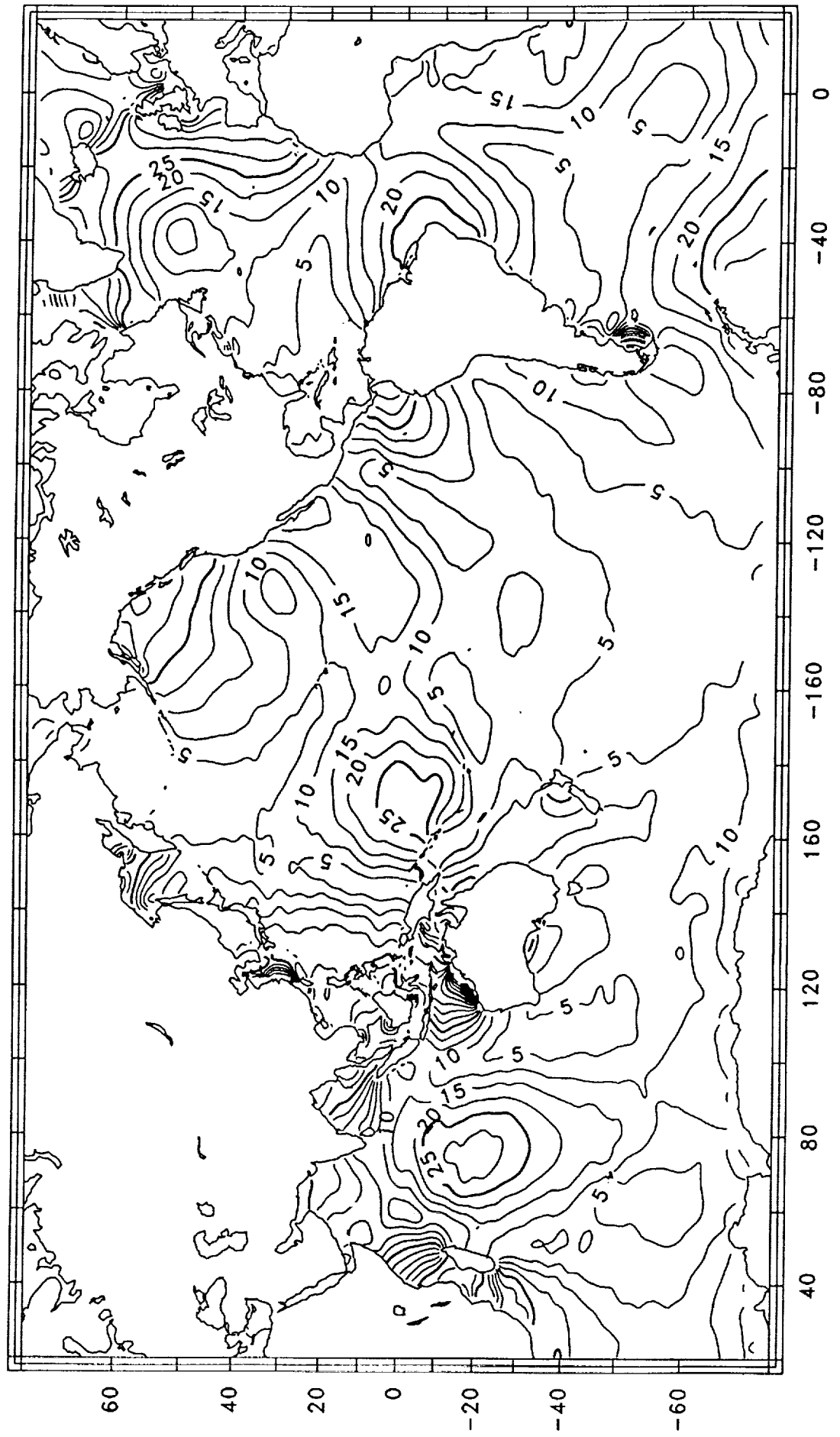
Figure 4.3a: Amplitude H of the S_2 ocean tide. Contour interval 5 cm.

24
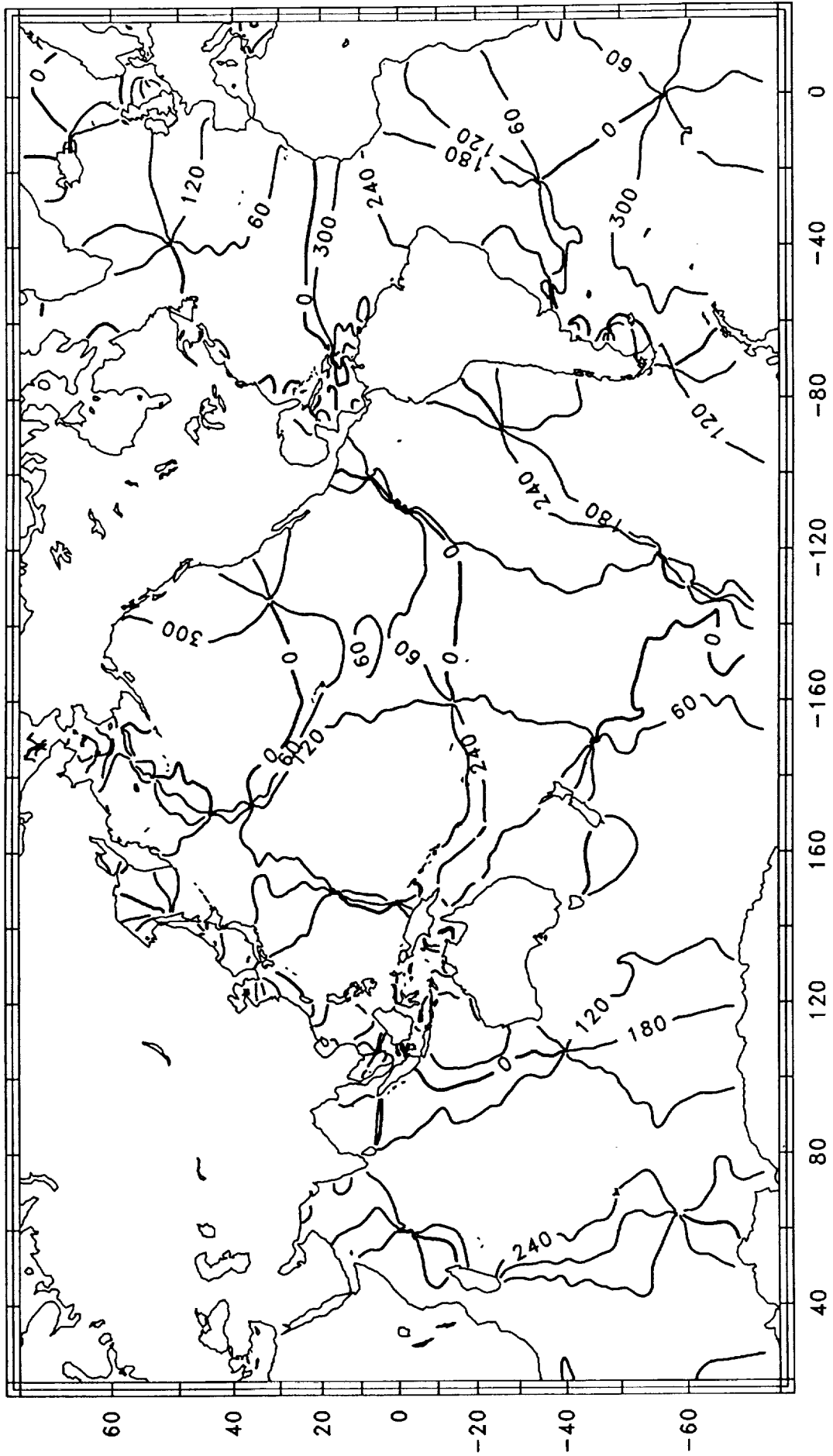
Figure 4.3b: Greenwich phase G of the S_2 ocean tide. Contour interval 60°.
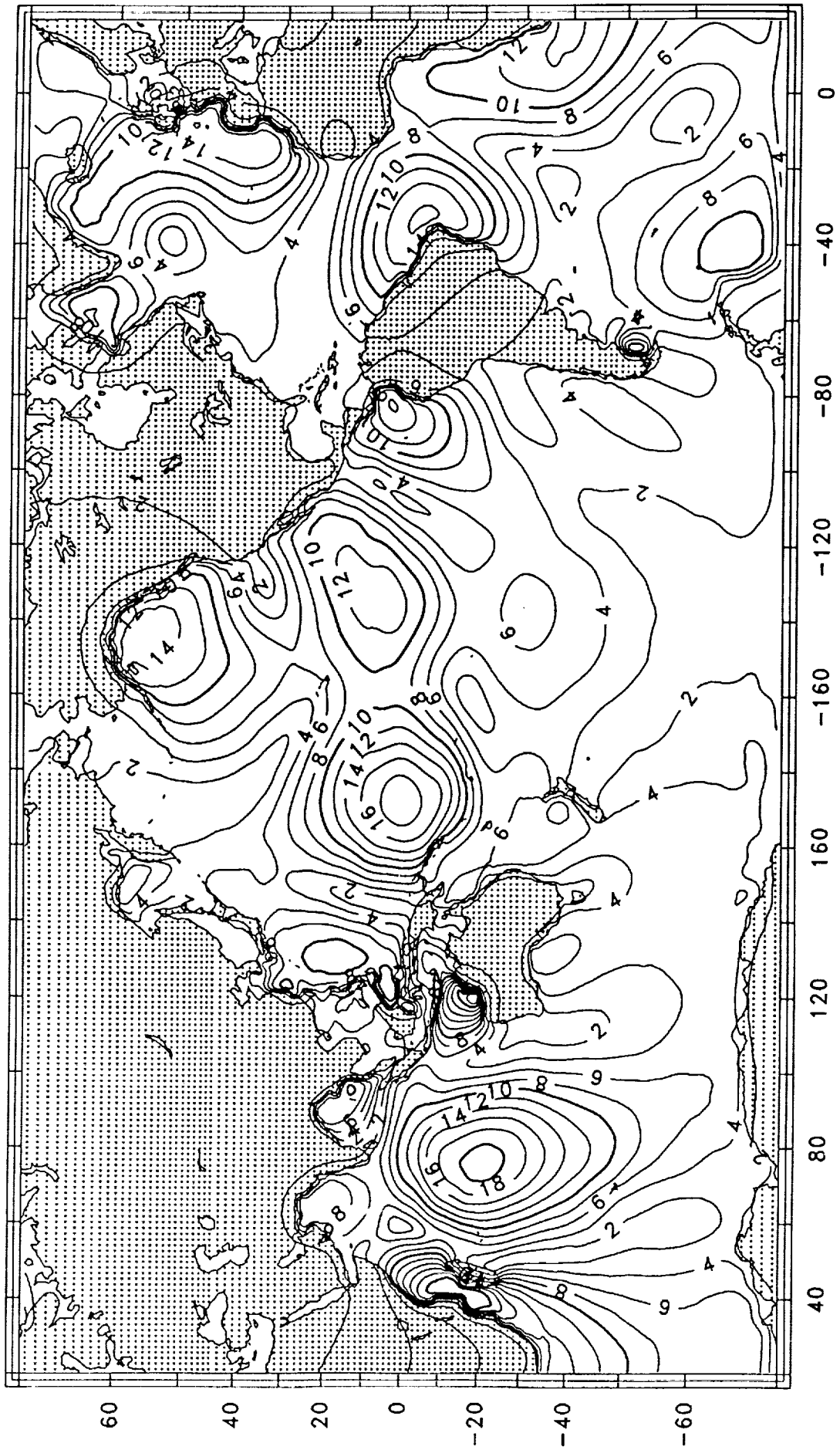
Figure 4.4a: Amplitude H_l of the S_2 load tide. Contour interval 2 mm.
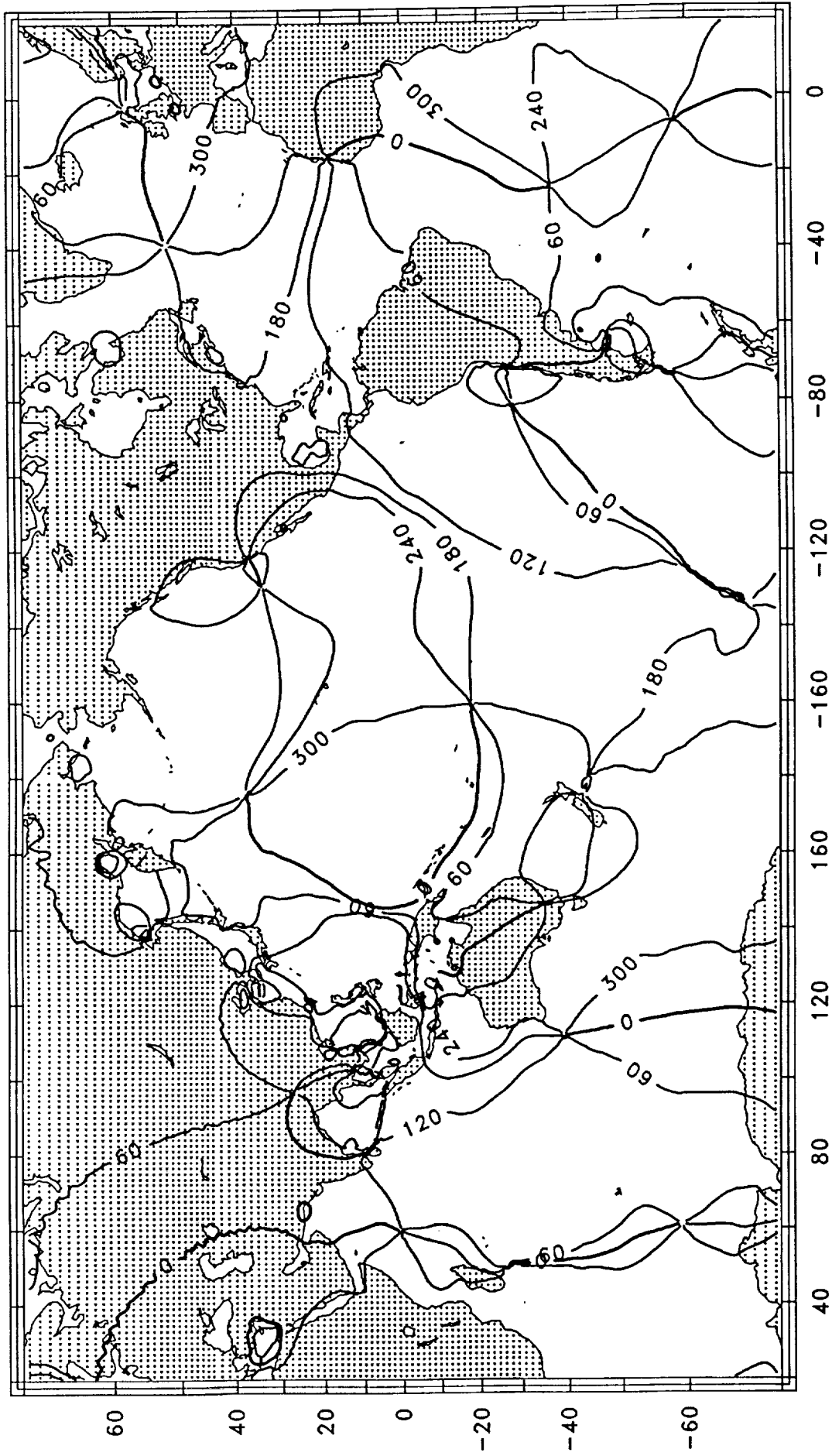
Figure 4.4b: Greenwich phase G_l of the S_2 load tide. Contour interval 60°.
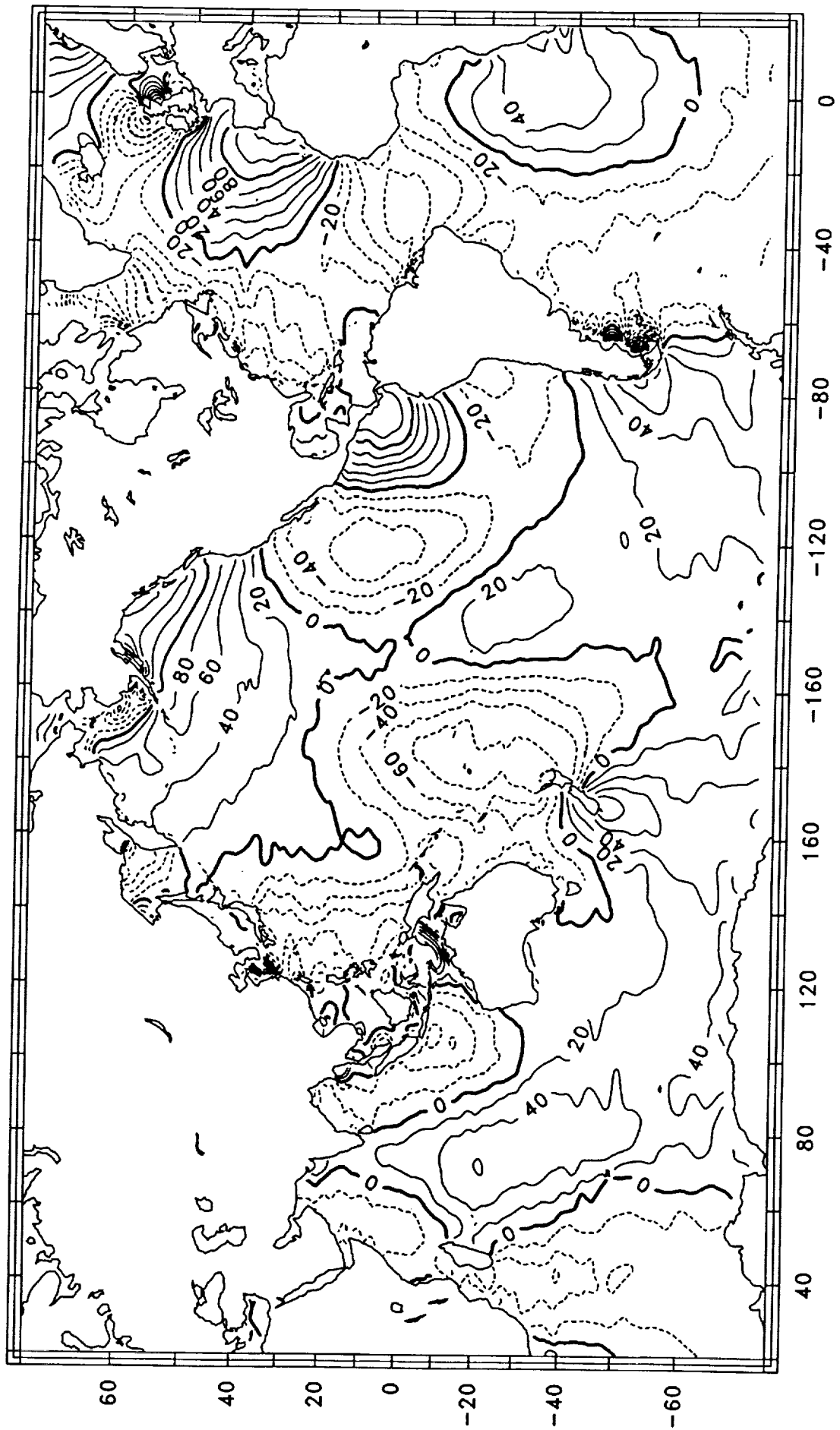
Figure 5.1a: Real component X' of the local admittance of the N_2 altimetric tide, in percent. Dashed contours are negative.

28
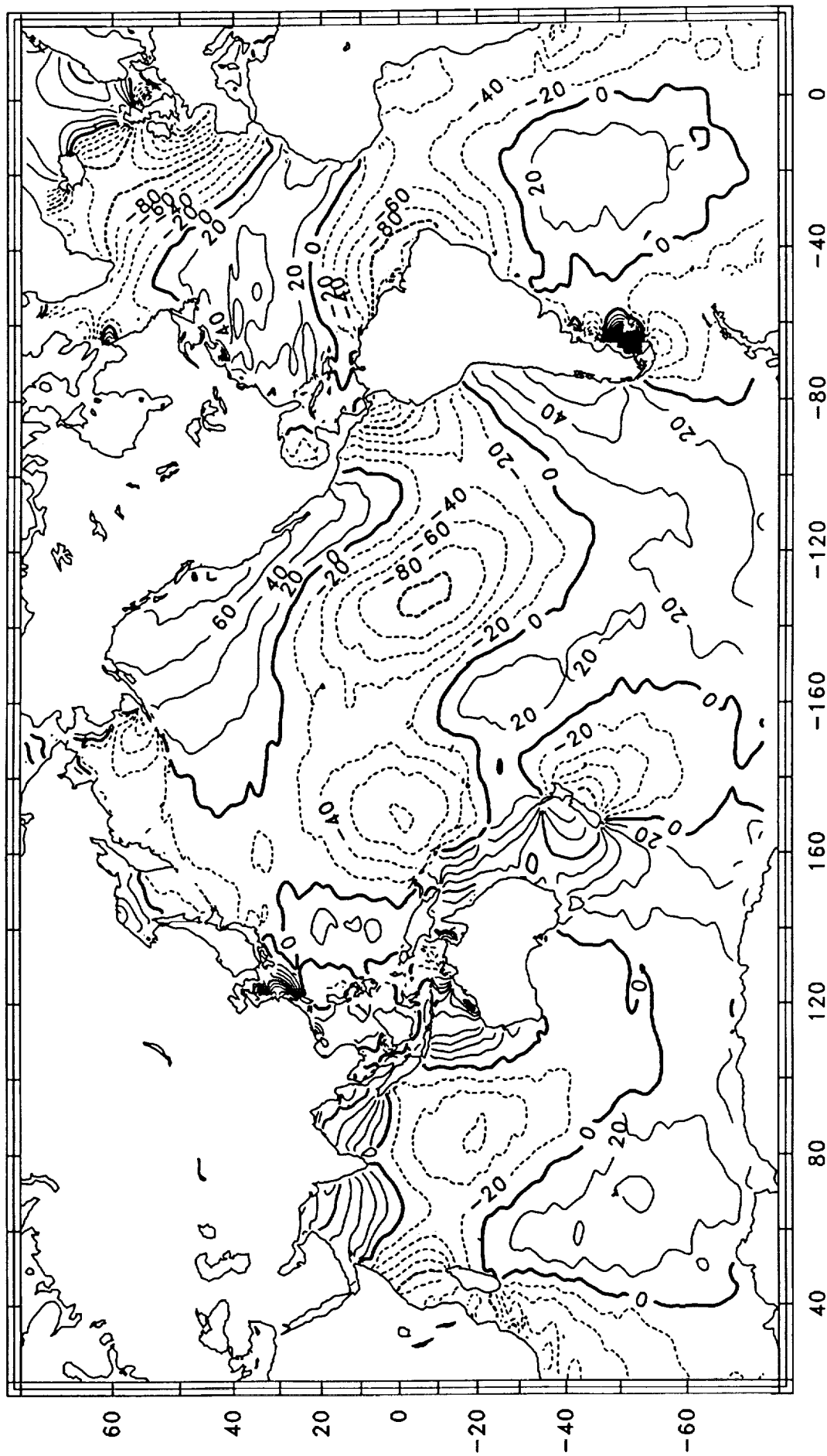
Figure 5.1b: Imaginary component Y' of the local admittance of the N_2 altimetric tide, in percent. Dashed contours are negative.

29
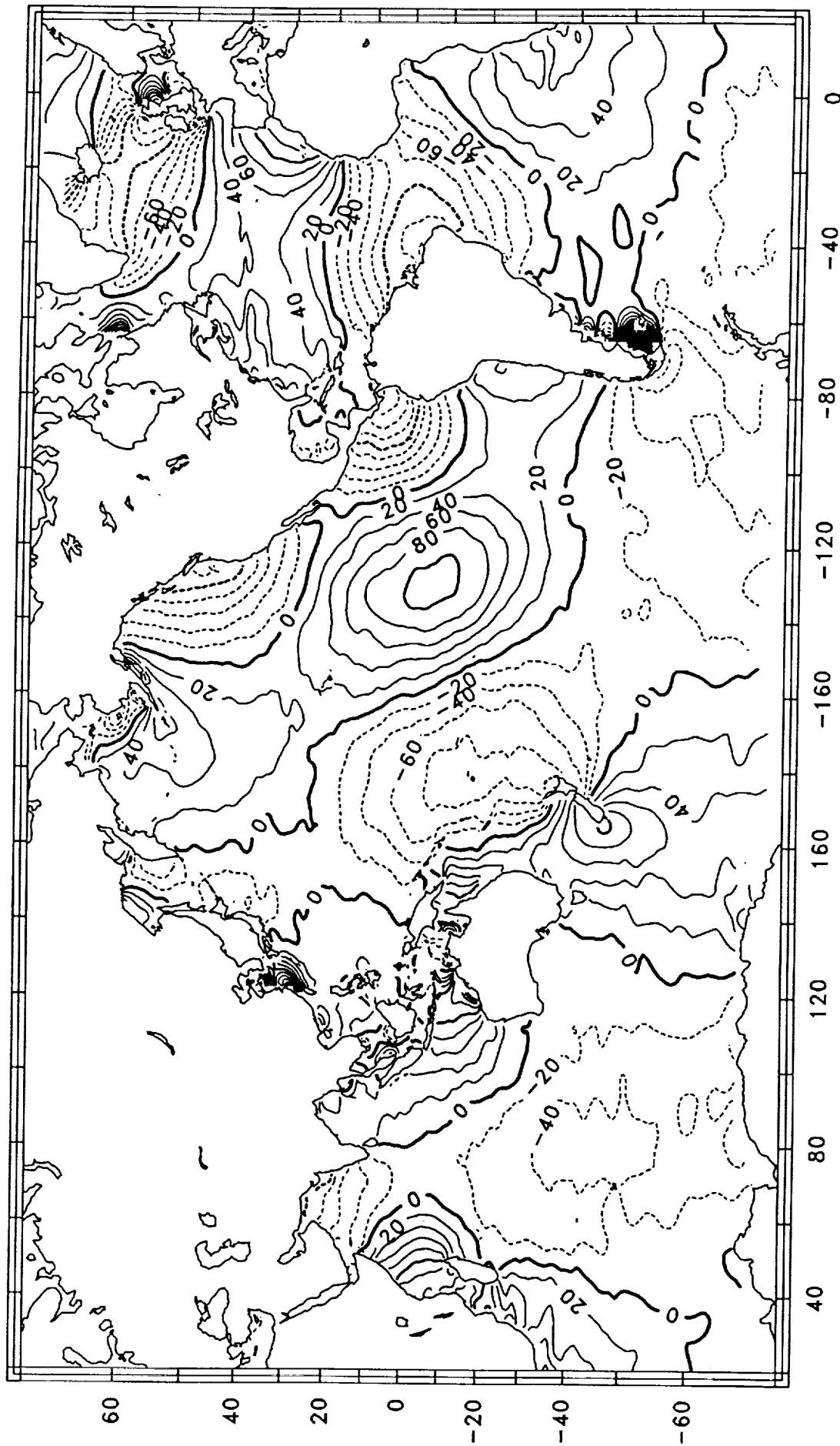
Figure 5.2a: Real component X of the Greenwich admittance of the N_2 altimetric tide, in percent. Dashed contours are negative.
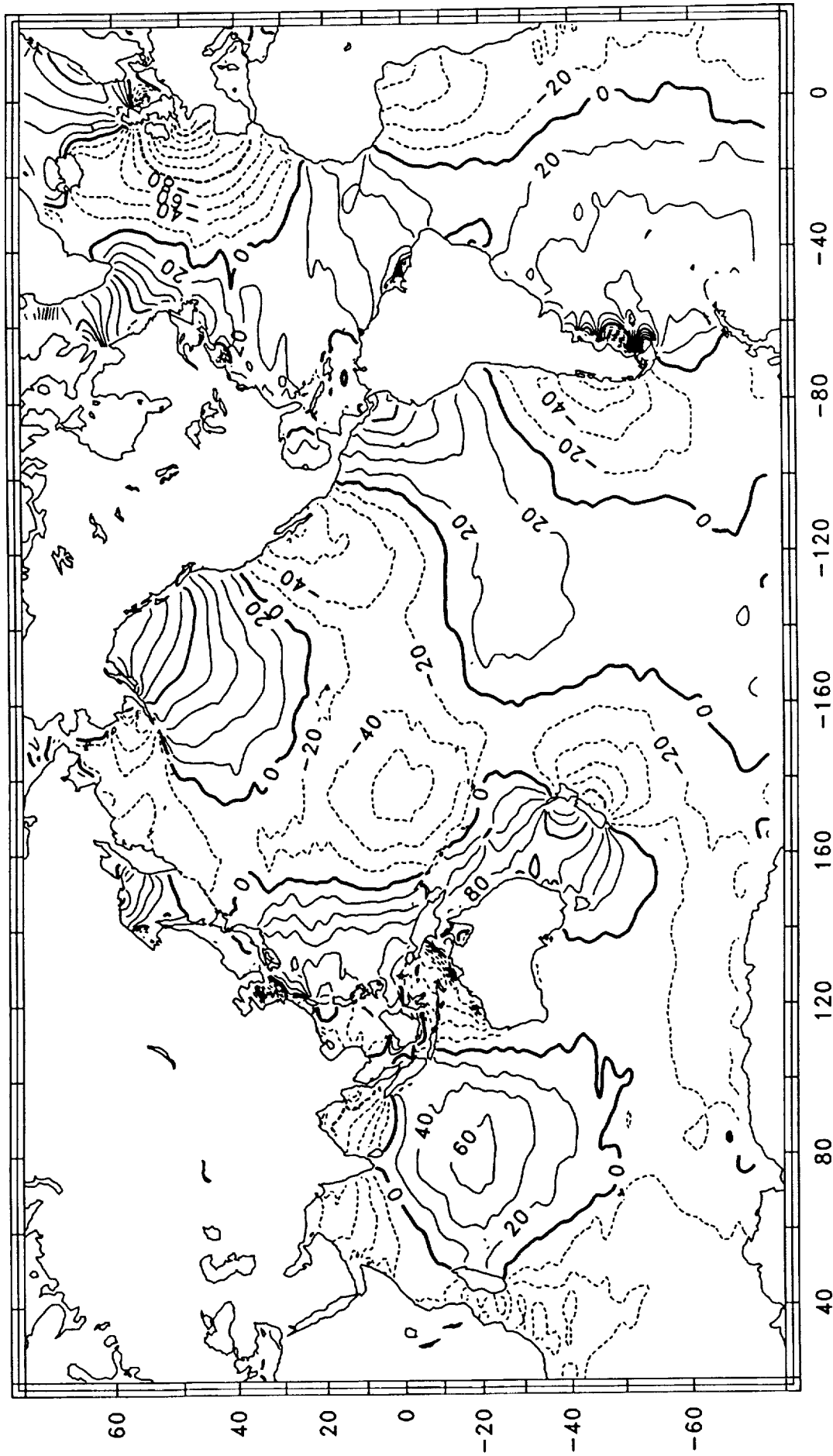
Figure 5.2b: Imaginary component Y of the Greenwich admittance of the N_2 altimetric tide, in percent. Dashed contours are negative.
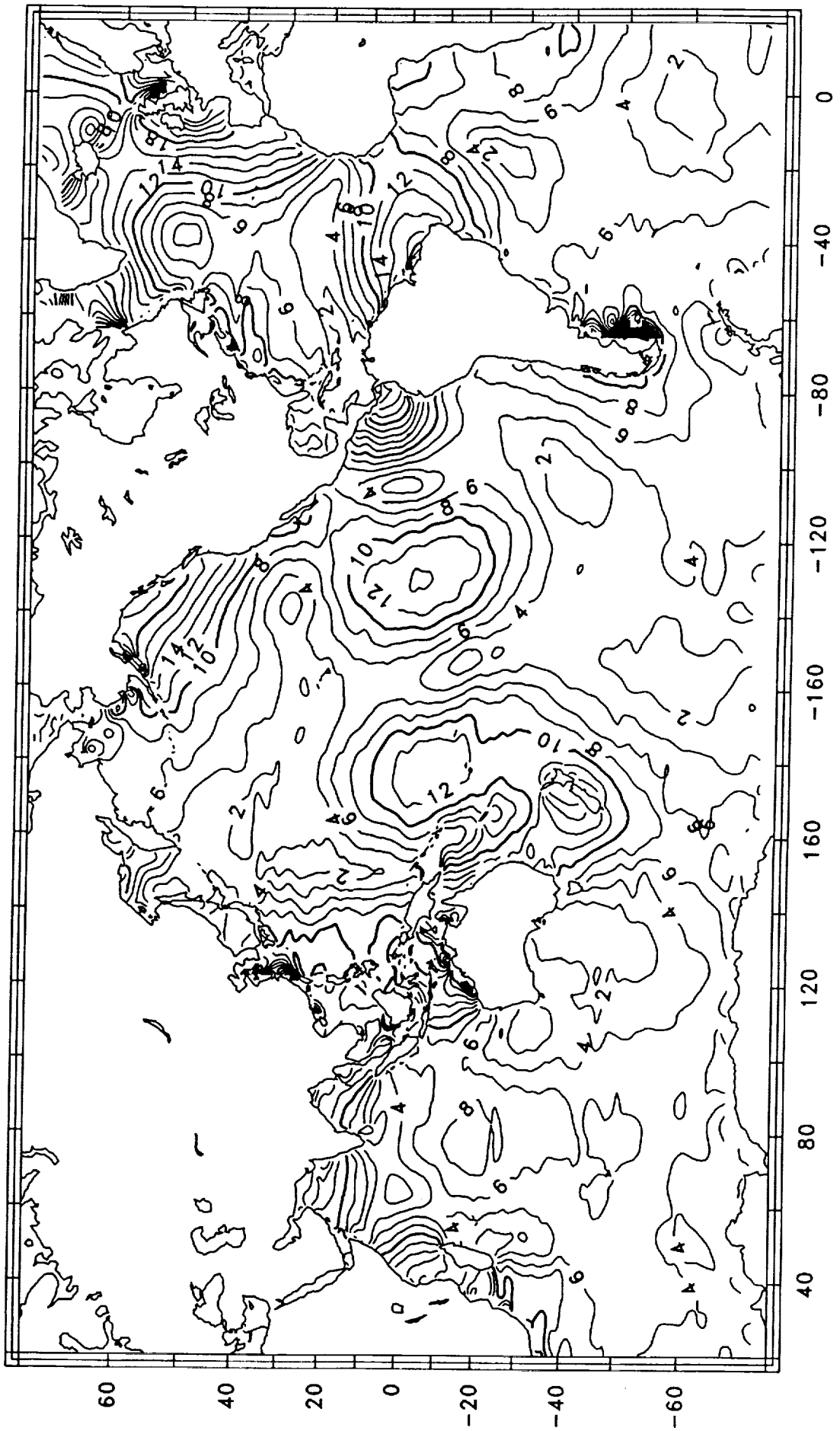
Figure 5.3a: Amplitude H of the N_2 ocean tide. Contour interval 2 cm.

32
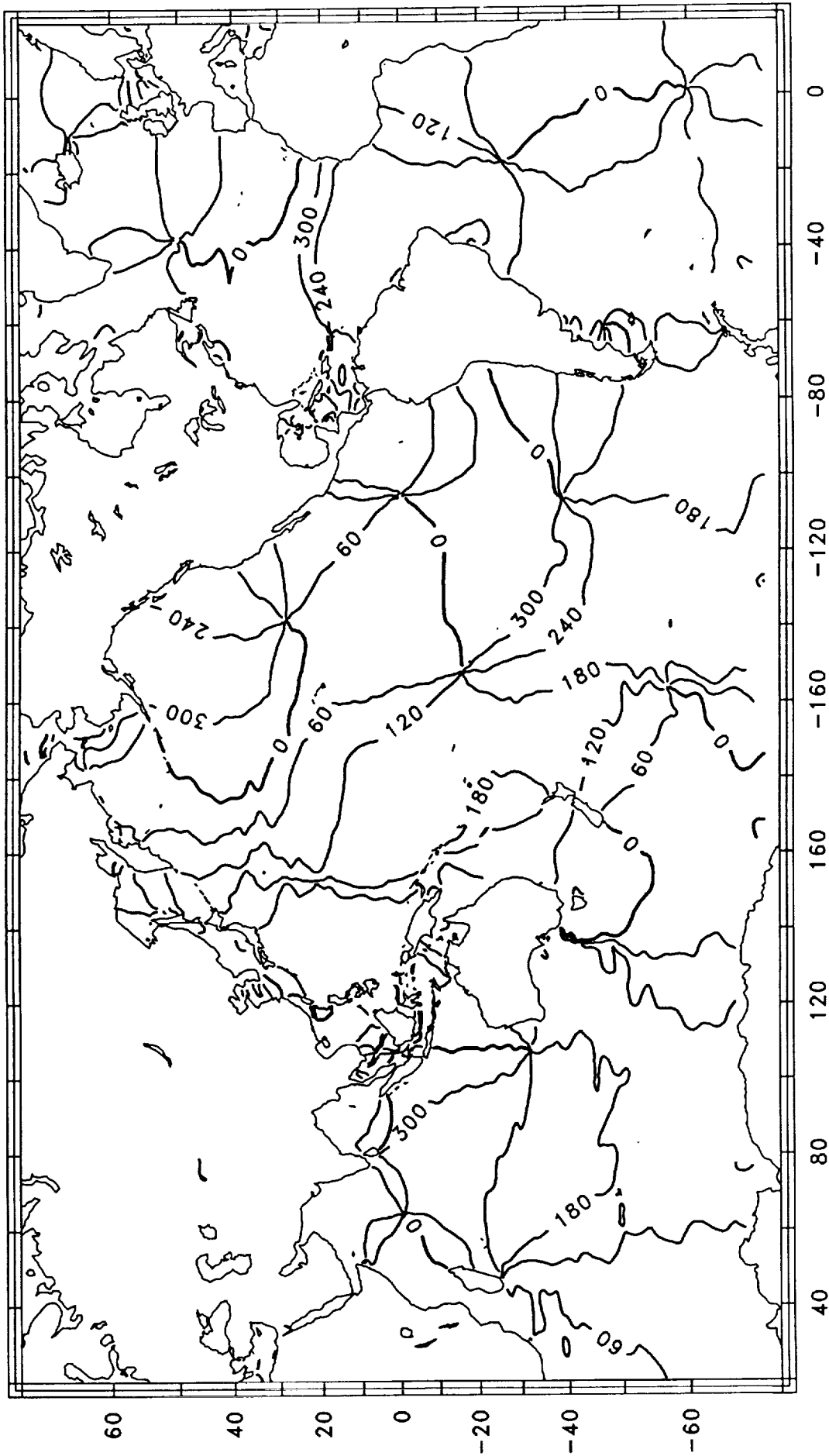
Figure 5.3b: Greenwich phase G of the N_2 ocean tide. Contour interval 60°.

33
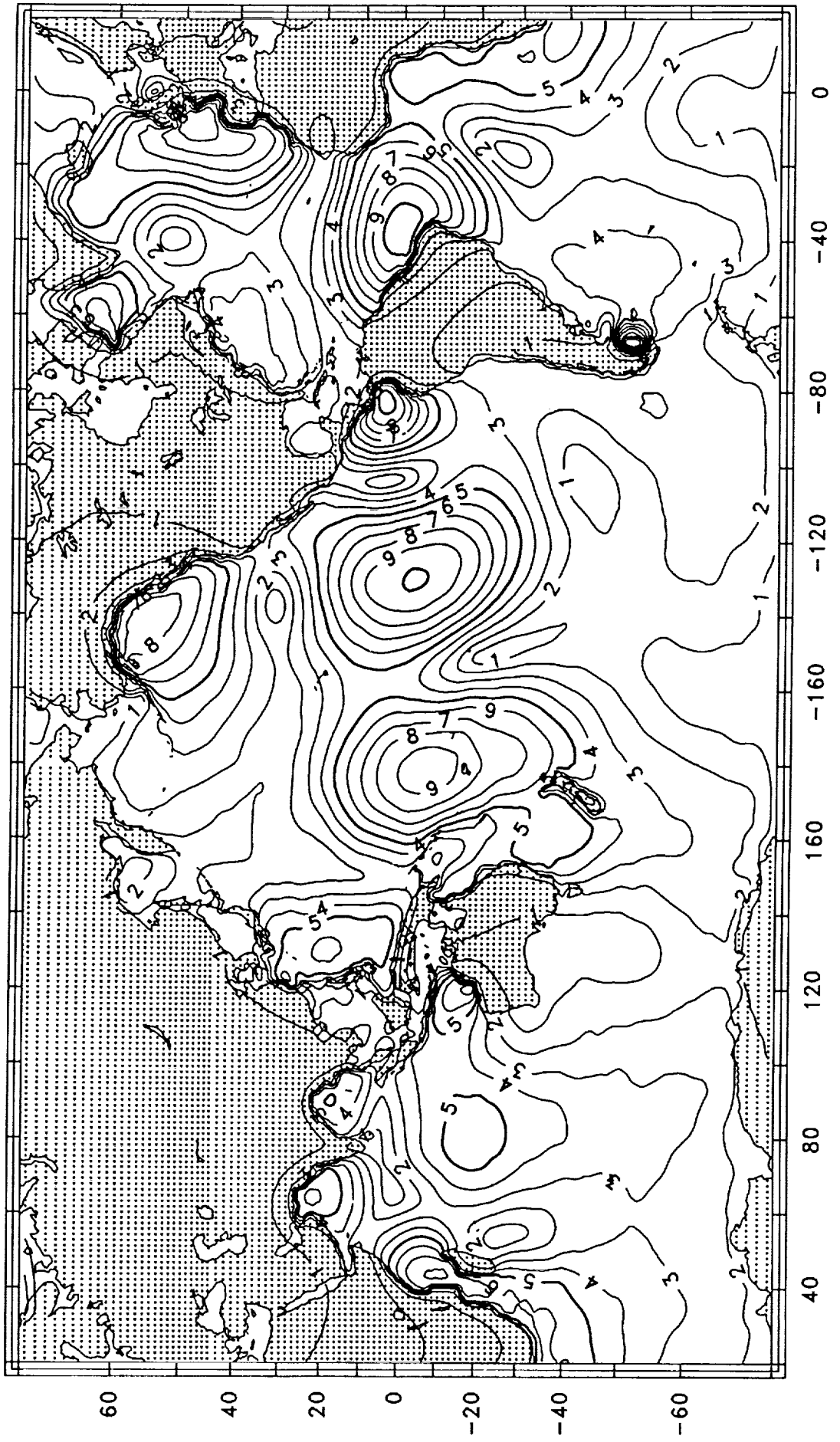
Figure 5.4a: Amplitude H_l of the N_2 load tide. Contour interval 1 mm.

34
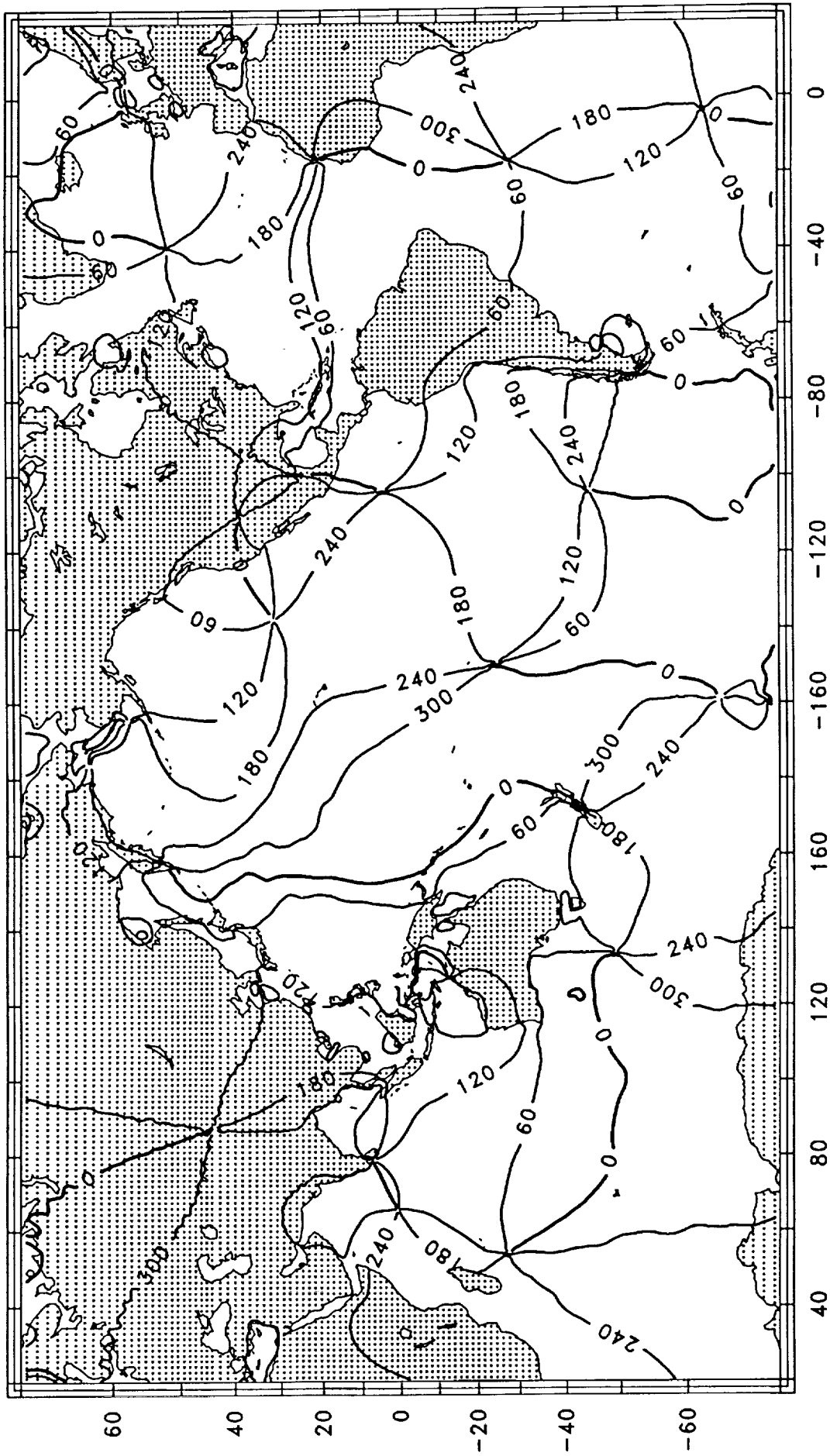
Figure 5.4b: Greenwich phase G_l of the N_2 load tide. Contour interval 60°.
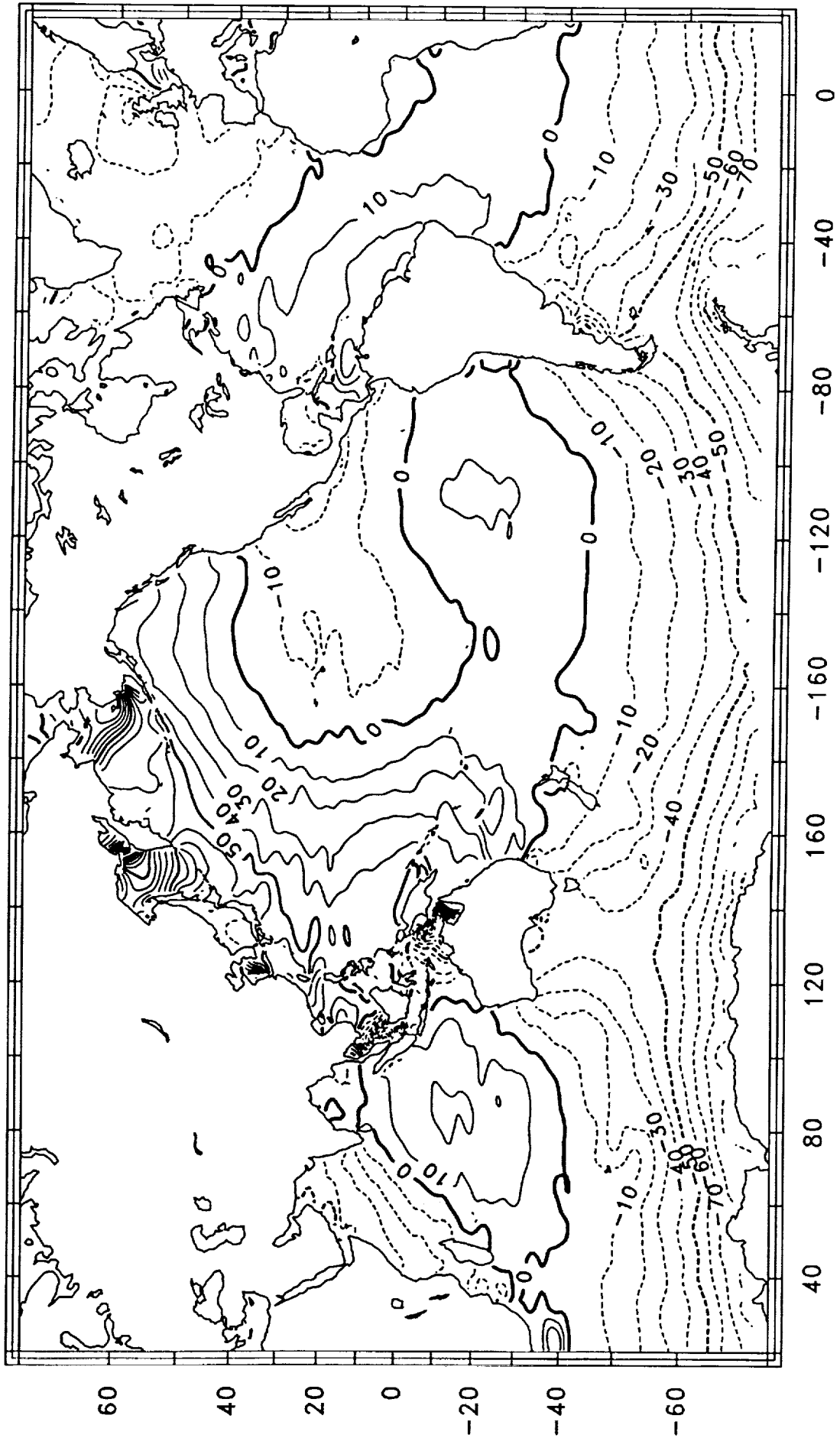
Figure 6.1a: Real component X' of the local admittance of the O_1 altimetric tide, in percent. Dashed contours are negative.
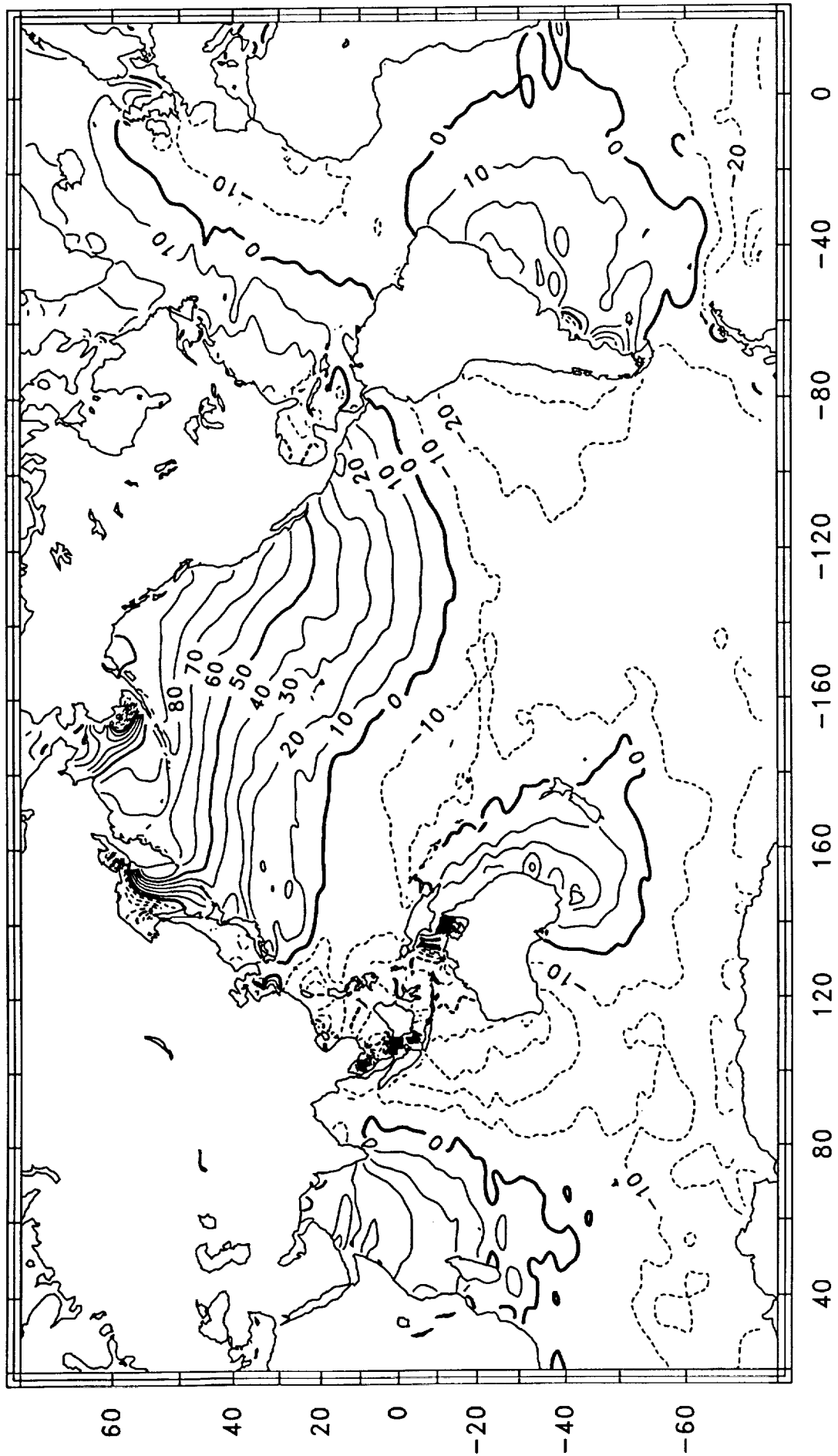
Figure 6.1b: Imaginary component Y' of the local admittance of the O_1 altimetric tide, in percent. Dashed contours are negative.
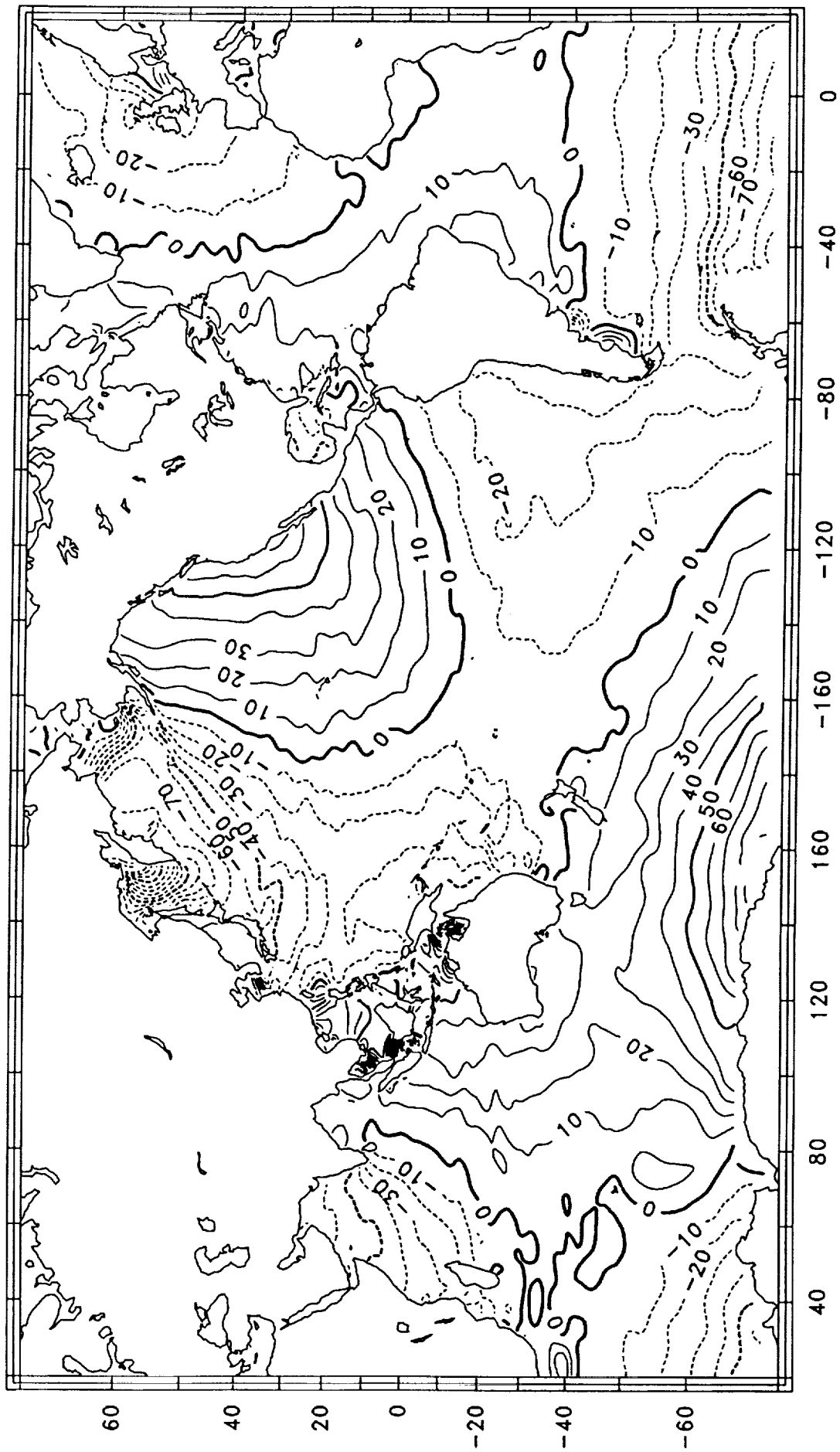
Figure 6.2a: Real component X of the Greenwich admittance of the O_1 altimetric tide, in percent. Dashed contours are negative.
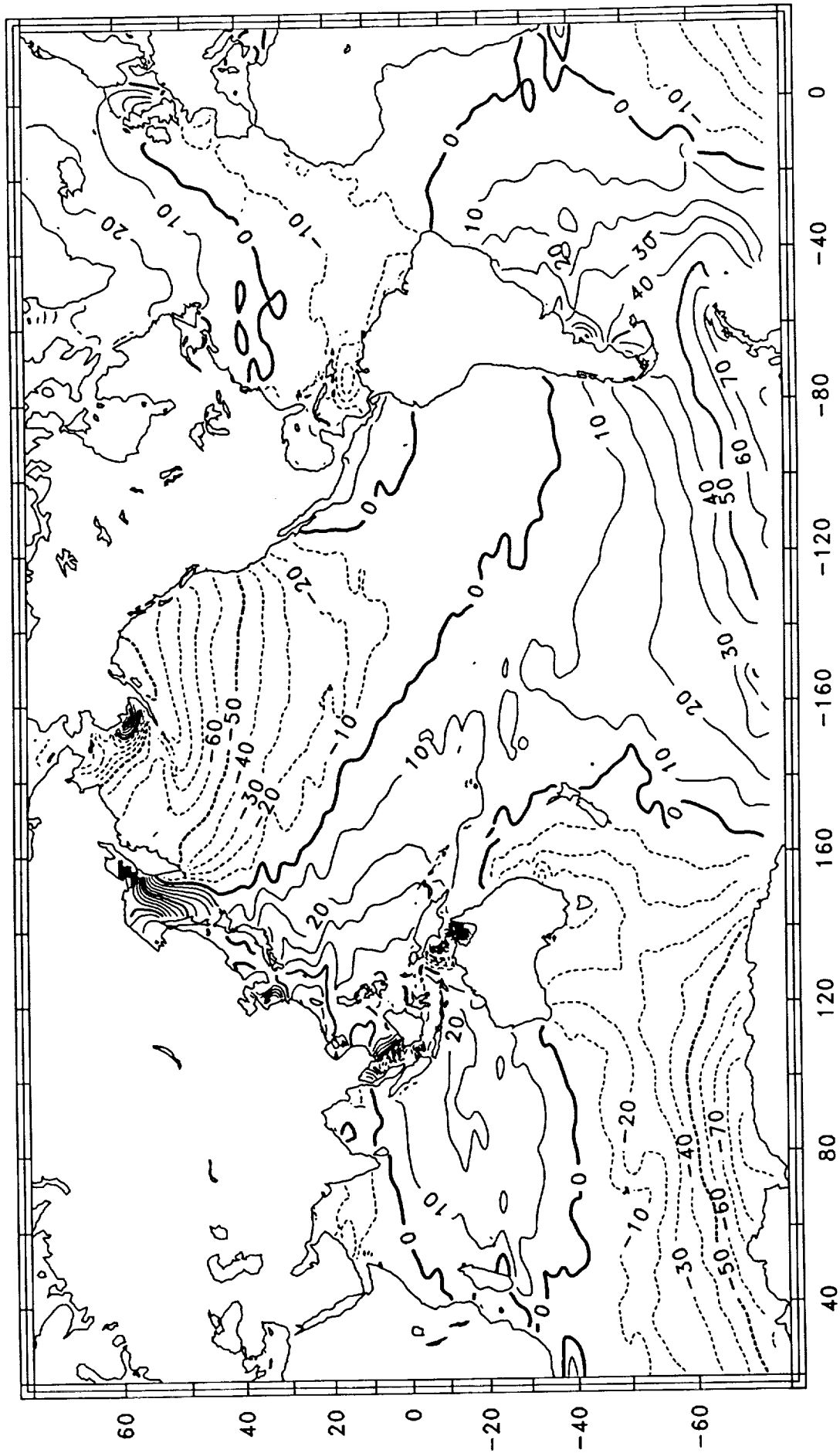
Figure 6.2b: Imaginary component Y of the Greenwich admittance of the O_1 altimetric tide, in percent. Dashed contours are negative.
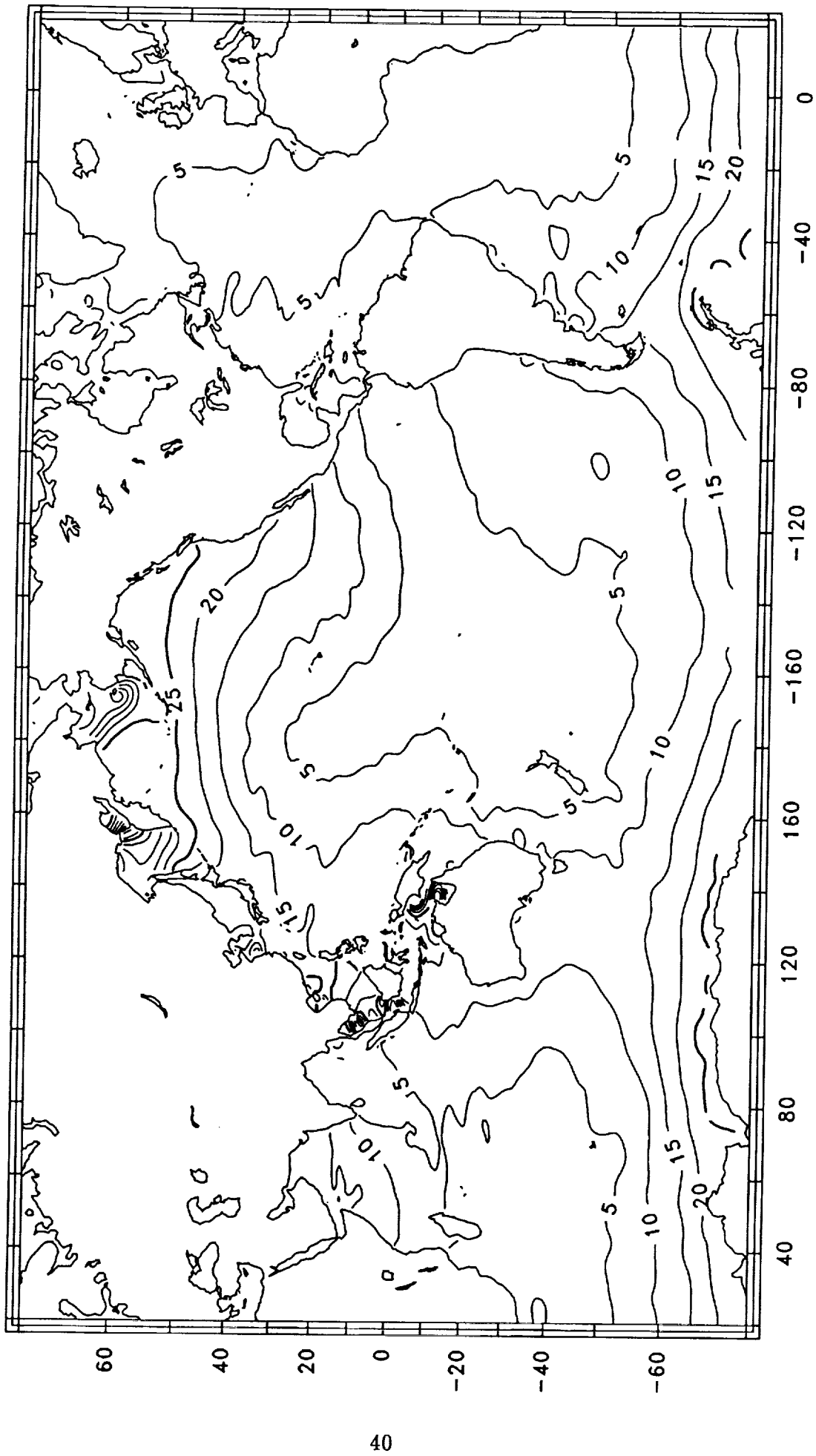
Figure 6.3a: Amplitude H of the O_1 ocean tide. Contour interval 5 cm.

40
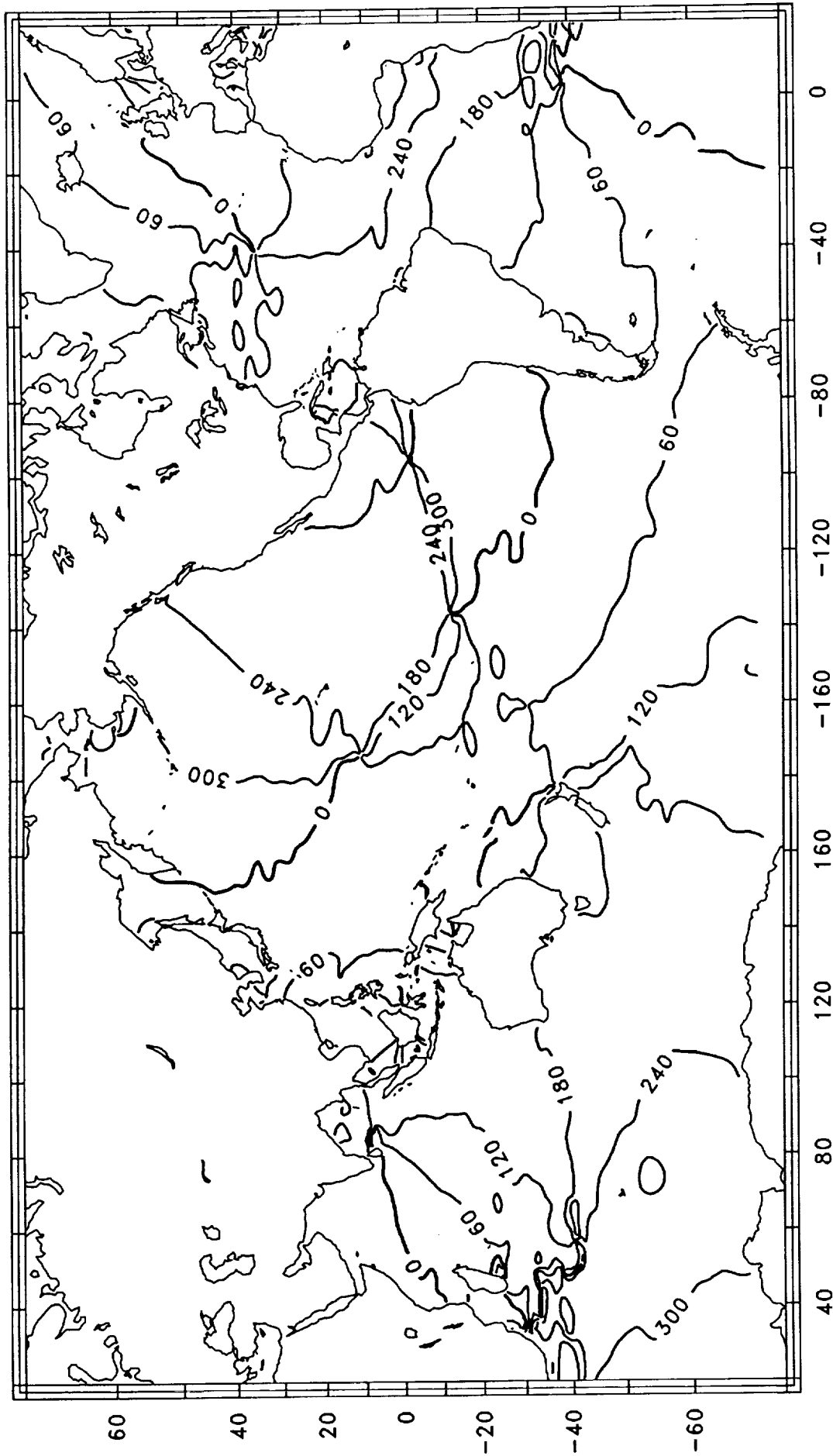
Figure 6.3b: Greenwich phase G of the O_1 ocean tide. Contour interval 60°.
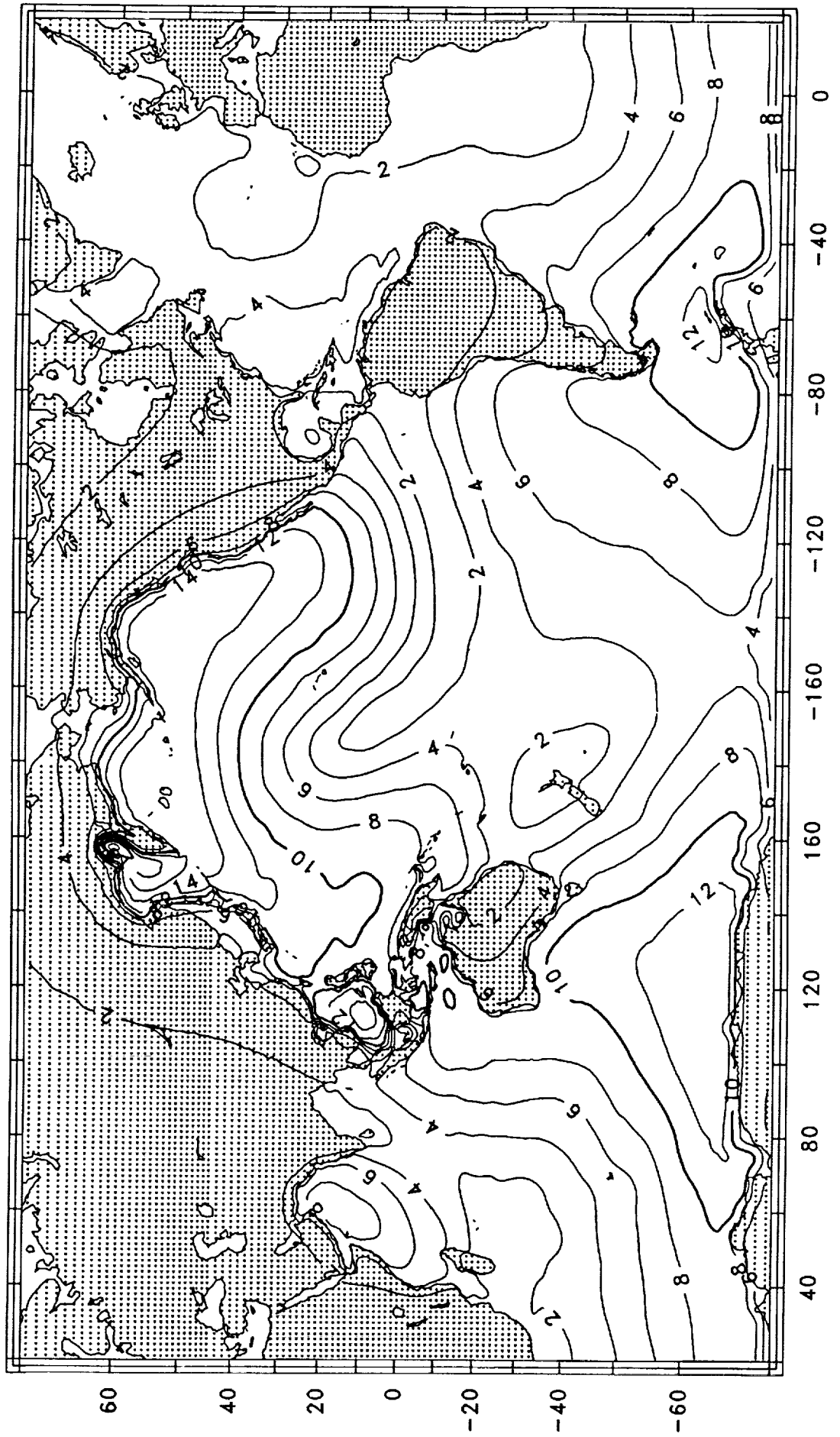
Figure 6.4a: Amplitude H_l of the O_1 load tide. Contour interval 2 mm.

42
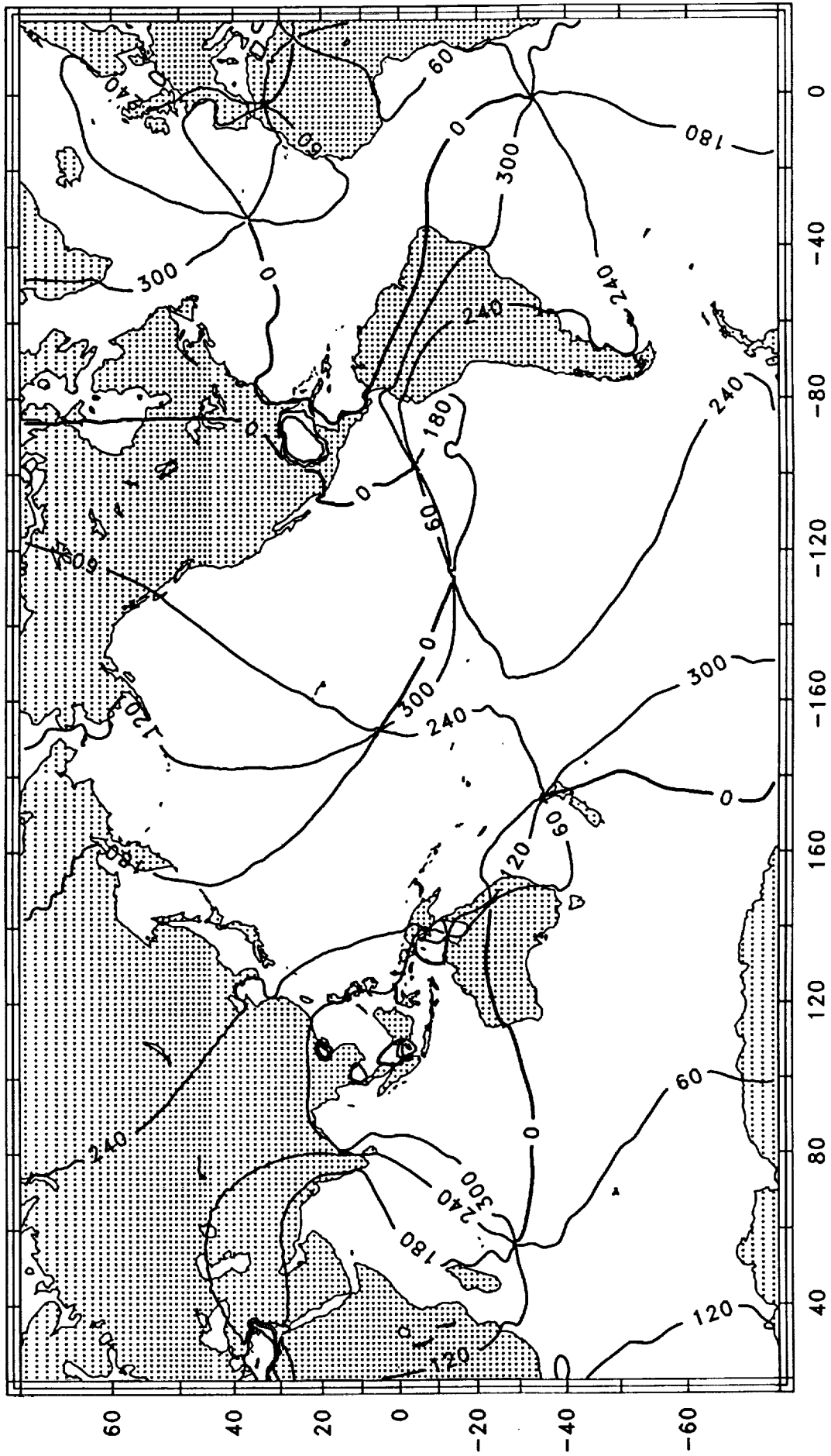
Figure 6.4b: Greenwich phase G_l of the O_1 load tide. Contour interval 60°.
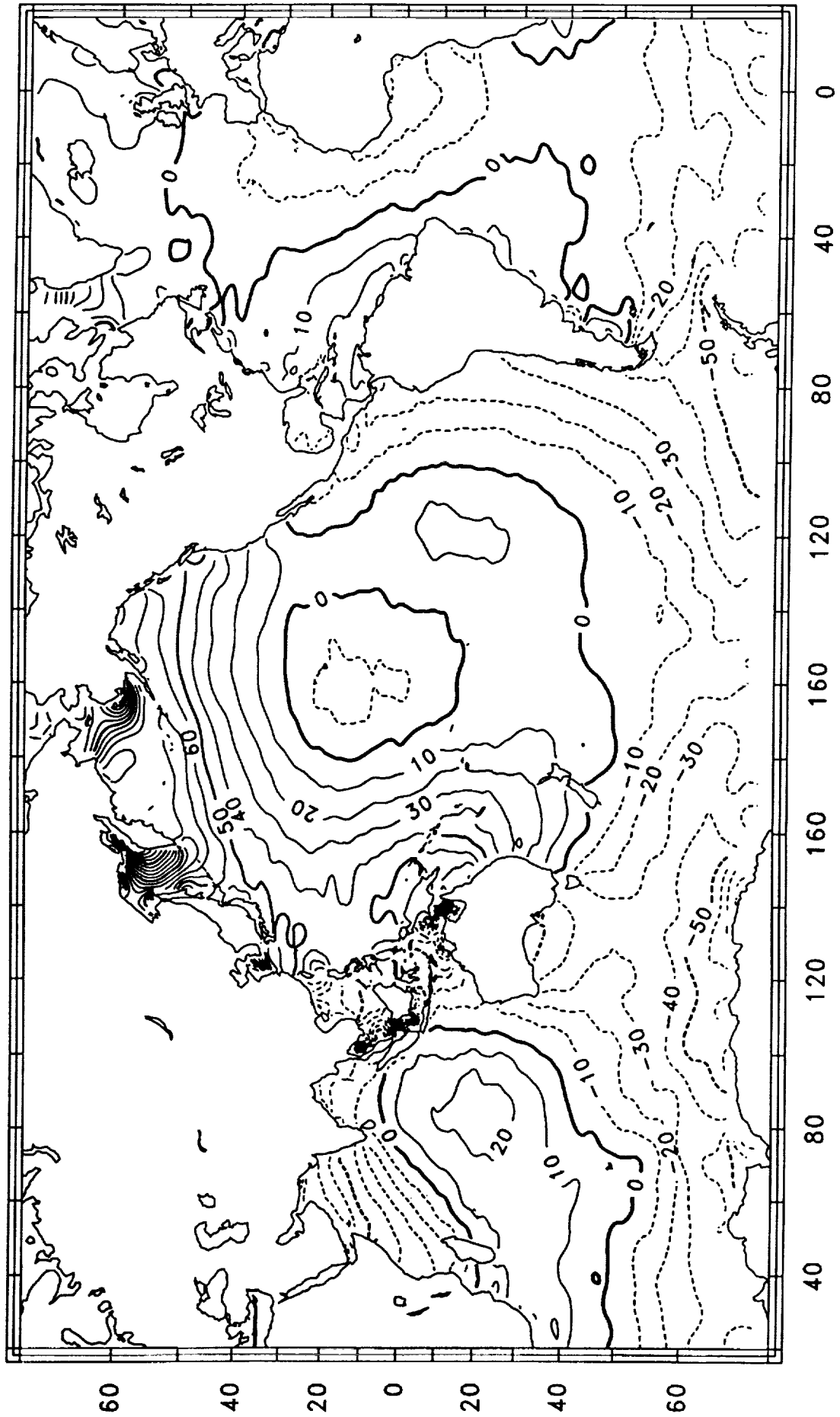
Figure 7.1a: Real component X' of the local admittance of the K_1 altimetric tide, in percent. Dashed contours are negative.
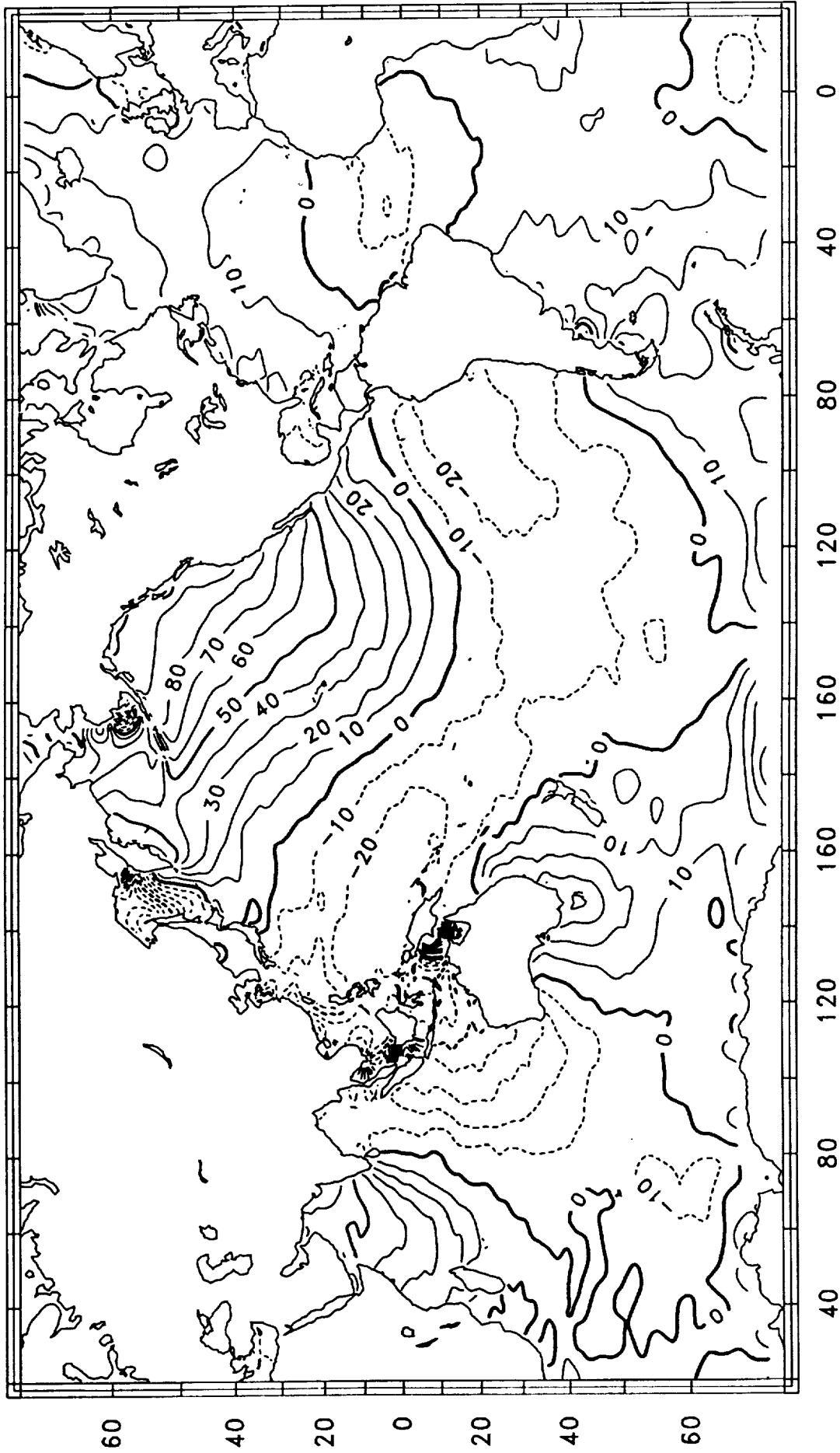
Figure 7.1b: Imaginary component Y' of the local admittance of the K_1 altimetric tide, in percent. Dashed contours are negative.
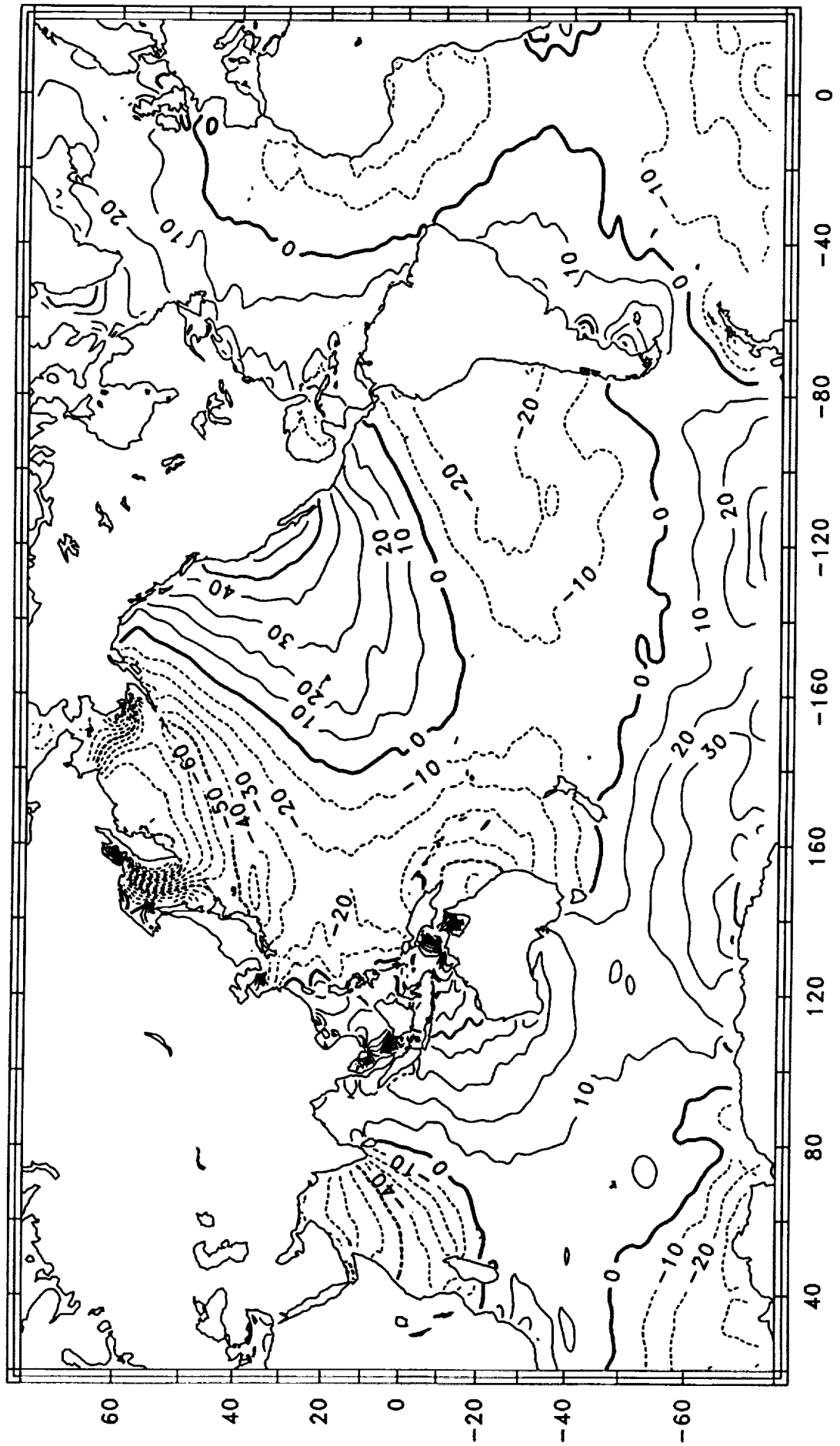
Figure 7.2a: Real component X of the Greenwich admittance of the K_1 altimetric tide, in percent. Dashed contours are negative.
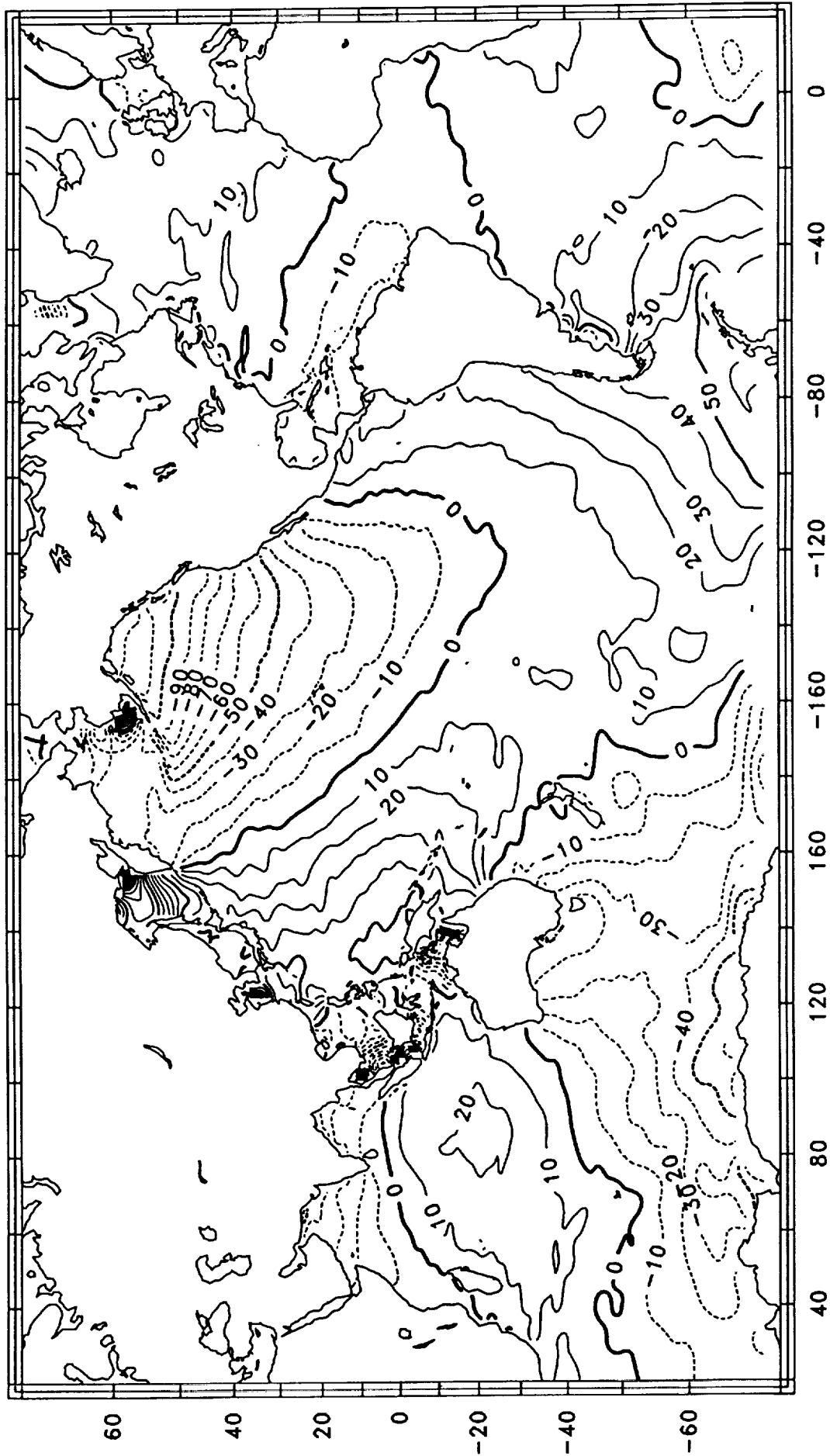
Figure 7.2b: Imaginary component Y of the Greenwich admittance of the K_1 altimetric tide, in percent. Dashed contours are negative.

47
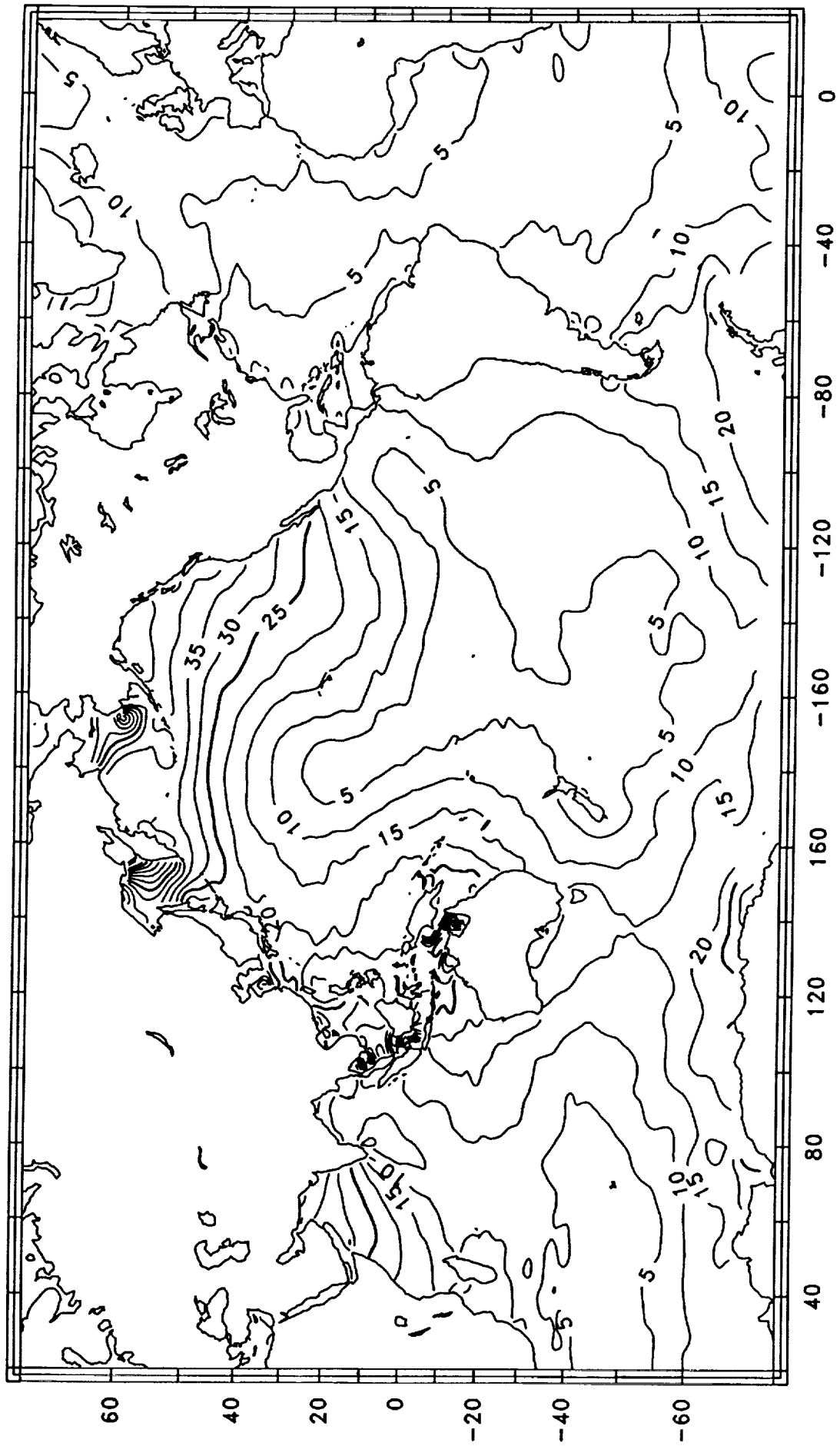
Figure 7.3a: Amplitude H of the K_1 ocean tide. Contour interval 5 cm.
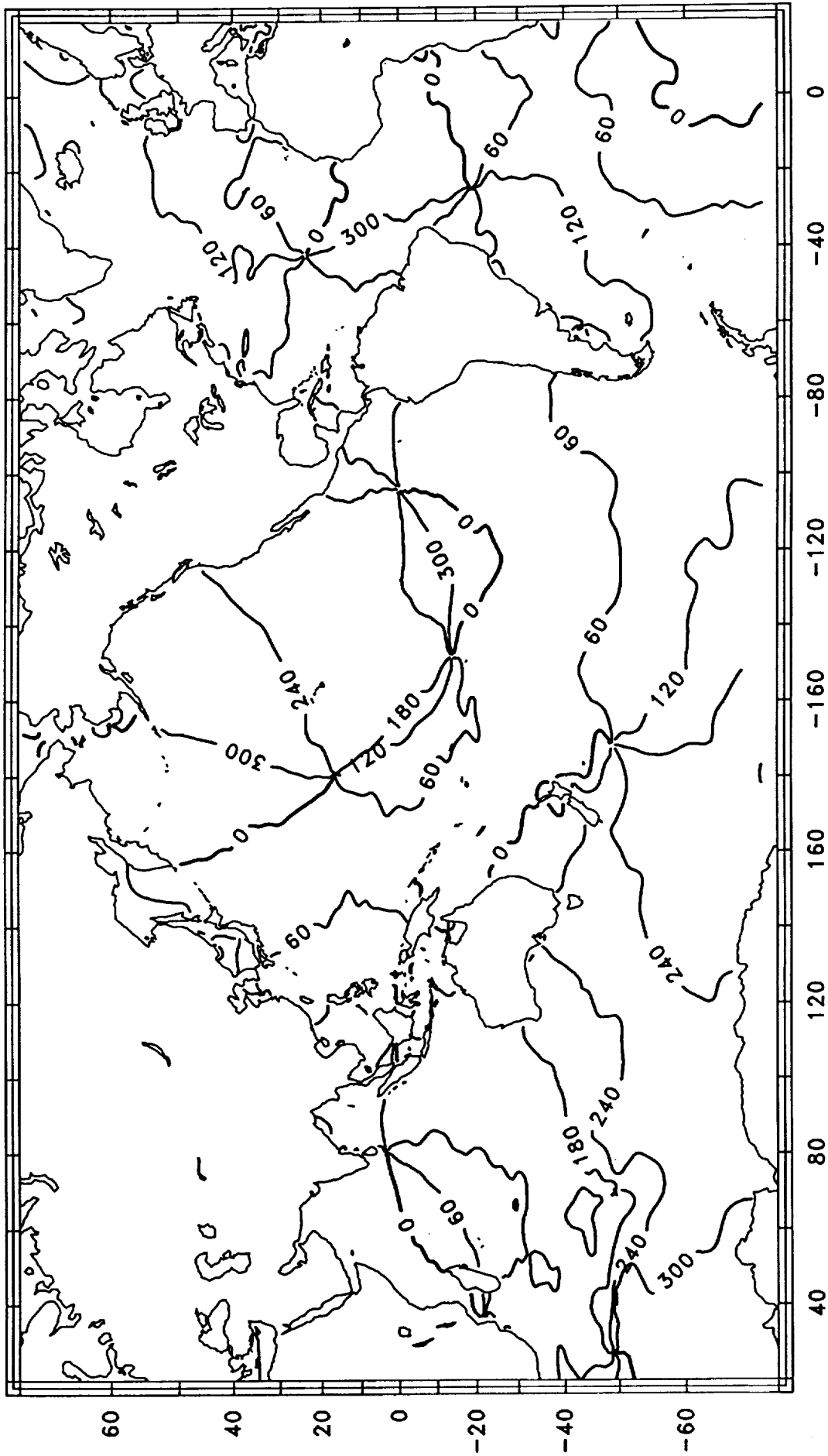
Figure 7.3b: Greenwich phase G of the K_1 ocean tide. Contour interval 60°.
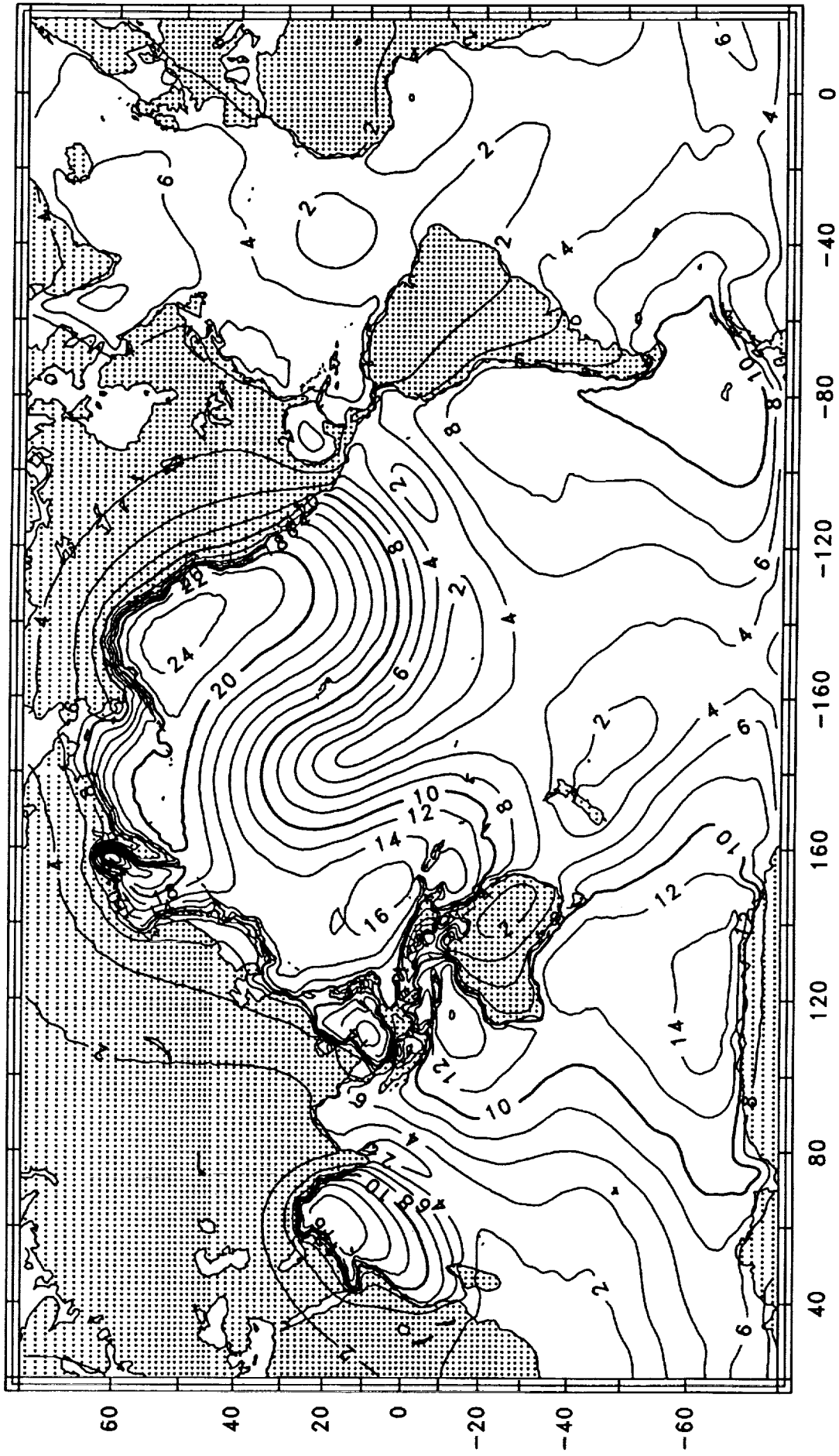
Figure 7.4a: Amplitude H_l of the K_1 load tide. Contour interval 2 mm.
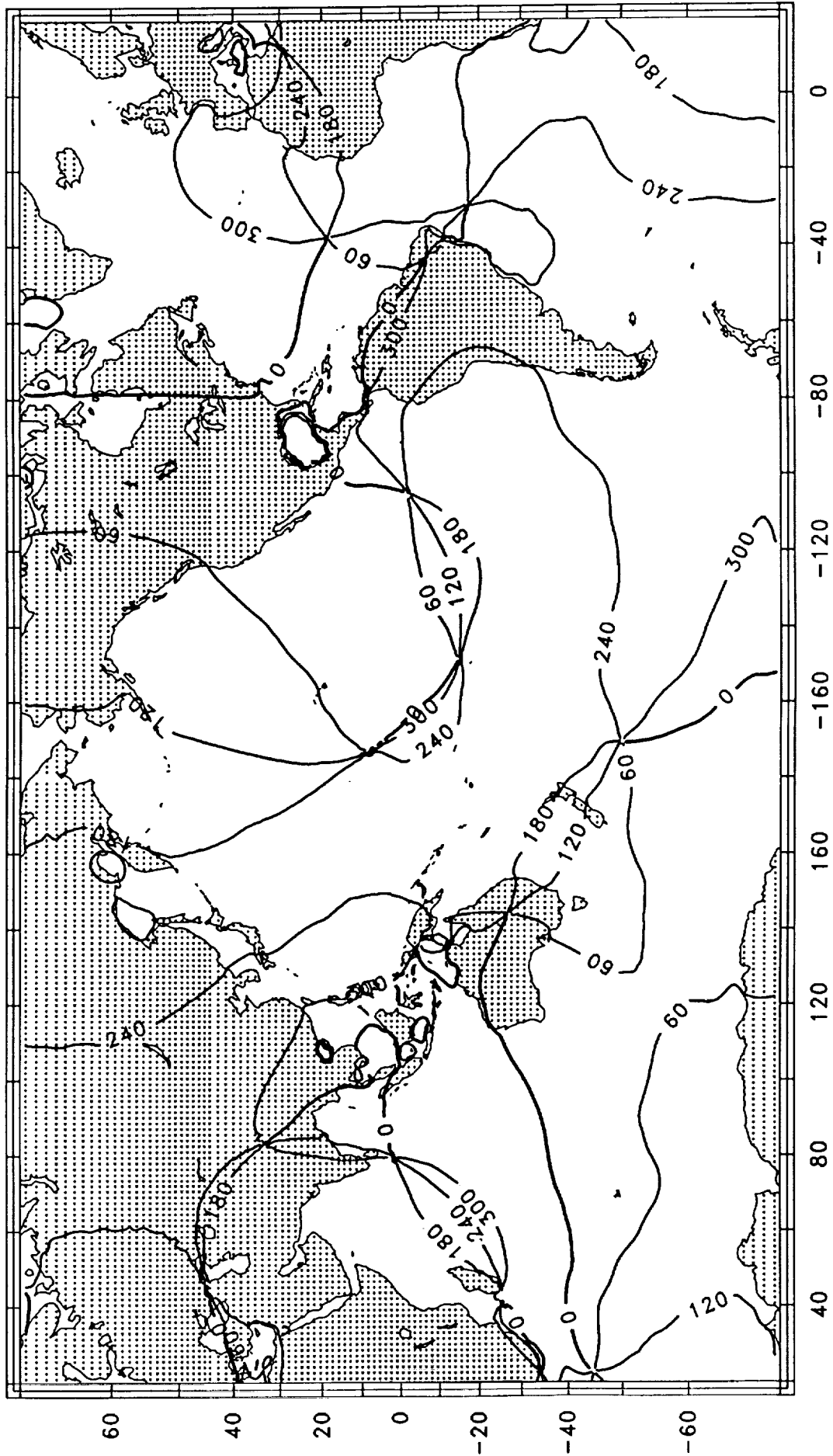
Figure 7.4b: Greenwich phase G_l of the K_1 load tide. Contour interval 60°.

5 Regional Maps

Figure pairs 8 to 14 show ocean tide maps in (H, G) notation for certain regional seas which are not clearly represented on the global scale, usually because of high amplitudes and steep gradients. Most show M_2 only, being the constituent of greatest interest, but the K_1 tide is also shown for the Australasian Seas and the Sea of Okhotsk.

The resonating Patagonian Shelf Sea (Figures 8a, b) has some extremely large amplitudes near the coast and two nodal points round which the tides rotate *contra solem*. (A third node off the coast of south Brazil, also included, is part of the main South Atlantic tide system.) Note that the amplitude contours are in steps of 10 cm from 0 to 60 cm, then in 20 cm steps upwards. Because of the large horizontal gradients and the proximity of land, including the Falkland Islands, some features may be poorly resolved or smoothed by the sampling procedure. *Cartwright and Ray* (1989) studied the energetics of this region from an early version of the CR90 analysis.

The M_2 tide in the Mediterranean Sea (Figure 9) is well known to have mostly low amplitude; it is close to the threshold of resolution against noise from altimetric and orbit errors. Parts of the Adriatic Sea and the gulf between 0°E and Gibraltar Strait are too narrow for adequate data capture and are not present in our data arrays. Therefore we do not show the nodal system in the northern Adriatic or the known rise of amplitude towards the Atlantic tide regime at Gibraltar. The figures show only the 10 cm amplitude and 120° and 180° phase lag, with indications of the intermediate values between isopleths. The rough division into 3 main basins (east, central, and west) with characteristic amplitudes and phases, together with resonant shallow gulfs of higher amplitude in the Gulf of Gabes east of Tunisia and in the northwestern Adriatic, accord qualitatively with coastal data and the dynamic model of *Dressler* (1980). Dressler's amplitudes are < 10 cm between longitudes 0° and 10°E, whereas our data there are consistently in the range 11-18 cm, probably too large in comparison to coastal data.

The M_2 tide in the South and East China Seas (Figure 10) has a great deal of tight structure, especially in the northern part, known as the Yellow Sea. (For early but detailed maps based largely on coastal gauges, see *Defant* (1961, pp. 418-426); recent hydrodynamic models are described by *Ye and Robinson* (1983) and by *Choi* (1980).) There are four *contra solem* nodes in the Yellow Sea, but smoothing and the proximity of land tend to obscure

detail here. Nevertheless, the broad tidal features of the area appear to be correctly represented by the altimetry.

Our M_2 maps for the Australasian seas (Figure 12) show the area of steep gradient of amplitude between western Australia and Java and the extent and limitations of altimetric data-retrieval in the island-studded seas of Indonesia. The large area north of Papua–New Guinea without phase contours, continued to the north in Figure 10, has phase lag everywhere between 270° and 300°, as documented elsewhere (e.g. *Schwiderski*, 1983). A nodal point is indicated inside the Gulf of Carpentaria, but our contouring algorithm has difficulty with such close-knit features in phase, emphasizing one advantage of (X, Y) plotting over (H, G) plotting. A node appears in the same Gulf for K_1, plotted in Figure 11. We have added a map for K_1 to this region because of its well-known interplay of daily and half-daily tides between the Pacific and Indian Oceans. For general descriptions of tidal knowledge of Indonesian seas, see *Defant* (1961, pp. 417–421) and *Bogdanov and Nefedyev* (1961, 62).

Turning finally to the northern part of the Asian Pacific border seas, Figures 13a, b and 14a, b show respectively K_1 and M_2 contours in the Okhotsk Sea area. The Okhotsk Sea is known for its strong diurnal response (Figure 14.1); it also has large semidiurnal response and a number of semidiurnal nodes near the coast *(Defant, 1961, pp. 430–433)*. The nodal points are not well resolved by the altimetry (Figure 14). The tides in the Japan Sea have low amplitude, confirmed by both Figures 14 and 10; few, if any, hydrodynamic models are available for the Japan Sea. *Defant* (1961, pp. 426–430) gives a general account of mid-century knowledge.
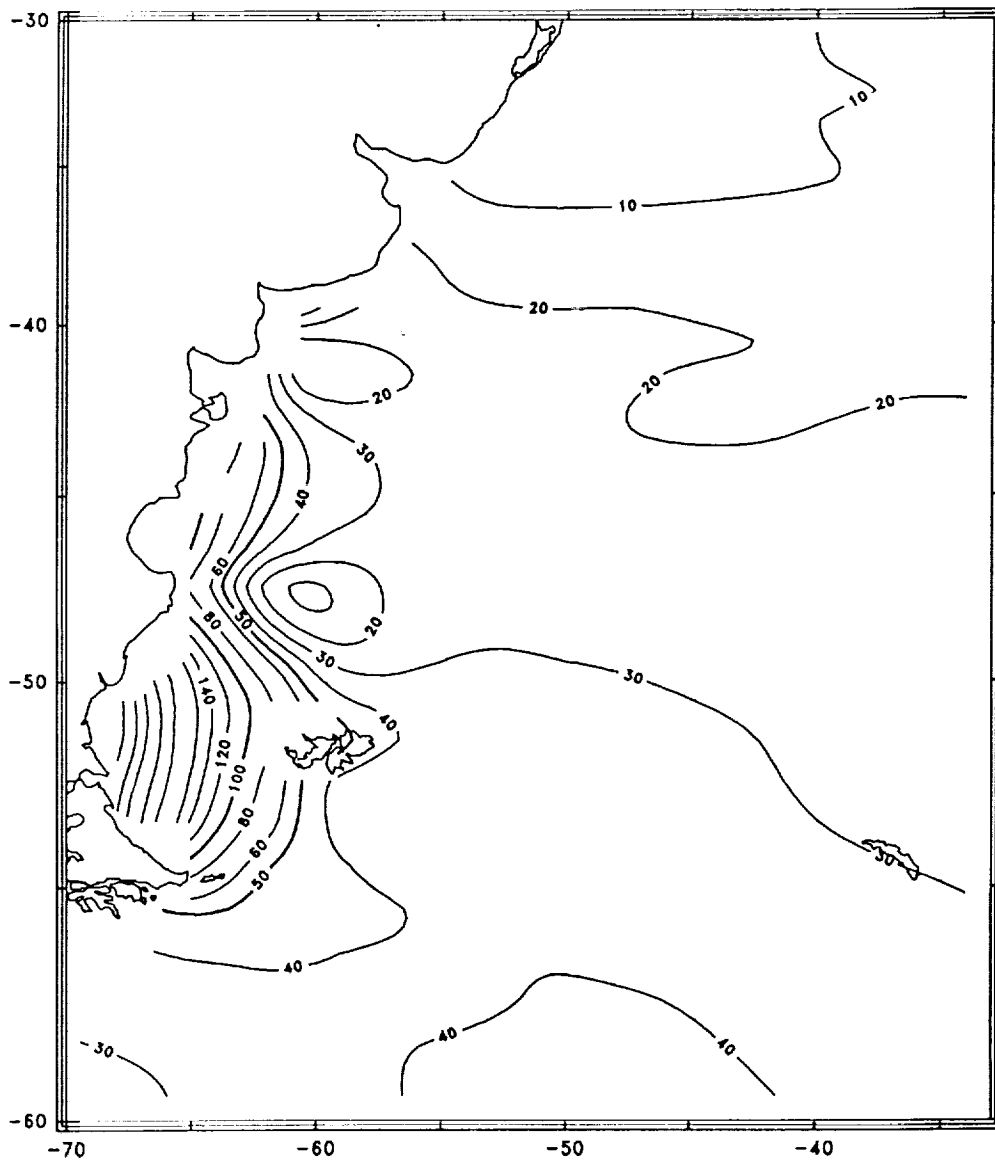
Figure 8a: M_2 ocean tide on the Patagonian Shelf.
Amplitude contours 10 (10) 60 (20) 260 cm.

54
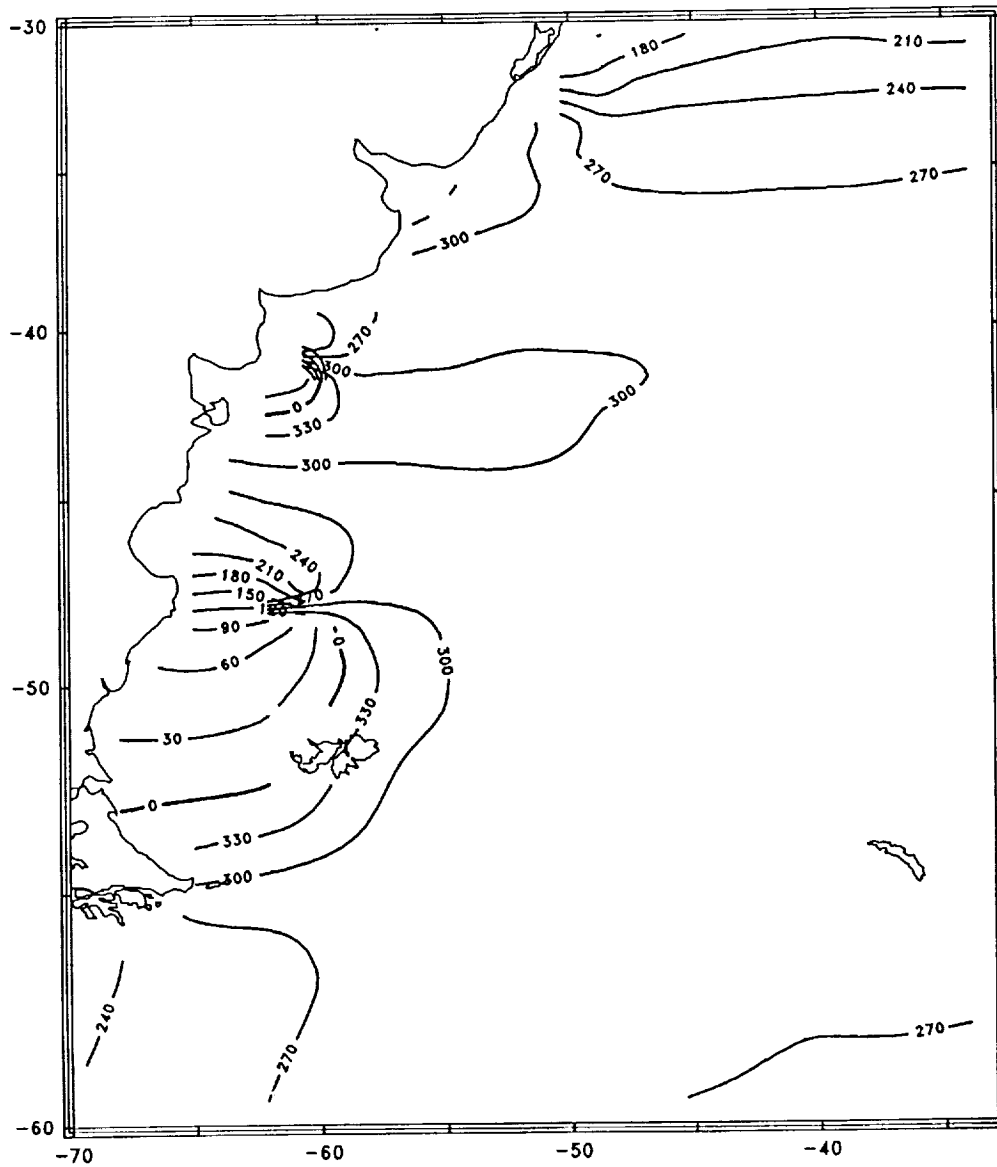
Figure 8b: M$_2$ ocean tide on the Patagonian Shelf.
Greenwich phase lag contours 0 (30) 360 degrees.
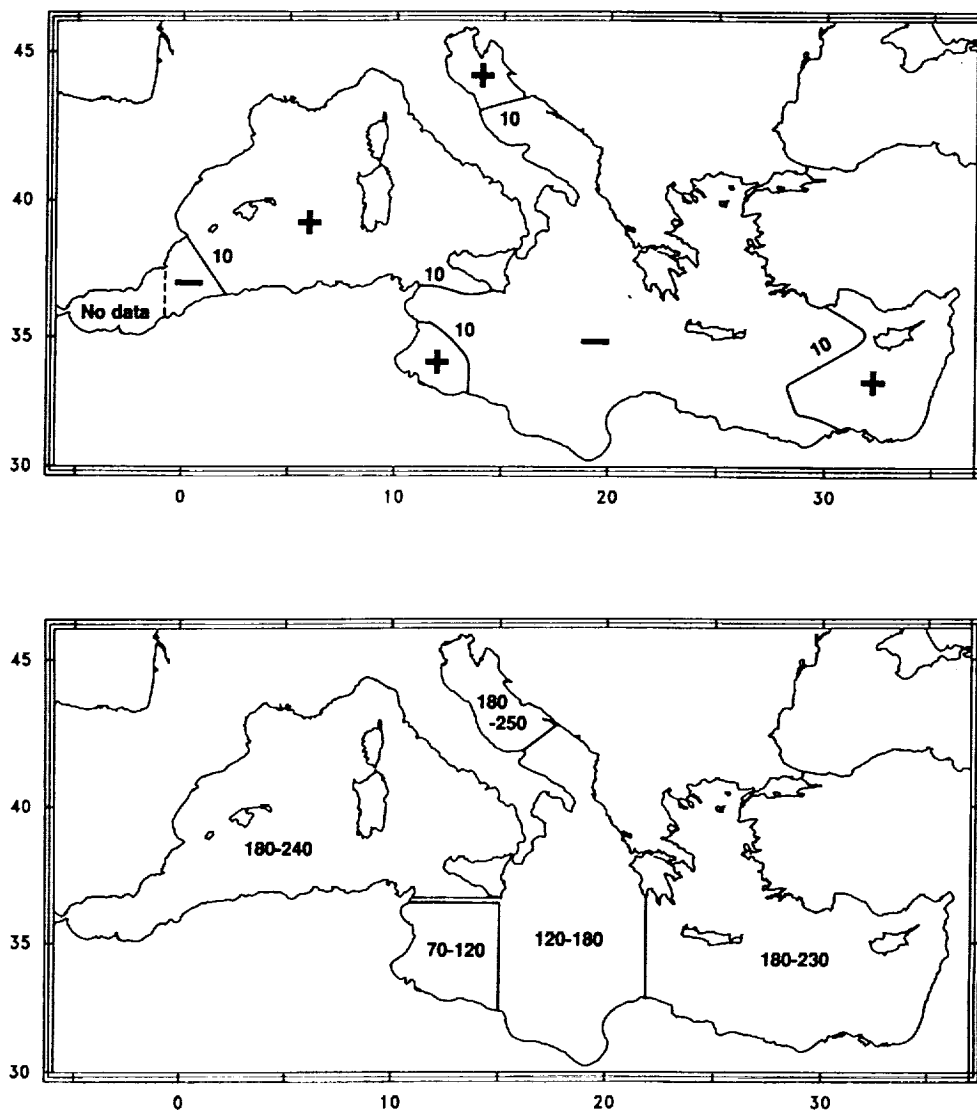
Figure 9: M_2 tide amplitude (top) and phase lag (bottom) in the Mediterranean Sea. Only 10 cm amplitude contours are shown, with + indicating > 10 cm and − indicating < 10 cm. Phase contours mark approximate position of 120° and 180° phase lags, with figures indicating range of values between contours and coastline.
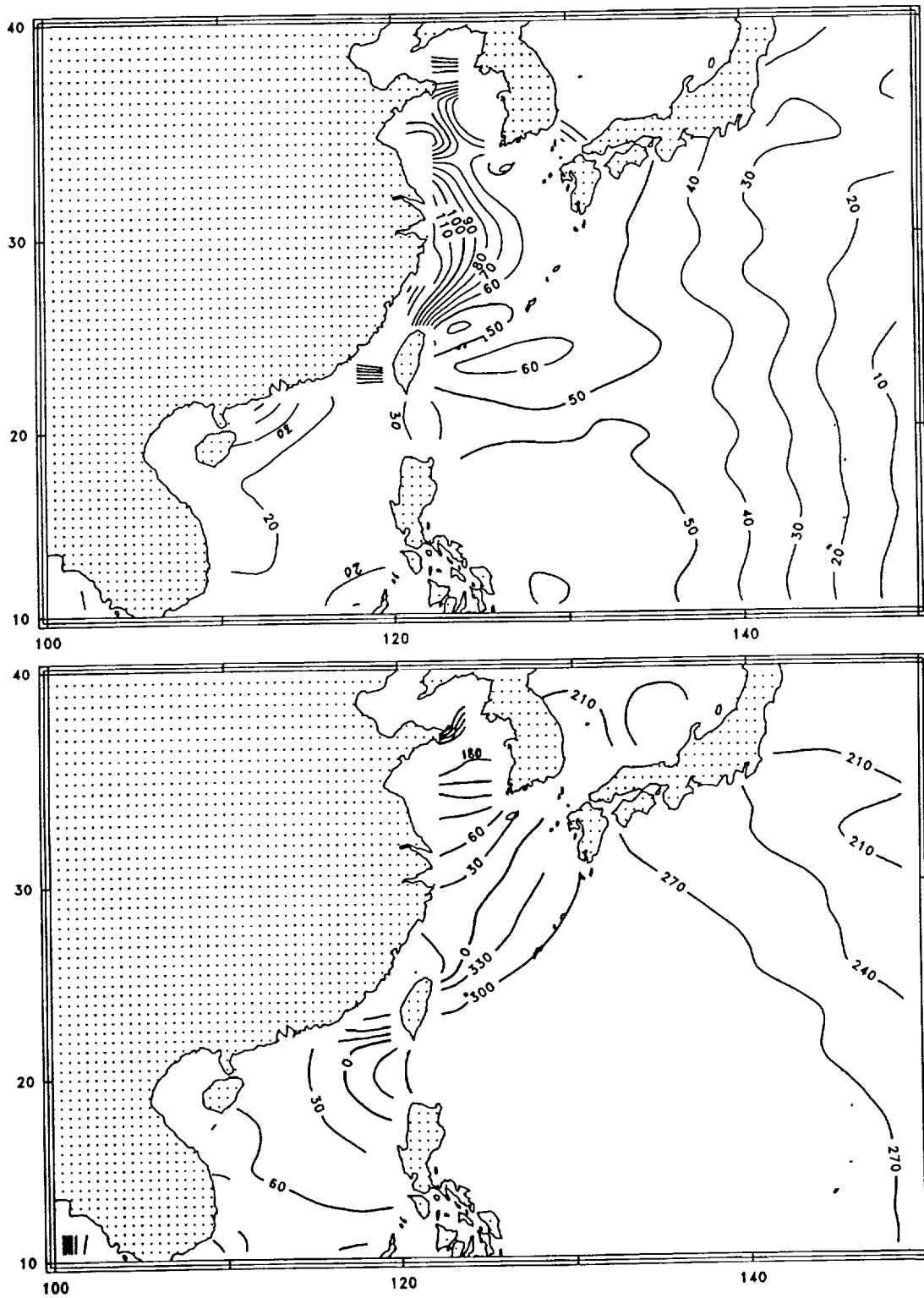
Figure 10: M_2 tide in the China Sea region. Amplitudes (top) in cm; Green-wich phase lags (bottom) in degrees.
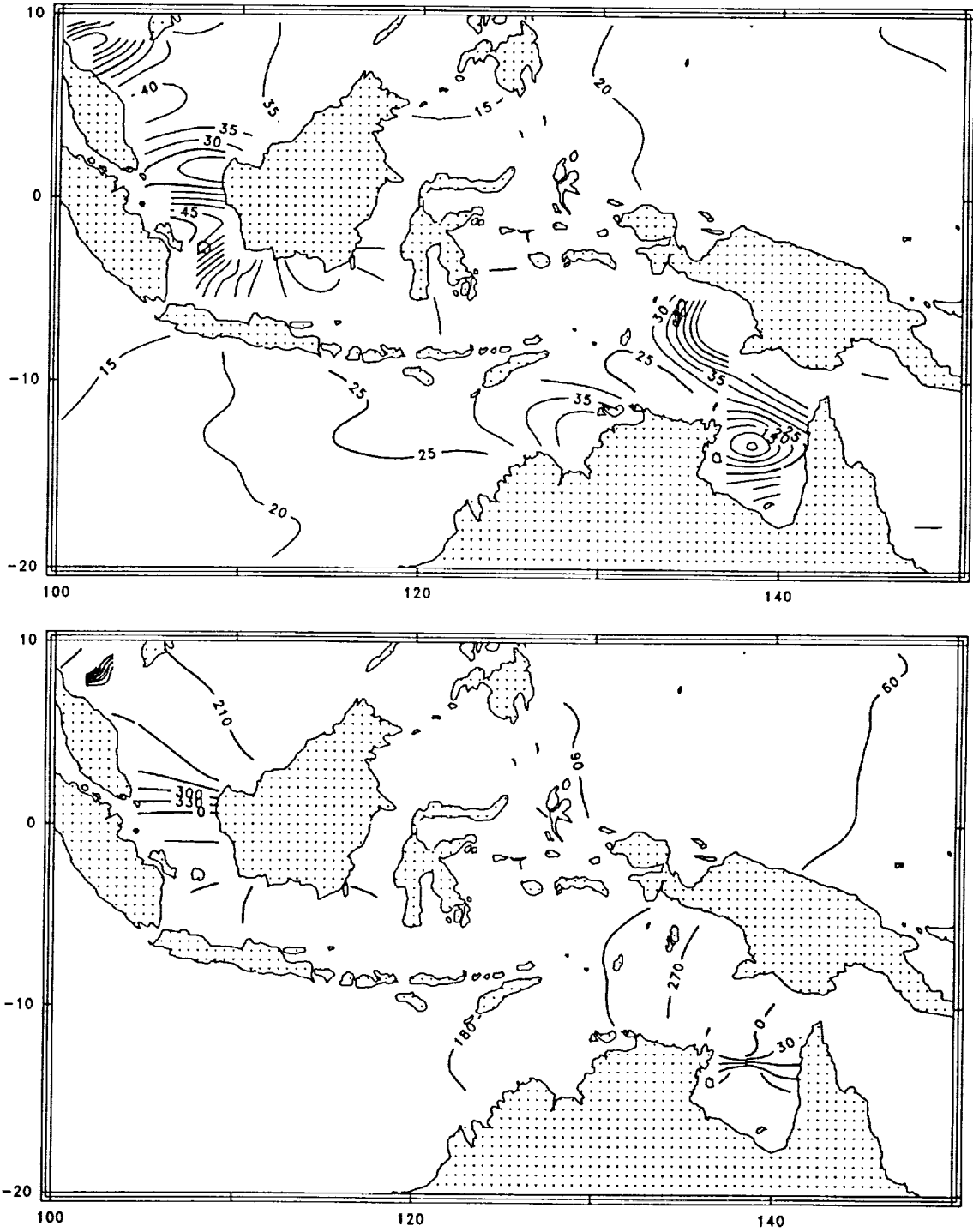
Figure 11: K_1 tide in the Australasian seas. Amplitudes (top) in cm; Greenwich phase lags (bottom) in degrees.
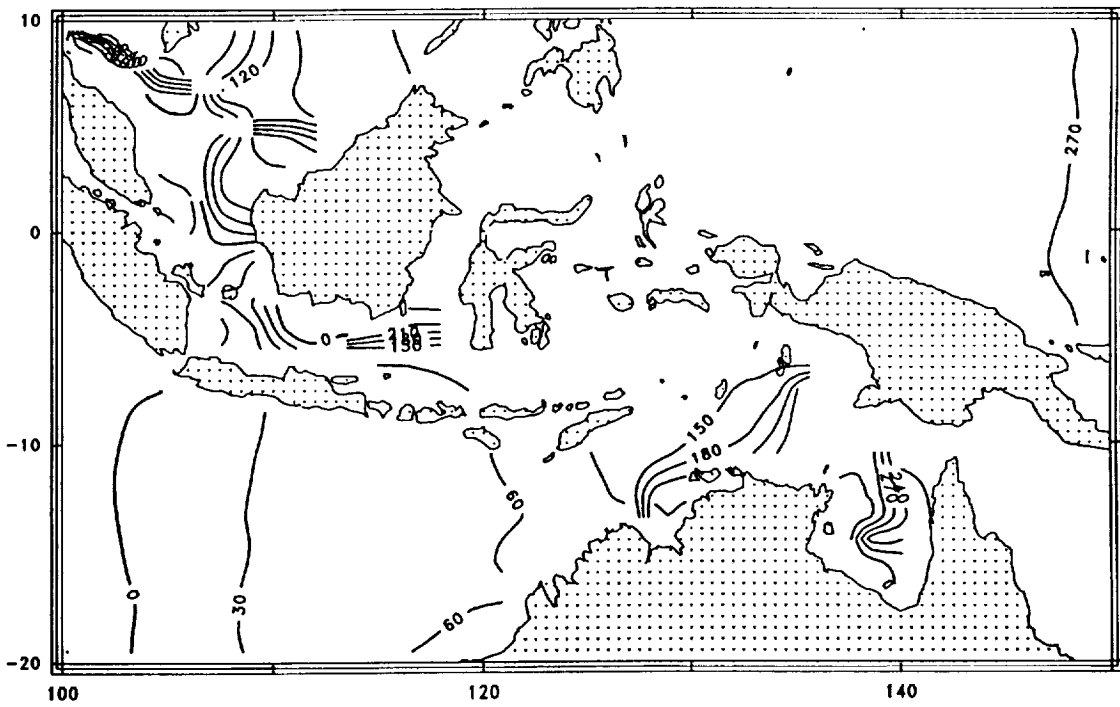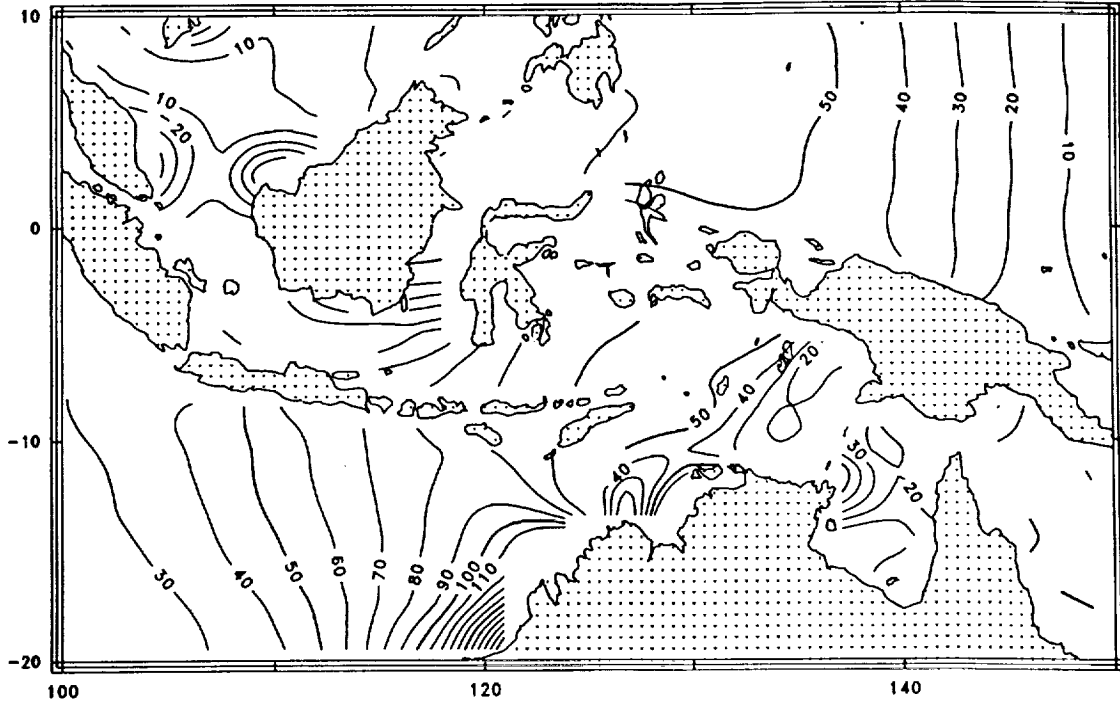
Figure 12: M_2 tide in the Australasian seas. Amplitudes (top) in cm; Greenwich phase lags (bottom) in degrees.
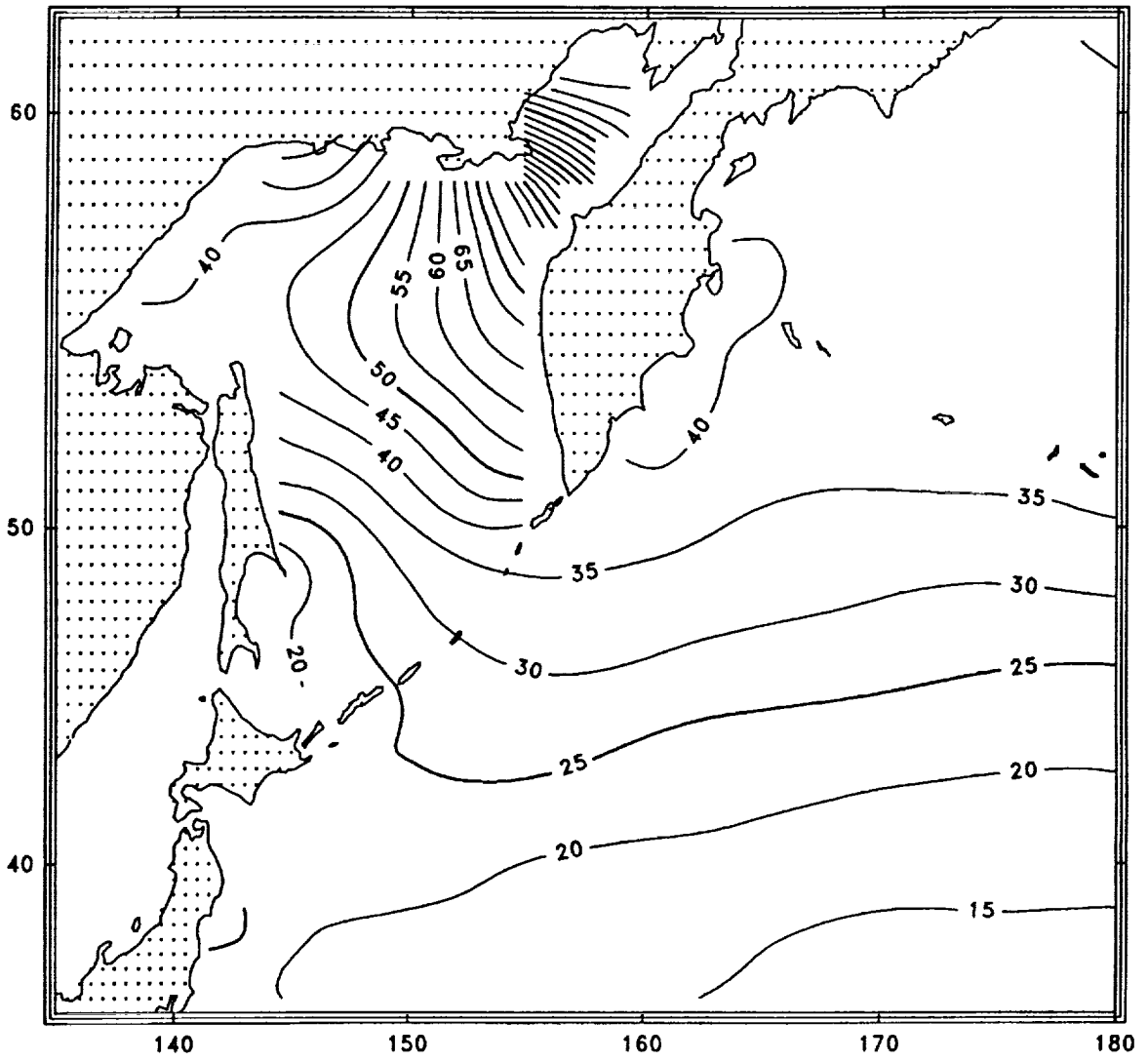
Figure 13a: K_1 tide in the Okhotsk Sea and adjacent seas.
Amplitudes in cm.
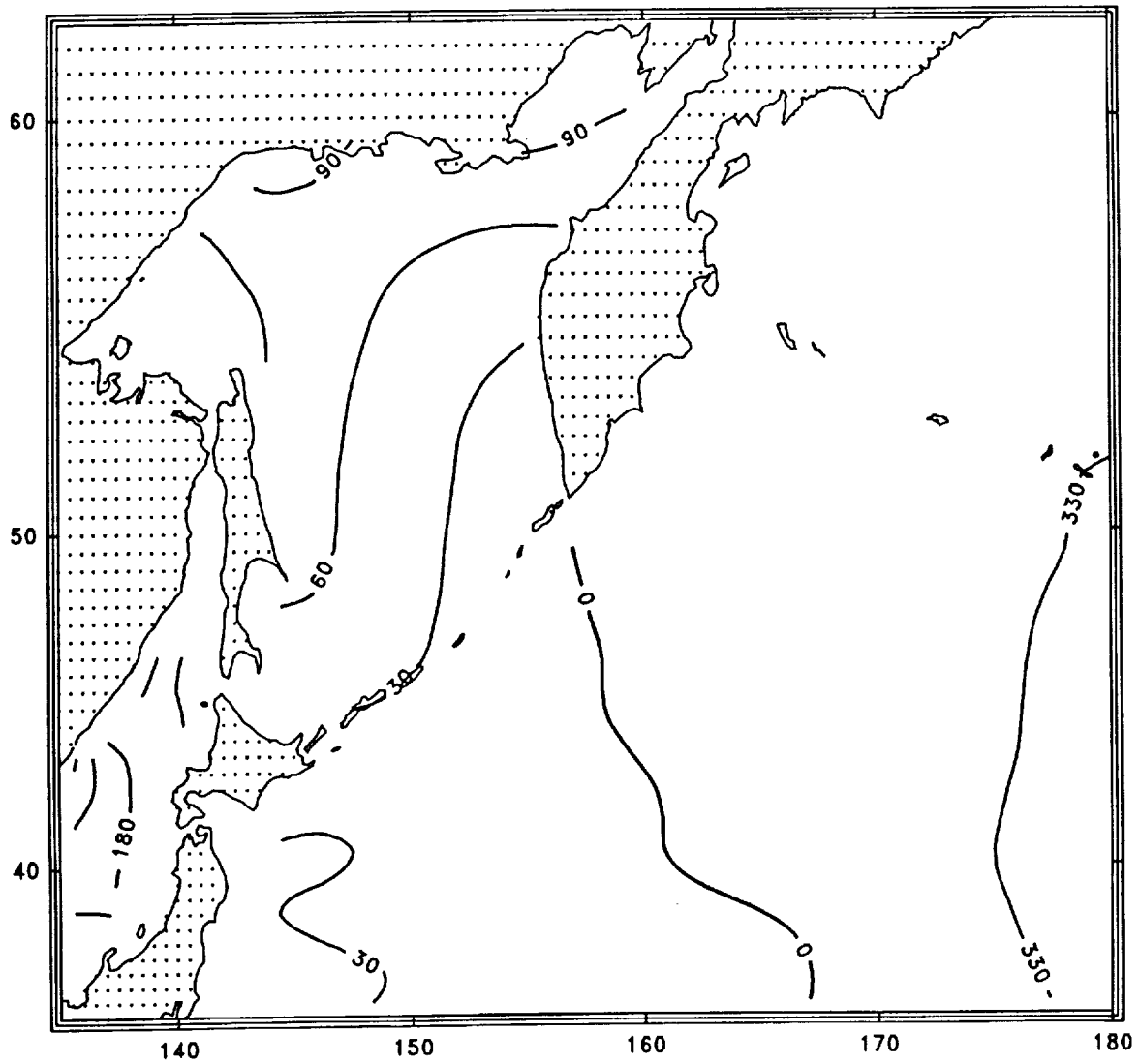
Figure 13b: K$_1$ tide in the Okhotsk Sea and adjacent seas.
Greenwich phase lags in degrees.

61
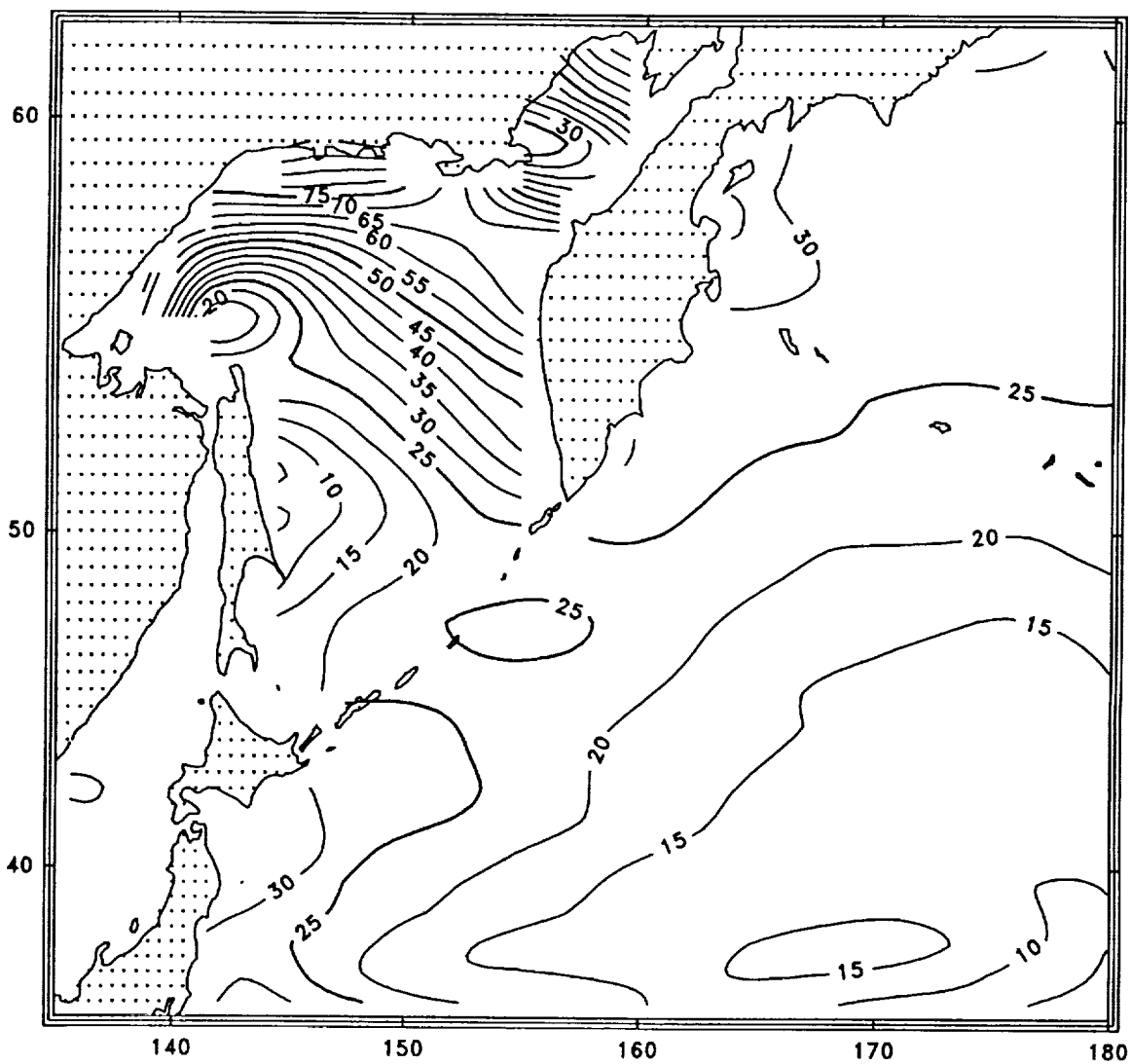
Figure 14a: M_2 tide in the Okhotsk Sea and adjacent seas.
Amplitudes in cm.

62
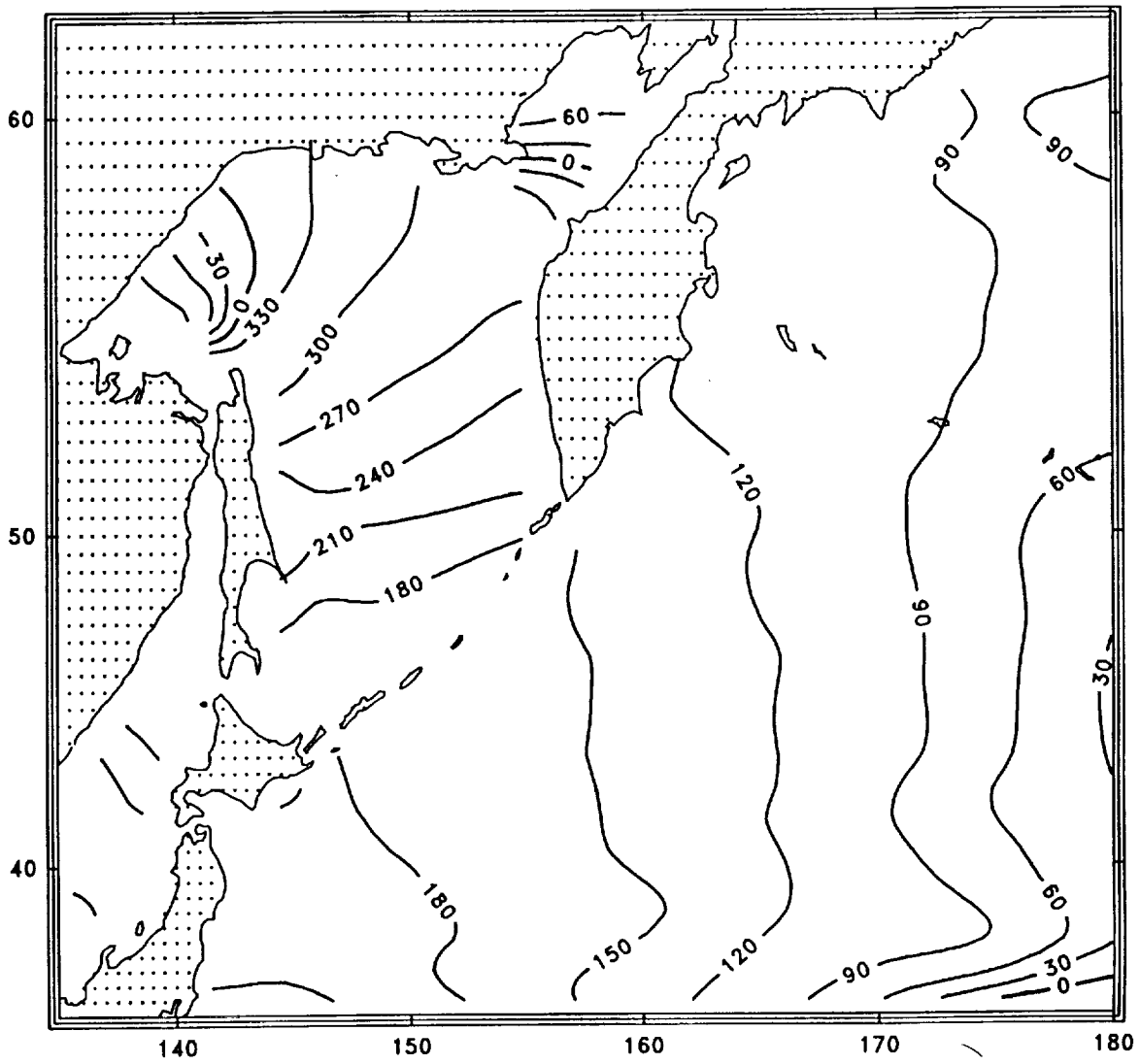
Figure 14b: M_2 tide in the Okhotsk Sea and adjacent seas.
Greenwich phase lags in degrees.

63

6 Expansions in Spherical Harmonics

For a number of applications it is desirable to have spherical harmonic expansion coefficients for the major ocean tide constituents. Tables 2–7 below list the lowest degree and order spherical harmonic coefficients for the constituents O_1, P_1, K_1, N_2, M_2, and S_2, computed from our global arrays of admittances, with adjustment for the load tide as explained in the Appendix to CR91 (i.e., the coefficients represent the pure ocean tide). These harmonics were computed through degree and order 122, the highest number appropriate for Geosat's longitude spacing of $360°/244$, but for space limitations, only those coefficients through degree and order 8 are presented here.

As in *Ray and Sanchez* (1989), we have found it convenient to express the spherical harmonic series in the following convention:

$$\frac{1}{2} \sum_{n=0}^{N} a_{n0} \bar{P}_n^0 (\cos \theta) + \sum_{n=1}^{N} \sum_{m=1}^{n} (a_{nm} \cos m\phi - b_{nm} \sin m\phi) \bar{P}_n^m (\cos \theta). \quad (10)$$

The $\bar{P}_n^m(\mu)$ are the normalized associated Legendre functions, the first few of which are given in Table 1.

For any particular tidal constituent, the in-phase and quadrature components $H \cos G$ and $H \sin G$ are expanded as follows:

$$H \cos G = \sum_{n=0}^{N} {\sum_{m=0}^{n}}' (a_{nm} \cos m\phi - b_{nm} \sin m\phi) \bar{P}_n^m (\cos \theta)$$

$$H \sin G = \sum_{n=0}^{N} {\sum_{m=0}^{n}}' (c_{nm} \cos m\phi - d_{nm} \sin m\phi) \bar{P}_n^m (\cos \theta)$$

where the prime on the second summation indicates that the first term is multiplied by $\frac{1}{2}$, in agreement with (10). The coefficients a_{nm}, b_{nm}, c_{nm}, and d_{nm} are listed in the following tables in units of millimeters.

Owing to conservation of mass, the terms a_{00} and c_{00} should in theory be zero. All six listed constituents, however, are found to violate this condition, the most serious discrepancy being a_{00} for K_1. Nonconservation of mass in tide models is a common annoyance and it is here as likely induced by the neglect of seas in latitudes greater than $70°$ as by errors in the derived admittance maps.

Table 1: Normalized Associated Legendre Functions.

$$\bar{P}_0^0(x) = \sqrt{(1/2)}$$
$$\bar{P}_1^0(x) = \sqrt{(3/2)}\,x$$
$$\bar{P}_1^1(x) = \sqrt{(3/4)}\,(1 - x^2)^{1/2}$$
$$\bar{P}_2^0(x) = \sqrt{(5/2)}\,(\tfrac{3}{2}x^2 - \tfrac{1}{2})$$
$$\bar{P}_2^1(x) = \sqrt{(5/12)}\,3x(1 - x^2)^{1/2}$$
$$\bar{P}_2^2(x) = \sqrt{(5/48)}\,3(1 - x^2)$$
$$\bar{P}_3^0(x) = \sqrt{(7/2)}\,(\tfrac{5}{2}x^3 - \tfrac{3}{2}x)$$
$$\bar{P}_3^1(x) = \sqrt{(7/24)}\,(\tfrac{15}{2}x^2 - \tfrac{3}{2})(1 - x^2)^{1/2}$$
$$\bar{P}_3^2(x) = \sqrt{(7/240)}\,15x(1 - x^2)$$
$$\bar{P}_3^3(x) = \sqrt{(7/1440)}\,15(1 - x^2)^{3/2}$$

For comparisons to other studies, the following formulae convert our tabulated coefficients to the unnormalized coefficients often used in satellite geodesy:

$$\left.\begin{array}{l} D_{nm}^{\pm} \cos \psi_{nm}^{\pm} = \tfrac{1}{2}(a_{nm} \pm d_{nm})N_n^m \\[6pt] D_{nm}^{\pm} \sin \psi_{nm}^{\pm} = \tfrac{1}{2}(c_{nm} \mp b_{nm})N_n^m \end{array}\right\} \quad \text{for species 2}$$

$$\left.\begin{array}{l} D_{nm}^{\pm} \sin \psi_{nm}^{\pm} = -\tfrac{1}{2}(a_{nm} \pm d_{nm})N_n^m \\[6pt] D_{nm}^{\pm} \cos \psi_{nm}^{\pm} = \tfrac{1}{2}(c_{nm} \mp b_{nm})N_n^m \end{array}\right\} \quad \text{for species 1,}$$

where the normalization factor N_n^m is given by

$$N_n^m = \left[\frac{2n + 1}{2}\frac{(n - m)!}{(n + m)!}\right]^{1/2}$$

The $D_{nm}^{\pm}$ and $\psi_{nm}^{\pm}$ are those used by *Lambeck* (1988), except that Lambeck adds 180° to ψ for certain constituents like O_1 and P_1 whose amplitude in the potential expansion of *Cartwright and Tayler* (1971) is negative. Others have also used a phase angle $\varepsilon = 90° - \psi$. Table 8 lists our coefficients in this D, ψ convention for those terms that have recently been estimated through the precise tracking of artificial satellites (*e.g., Marsh et al.*, 1990).

In CR91 we discuss the harmonics of degree 2 in relation to their implied rates of tidal energy dissipation and in comparison with similar estimates

Table 2. Coefficients of O_1.

n	m	a_{nm}	b_{nm}	c_{nm}	d_{nm}
0	0	6.423		-3.685	
1	0	4.869		-18.267	
1	1	1.621	-7.434	3.366	-8.252
2	0	8.691		-12.353	
2	1	-15.747	-41.610	11.533	-33.268
2	2	16.599	2.668	-7.118	17.479
3	0	7.283		15.837	
3	1	9.576	16.476	24.185	31.418
3	2	14.837	30.911	-11.574	21.196
3	3	-33.074	-35.436	2.886	-8.137
4	0	-3.856		16.026	
4	1	-30.245	9.224	12.757	-20.133
4	2	6.781	9.021	-11.414	8.549
4	3	-6.373	-7.109	16.398	-31.154
4	4	7.852	30.303	1.954	2.513
5	0	-13.498		5.191	
5	1	17.279	-1.453	-12.562	12.811
5	2	8.074	2.626	-6.827	2.950
5	3	5.629	-7.539	-0.215	0.047
5	4	5.679	11.330	-3.537	4.161
5	5	15.550	5.789	-0.855	2.147
6	0	-7.700		4.749	
6	1	0.235	-1.127	-5.623	0.233
6	2	6.768	-4.579	0.574	5.520
6	3	-2.266	-9.941	1.193	-1.077
6	4	11.074	7.313	-5.935	4.149
6	5	0.960	7.560	2.361	4.662
6	6	-7.220	-1.055	-0.719	-3.983
7	0	-1.289		-4.998	
7	1	0.758	-0.679	-10.129	-4.609
7	2	0.327	-3.583	5.312	0.820
7	3	-7.456	2.589	-3.849	-5.772
7	4	6.068	7.049	0.296	7.041
7	5	-5.400	3.281	-3.588	-0.854
7	6	-5.980	-6.772	1.614	-5.693
7	7	7.311	-1.009	-1.612	0.123
8	0	-1.499		-8.442	
8	1	8.357	4.993	-2.736	10.055
8	2	-1.748	-0.171	3.987	1.680
8	3	-4.318	-2.556	8.497	-2.909
8	4	5.305	8.476	-1.392	4.959
8	5	-8.806	-6.106	0.597	-4.211
8	6	-8.487	-1.447	0.606	-6.996
8	7	0.432	-1.851	-0.913	2.861
8	8	3.191	-8.136	0.066	3.617

Table 3. Coefficients of P_1.

n	m	a_{nm}	b_{nm}	c_{nm}	d_{nm}
0	0	4.339		0.341	
1	0	2.813		-9.486	
1	1	1.353	-2.584	2.962	-4.268
2	0	-2.729		-4.435	
2	1	-4.522	-14.256	3.927	-15.024
2	2	10.181	0.327	-0.438	12.517
3	0	4.436		10.126	
3	1	-6.182	1.132	13.637	9.998
3	2	2.725	10.220	-0.232	17.350
3	3	-13.200	-14.972	-2.517	-11.932
4	0	0.413		3.876	
4	1	-13.111	8.873	0.281	-7.227
4	2	4.256	1.322	-5.597	2.801
4	3	-6.080	-0.610	5.812	-11.886
4	4	4.103	17.736	5.547	5.212
5	0	-8.082		-0.946	
5	1	7.135	-2.615	-5.373	5.182
5	2	4.452	-0.169	-2.992	2.334
5	3	1.061	-2.456	0.201	-1.580
5	4	1.191	2.701	-3.836	4.664
5	5	7.059	4.695	1.152	0.560
6	0	-2.630		3.039	
6	1	1.147	-1.779	-3.200	1.223
6	2	1.884	-4.648	0.577	1.942
6	3	-2.375	-5.096	-0.734	-1.103
6	4	6.361	0.344	0.519	3.453
6	5	-1.389	3.758	-1.366	2.305
6	6	-1.819	0.579	-4.790	-2.057
7	0	-0.035		-0.822	
7	1	1.554	0.871	-4.209	-1.893
7	2	-1.395	-1.943	3.597	-0.916
7	3	-2.585	0.985	-1.583	-4.014
7	4	4.098	0.995	1.149	5.058
7	5	-3.028	-0.578	-1.894	1.401
7	6	-2.036	-2.931	-0.611	-4.382
7	7	4.359	-2.228	0.533	0.840
8	0	2.549		-3.366	
8	1	4.339	1.178	-0.259	3.721
8	2	-1.485	-0.402	0.919	0.595
8	3	-3.329	-0.271	2.894	-2.763
8	4	2.646	1.588	0.952	4.352
8	5	-3.558	-2.587	-1.234	-2.697
8	6	-2.669	-0.909	0.239	-1.161
8	7	-0.019	-1.919	-0.805	3.426
8	8	1.011	-4.174	1.487	0.653

Units are millimeters.

<table>
<tr><td colspan="6" align="center">Table 4. Coefficients of K_1.</td></tr>
</table>

n	m	a_{nm}	b_{nm}	c_{nm}	d_{nm}
0	0	13.791		0.353	
1	0	8.866		-28.802	
1	1	2.508	-7.660	9.532	-13.986
2	0	-9.604		-14.703	
2	1	-12.854	-42.676	11.208	-45.238
2	2	31.138	-0.186	-1.032	38.567
3	0	13.331		31.474	
3	1	-21.039	3.302	39.674	28.776
3	2	6.491	28.839	0.196	53.202
3	3	-39.873	-44.973	-8.232	-37.442
4	0	1.880		12.224	
4	1	-38.614	27.833	0.126	-20.796
4	2	13.531	4.182	-17.338	7.734
4	3	-18.582	-1.790	16.866	-35.992
4	4	11.582	54.126	17.840	17.097
5	0	-24.332		-4.160	
5	1	21.768	-8.420	-16.458	15.317
5	2	13.758	-1.053	-9.190	6.908
5	3	2.588	-6.615	0.373	-5.212
5	4	3.881	7.064	-12.324	14.223
5	5	21.345	14.730	4.217	1.840
6	0	-8.082		9.589	
6	1	3.962	-5.982	-9.715	3.940
6	2	5.456	-14.469	1.448	5.199
6	3	-7.520	-15.453	-2.455	-3.920
6	4	19.138	0.145	2.567	10.136
6	5	-3.804	11.730	-4.686	6.979
6	6	-4.246	1.946	-15.247	-6.344
7	0	-0.415		-1.870	
7	1	4.944	2.691	-12.436	-5.782
7	2	-4.688	-5.724	10.842	-3.313
7	3	-7.873	3.337	-5.025	-12.540
7	4	12.493	2.297	3.860	15.291
7	5	-9.324	-2.758	-5.880	4.204
7	6	-5.335	-8.732	-2.147	-13.607
7	7	13.412	-7.523	2.131	2.680
8	0	8.315		-9.542	
8	1	13.244	3.760	-0.498	11.048
8	2	-4.307	-1.287	2.521	1.927
8	3	-9.822	-0.300	8.098	-8.486
8	4	7.669	3.921	3.186	13.352
8	5	-10.402	-7.759	-3.999	-8.376
8	6	-7.957	-3.043	0.710	-3.175
8	7	-0.006	-6.373	-2.448	10.674
8	8	2.567	-12.637	4.966	1.528

<table>
<tr><td colspan="6" align="center">Table 5. Coefficients of N_2.</td></tr>
</table>

n	m	a_{nm}	b_{nm}	c_{nm}	d_{nm}
0	0	0.124		-0.613	
1	0	2.347		-0.356	
1	1	-2.684	0.900	0.889	-4.602
2	0	-0.330		-2.724	
2	1	-5.427	-0.315	1.936	0.744
2	2	-9.838	-17.890	16.799	-16.710
3	0	1.807		-11.885	
3	1	7.518	4.513	11.610	-7.367
3	2	1.616	6.610	-4.544	2.724
3	3	25.920	-3.790	1.572	1.172
4	0	-12.528		5.499	
4	1	4.211	0.708	10.177	2.911
4	2	19.048	25.642	-6.994	6.637
4	3	-16.758	17.226	-2.399	10.398
4	4	-21.380	-12.878	10.398	-4.917
5	0	-6.670		10.245	
5	1	-18.060	-12.981	-13.043	-5.285
5	2	-18.941	-7.079	12.244	20.830
5	3	-11.707	-9.867	3.576	-12.201
5	4	8.180	-4.602	8.199	23.779
5	5	12.910	-13.687	-6.123	-2.481
6	0	14.584		-6.514	
6	1	-2.806	0.950	-9.253	-1.520
6	2	1.128	-14.889	5.353	-2.409
6	3	-1.457	-0.653	8.699	0.641
6	4	12.146	2.412	6.385	1.645
6	5	-3.179	8.960	-1.089	-14.114
6	6	8.130	14.598	21.618	8.964
7	0	10.444		1.792	
7	1	3.632	5.663	-0.594	4.968
7	2	3.422	-5.350	-8.075	-13.139
7	3	-8.559	-2.421	-0.531	-5.251
7	4	-1.021	-1.091	-3.435	8.477
7	5	-4.462	5.581	-5.225	13.202
7	6	-1.164	-6.762	-3.062	6.700
7	7	9.327	10.808	2.891	3.865
8	0	-1.330		3.035	
8	1	3.870	1.355	-4.851	1.686
8	2	-4.560	2.444	-4.959	-1.868
8	3	6.601	-4.516	-3.579	1.730
8	4	-2.387	-2.322	11.113	6.069
8	5	-6.043	6.228	-3.443	3.352
8	6	-4.416	2.961	-3.046	2.010
8	7	-12.205	5.693	0.784	-2.092
8	8	0.554	-1.260	-1.873	-0.146

<table>
<thead>
<tr><th colspan="6">Table 6. Coefficients of M_2.</th></tr>
<tr><th>n</th><th>m</th><th>a_{nm}</th><th>b_{nm}</th><th>c_{nm}</th><th>d_{nm}</th></tr>
</thead>
<tbody>
<tr><td>0</td><td>0</td><td>6.520</td><td></td><td>−2.747</td><td></td></tr>
<tr><td>1</td><td>0</td><td>7.320</td><td></td><td>5.956</td><td></td></tr>
<tr><td>1</td><td>1</td><td>−12.735</td><td>15.518</td><td>−9.016</td><td>−12.699</td></tr>
<tr><td>2</td><td>0</td><td>−7.225</td><td></td><td>−30.398</td><td></td></tr>
<tr><td>2</td><td>1</td><td>−24.297</td><td>6.794</td><td>−6.219</td><td>−11.706</td></tr>
<tr><td>2</td><td>2</td><td>−56.604</td><td>−73.104</td><td>86.870</td><td>−90.602</td></tr>
<tr><td>3</td><td>0</td><td>9.639</td><td></td><td>−46.005</td><td></td></tr>
<tr><td>3</td><td>1</td><td>27.096</td><td>23.199</td><td>74.606</td><td>−32.045</td></tr>
<tr><td>3</td><td>2</td><td>−1.523</td><td>23.062</td><td>−10.671</td><td>9.774</td></tr>
<tr><td>3</td><td>3</td><td>108.486</td><td>−22.920</td><td>40.788</td><td>−3.495</td></tr>
<tr><td>4</td><td>0</td><td>−40.916</td><td></td><td>23.428</td><td></td></tr>
<tr><td>4</td><td>1</td><td>1.088</td><td>−8.575</td><td>63.547</td><td>27.841</td></tr>
<tr><td>4</td><td>2</td><td>74.350</td><td>94.796</td><td>−18.889</td><td>75.479</td></tr>
<tr><td>4</td><td>3</td><td>−70.380</td><td>77.704</td><td>−52.820</td><td>71.706</td></tr>
<tr><td>4</td><td>4</td><td>−96.299</td><td>−73.162</td><td>11.401</td><td>−37.282</td></tr>
<tr><td>5</td><td>0</td><td>−19.777</td><td></td><td>22.186</td><td></td></tr>
<tr><td>5</td><td>1</td><td>−69.804</td><td>−37.849</td><td>−100.333</td><td>−45.503</td></tr>
<tr><td>5</td><td>2</td><td>−81.484</td><td>−56.592</td><td>14.114</td><td>86.186</td></tr>
<tr><td>5</td><td>3</td><td>−40.991</td><td>−25.305</td><td>9.861</td><td>−75.385</td></tr>
<tr><td>5</td><td>4</td><td>27.995</td><td>−35.100</td><td>74.224</td><td>97.607</td></tr>
<tr><td>5</td><td>5</td><td>57.708</td><td>−40.326</td><td>−23.676</td><td>−38.304</td></tr>
<tr><td>6</td><td>0</td><td>56.985</td><td></td><td>−9.897</td><td></td></tr>
<tr><td>6</td><td>1</td><td>−5.093</td><td>−1.029</td><td>−42.678</td><td>−6.807</td></tr>
<tr><td>6</td><td>2</td><td>−15.925</td><td>−65.591</td><td>44.290</td><td>−39.668</td></tr>
<tr><td>6</td><td>3</td><td>−20.135</td><td>0.184</td><td>46.227</td><td>−3.366</td></tr>
<tr><td>6</td><td>4</td><td>30.601</td><td>−0.888</td><td>36.936</td><td>12.123</td></tr>
<tr><td>6</td><td>5</td><td>−11.485</td><td>54.338</td><td>-6.474</td><td>−55.435</td></tr>
<tr><td>6</td><td>6</td><td>9.580</td><td>56.721</td><td>111.845</td><td>78.788</td></tr>
<tr><td>7</td><td>0</td><td>33.830</td><td></td><td>33.420</td><td></td></tr>
<tr><td>7</td><td>1</td><td>20.385</td><td>17.801</td><td>10.123</td><td>35.489</td></tr>
<tr><td>7</td><td>2</td><td>28.298</td><td>−0.382</td><td>−36.705</td><td>−59.548</td></tr>
<tr><td>7</td><td>3</td><td>−32.679</td><td>−14.754</td><td>−19.272</td><td>−26.310</td></tr>
<tr><td>7</td><td>4</td><td>−3.001</td><td>−27.161</td><td>−9.241</td><td>36.102</td></tr>
<tr><td>7</td><td>5</td><td>−12.942</td><td>6.652</td><td>−32.701</td><td>74.351</td></tr>
<tr><td>7</td><td>6</td><td>−7.486</td><td>−42.845</td><td>−8.875</td><td>19.921</td></tr>
<tr><td>7</td><td>7</td><td>48.794</td><td>43.414</td><td>31.749</td><td>28.019</td></tr>
<tr><td>8</td><td>0</td><td>−7.415</td><td></td><td>12.428</td><td></td></tr>
<tr><td>8</td><td>1</td><td>31.814</td><td>7.927</td><td>−23.788</td><td>5.829</td></tr>
<tr><td>8</td><td>2</td><td>−14.743</td><td>15.690</td><td>−36.526</td><td>−14.510</td></tr>
<tr><td>8</td><td>3</td><td>34.484</td><td>−23.014</td><td>−14.665</td><td>7.803</td></tr>
<tr><td>8</td><td>4</td><td>−28.656</td><td>−19.711</td><td>43.145</td><td>24.483</td></tr>
<tr><td>8</td><td>5</td><td>−19.204</td><td>22.334</td><td>−28.312</td><td>31.960</td></tr>
<tr><td>8</td><td>6</td><td>−12.206</td><td>5.368</td><td>−23.358</td><td>2.721</td></tr>
<tr><td>8</td><td>7</td><td>−58.555</td><td>21.136</td><td>−17.010</td><td>1.044</td></tr>
<tr><td>8</td><td>8</td><td>19.809</td><td>−5.813</td><td>−10.962</td><td>−7.817</td></tr>
</tbody>
</table>

<table>
<thead>
<tr><th colspan="6">Table 7. Coefficients of S_2.</th></tr>
<tr><th>n</th><th>m</th><th>a_{nm}</th><th>b_{nm}</th><th>c_{nm}</th><th>d_{nm}</th></tr>
</thead>
<tbody>
<tr><td>0</td><td>0</td><td>3.374</td><td></td><td>3.269</td><td></td></tr>
<tr><td>1</td><td>0</td><td>4.664</td><td></td><td>2.571</td><td></td></tr>
<tr><td>1</td><td>1</td><td>−2.498</td><td>7.825</td><td>−0.167</td><td>0.292</td></tr>
<tr><td>2</td><td>0</td><td>11.213</td><td></td><td>−7.474</td><td></td></tr>
<tr><td>2</td><td>1</td><td>−5.644</td><td>9.722</td><td>−4.194</td><td>1.099</td></tr>
<tr><td>2</td><td>2</td><td>−23.047</td><td>−19.205</td><td>38.661</td><td>−21.652</td></tr>
<tr><td>3</td><td>0</td><td>6.892</td><td></td><td>−26.029</td><td></td></tr>
<tr><td>3</td><td>1</td><td>−9.660</td><td>9.082</td><td>27.785</td><td>−0.534</td></tr>
<tr><td>3</td><td>2</td><td>−5.958</td><td>13.594</td><td>−22.113</td><td>−4.515</td></tr>
<tr><td>3</td><td>3</td><td>21.705</td><td>0.721</td><td>26.562</td><td>−14.133</td></tr>
<tr><td>4</td><td>0</td><td>−28.155</td><td></td><td>2.737</td><td></td></tr>
<tr><td>4</td><td>1</td><td>−8.734</td><td>−12.709</td><td>26.185</td><td>−5.349</td></tr>
<tr><td>4</td><td>2</td><td>37.375</td><td>9.557</td><td>−4.417</td><td>31.725</td></tr>
<tr><td>4</td><td>3</td><td>3.252</td><td>7.504</td><td>−20.393</td><td>44.780</td></tr>
<tr><td>4</td><td>4</td><td>−20.990</td><td>−29.871</td><td>−7.898</td><td>−30.279</td></tr>
<tr><td>5</td><td>0</td><td>−2.756</td><td></td><td>21.254</td><td></td></tr>
<tr><td>5</td><td>1</td><td>−1.100</td><td>−0.981</td><td>−47.657</td><td>−16.770</td></tr>
<tr><td>5</td><td>2</td><td>−17.797</td><td>−25.752</td><td>5.908</td><td>30.786</td></tr>
<tr><td>5</td><td>3</td><td>−18.360</td><td>14.777</td><td>11.005</td><td>−29.203</td></tr>
<tr><td>5</td><td>4</td><td>−17.051</td><td>−12.240</td><td>23.998</td><td>50.654</td></tr>
<tr><td>5</td><td>5</td><td>28.951</td><td>3.534</td><td>−22.061</td><td>−10.434</td></tr>
<tr><td>6</td><td>0</td><td>19.850</td><td></td><td>−2.247</td><td></td></tr>
<tr><td>6</td><td>1</td><td>5.445</td><td>6.059</td><td>−18.304</td><td>2.912</td></tr>
<tr><td>6</td><td>2</td><td>−23.504</td><td>−13.049</td><td>5.107</td><td>−27.751</td></tr>
<tr><td>6</td><td>3</td><td>−19.845</td><td>−0.550</td><td>3.326</td><td>11.428</td></tr>
<tr><td>6</td><td>4</td><td>8.190</td><td>−4.832</td><td>4.634</td><td>−4.820</td></tr>
<tr><td>6</td><td>5</td><td>−9.713</td><td>27.483</td><td>8.027</td><td>−20.275</td></tr>
<tr><td>6</td><td>6</td><td>−19.454</td><td>−4.257</td><td>37.629</td><td>44.844</td></tr>
<tr><td>7</td><td>0</td><td>−2.808</td><td></td><td>8.776</td><td></td></tr>
<tr><td>7</td><td>1</td><td>2.416</td><td>−2.663</td><td>6.438</td><td>10.629</td></tr>
<tr><td>7</td><td>2</td><td>13.437</td><td>11.666</td><td>−9.943</td><td>−16.182</td></tr>
<tr><td>7</td><td>3</td><td>−10.349</td><td>−3.113</td><td>−12.029</td><td>−25.536</td></tr>
<tr><td>7</td><td>4</td><td>2.044</td><td>−10.613</td><td>−4.555</td><td>2.185</td></tr>
<tr><td>7</td><td>5</td><td>−0.261</td><td>−8.221</td><td>−14.512</td><td>24.055</td></tr>
<tr><td>7</td><td>6</td><td>−5.307</td><td>−12.561</td><td>−7.946</td><td>−10.137</td></tr>
<tr><td>7</td><td>7</td><td>8.356</td><td>12.098</td><td>22.316</td><td>15.170</td></tr>
<tr><td>8</td><td>0</td><td>−0.156</td><td></td><td>8.046</td><td></td></tr>
<tr><td>8</td><td>1</td><td>16.608</td><td>−0.693</td><td>0.276</td><td>1.876</td></tr>
<tr><td>8</td><td>2</td><td>3.131</td><td>6.705</td><td>−13.693</td><td>−6.271</td></tr>
<tr><td>8</td><td>3</td><td>19.426</td><td>−10.977</td><td>0.925</td><td>−0.333</td></tr>
<tr><td>8</td><td>4</td><td>−12.510</td><td>−12.454</td><td>7.358</td><td>5.245</td></tr>
<tr><td>8</td><td>5</td><td>0.515</td><td>−1.337</td><td>−14.901</td><td>14.836</td></tr>
<tr><td>8</td><td>6</td><td>1.686</td><td>−0.975</td><td>−8.086</td><td>0.032</td></tr>
<tr><td>8</td><td>7</td><td>−16.761</td><td>0.108</td><td>−14.250</td><td>1.701</td></tr>
<tr><td>8</td><td>8</td><td>16.856</td><td>1.118</td><td>4.850</td><td>−2.800</td></tr>
</tbody>
</table>

Table 8: Some selected harmonic coefficients.

Tide	n	m	D_{nm}^+ (cm)	ψ_{nm}^+	Tide	n	m	D_{nm}^+ (cm)	ψ_{nm}^+
O_1	2	1	2.33	42.7	N_2	2	2	0.70	127.4
	3	1	1.13	280.6		3	2	0.10	291.3
	4	1	1.20	86.0		4	2	0.23	308.2
	5	1	0.69	249.7		5	2	0.08	84.4
	6	1	0.09	185.9		6	2	0.06	93.6
	7	1	0.19	157.8		7	2	0.03	195.7
	8	1	0.34	247.2		8	2	0.02	229.0
P_1	2	1	0.86	47.1	M_2	2	2	3.51	132.6
	3	1	0.35	343.0		3	2	0.30	283.7
	4	1	0.52	112.9		4	2	1.05	322.8
	5	1	0.27	257.4		5	2	0.29	86.2
	6	1	0.05	239.0		6	2	0.38	116.8
	7	1	0.09	176.2		7	2	0.12	229.3
	8	1	0.14	259.9		8	2	0.12	240.7
K_1	2	1	2.56	47.2	S_2	2	2	1.18	127.7
	3	1	1.00	348.0		3	2	0.32	253.6
	4	1	1.55	115.0		4	2	0.39	348.6
	5	1	0.81	257.8		5	2	0.14	67.7
	6	1	0.17	244.7		6	2	0.17	160.5
	7	1	0.28	176.8		7	2	0.05	262.8
	8	1	0.42	260.1		8	2	0.04	261.2

from other models. As a minor detail, we point out in particular that the *in-phase* component of the $(2,2)$ harmonic, namely $D_{22}^+ \cos \psi_{22}^+$, may be in error by $0.01 \times$ the potential amplitude divided by g, on account of the subtraction of the body tide with an older version of the Love number h_2 (0.619 instead of the modern 0.609). The difference in M_2 caused by this correction is less than 1 mm, significant in comparison with D_{22}^+ itself, but negligible in a general comparison of tidal amplitudes. We have not applied this correction to the values listed in Tables 2–8; however, the correction was applied to M_2 and S_2 in Table 5 of CR91.

REFERENCES

Bogdanov, K. T. and V. P. Nefedyev, New cotidal charts in the Australasian seas, *Doklady Akad. Nauk, SSSR*, **141**, 1078–1081, 1961. (1255–1257 in English transl.) *and* **144**, 1034–1037, 1962. (14–16 in English transl.).

Born, G. H., J. L. Mitchell and G. A. Heyler, Geosat ERM—mission design, *J. Astronaut. Sci.*, **35**, 119–134, 1987.

Brenner, A. C., C. J. Koblinsky, and B. D. Beckley, A preliminary estimate of geoid-induced variations in repeat-orbit satellite altimeter observations, *J. Geophys. Res.*, **95**, 3033–3040, 1990.

Cartwright, D. E. and A. C. Edden, Corrected tables of tidal harmonics, *Geophys. J. R. astr. Soc.*, **33**, 253–264, 1973.

Cartwright, D. E. and R. D. Ray, New estimates of oceanic tidal energy dissipation from satellite altimetry, *Geophys. Res. Lett.*, **16**, 73–76, 1989.

Cartwright, D. E. and R. D. Ray, Oceanic tides from Geosat altimetry, *J. Geophys. Res.*, **95**, 3069–3090, 1990.

Cartwright, D. E. and R. D. Ray, Energetics of global ocean tides from Geosat altimetry, *J. Geophys. Res.*, in press, 1991.

Cartwright, D. E. and R. J. Tayler, New computations of the tide-generating potential, *Geophys. J. R. astr. Soc.*, **23**, 45–73, 1971.

Choi, B.-H., Tidal model of the Yellow Sea and the East China Sea, Korea Ocean Res. Dev. Inst. Rept. 80-02, 72 pp., 1980.

Defant, A., *Physical Oceanography*, vol. 2, Pergamon Press, Oxford, 1961.

Dressler, R., Hydrodynamisch-numerische Untersuchungen der M_2 Gezeit und einiger Tsunamis im europäischen Mittelmeer, Mitteilungen d. Inst. f. Meereskunde, Universität Hamburg, Nr. 23, 27 pp., 1980.

Farrell, W. E., Deformation of the Earth by surface loads, *Rev. Geophys. Space Phys.*, **10**, 761–797, 1972.

Francis, O. and P. Mazzega, Global charts of ocean tide loading effects, *J. Geophys. Res.*, **95**, 11411–11424, 1990.

Groves, G. W. and R. W. Reynolds, An orthogonalized convolution method of tide prediction, *J. Geophys. Res.*, **80**, 4131–4138, 1975.

Haines, B. J., G. H. Born, G. W. Rosborough, J. G. Marsh, and R. G. Williamson, Precise orbit computation for the Geosat Exact Repeat Mission, *J. Geophys. Res.*, **95**, 2871–2885, 1990.

Lambeck, K., *Geophysical Geodesy: The Slow Deformations of the Earth*, Clarendon Press, Oxford, 1988.

Marsh, J. G. and 16 co-authors, The GEM-T2 gravitational model, *J. Geophys. Res.*, **95**, 22043–22071, 1990.

Parke, M. E. and M. C. Hendershott, M_2, S_2, K_1 models of the global ocean tide on an elastic earth, *Marine Geod.*, **3**, 379–407, 1980.

Ray, R. D. and C. J. Koblinsky, On the sea-state bias of the Geosat altimeter, *J. Atmos. Oceanic Tech.*, **8**, 397–408, 1991.

Ray, R. D., C. J. Koblinsky, and B. D. Beckley, On the effectiveness of Geosat altimeter corrections, *Int. J. Remote Sensing*, in press, 1991.

Ray, R. D. and B. V. Sanchez, Radial deformation of the Earth by oceanic tidal loading, NASA Tech. Memo. 100743, 49 pp., 1989.

Schureman, P., Manual of harmonic analysis and prediction of tides, Spec. Pub. 98, revised edition, U. S. Dept. Commerce, 1940; reprinted 1988.

Schwiderski, E. W., Atlas of ocean tidal charts and maps: M_2, S_2, K_1, N_2, P_1, K_2, Mf Tech. Repts., Naval Surface Weapons Center, Dahlgren, Va, 1983.

Ye, A. L. and I. S. Robinson, Tidal dynamics in the South China Sea, *Geophys. J. R. astr. Soc.*, **72**, 691–707, 1983.

Plate Captions

Plate 1: Differences (cm) between the present Geosat-derived ocean tide and the *Schwiderski* (1983) model, for the M_2 constituent. (Top) In-phase component $H \cos G$; (bottom) quadrature component $H \sin G$. Each color spans an interval of 5 cm. Differences on the Patagonian Shelf exceed 50 cm.

Plate 2: As for Plate 1, but for the O_1 constituent. Each color spans an interval of 2 cm.
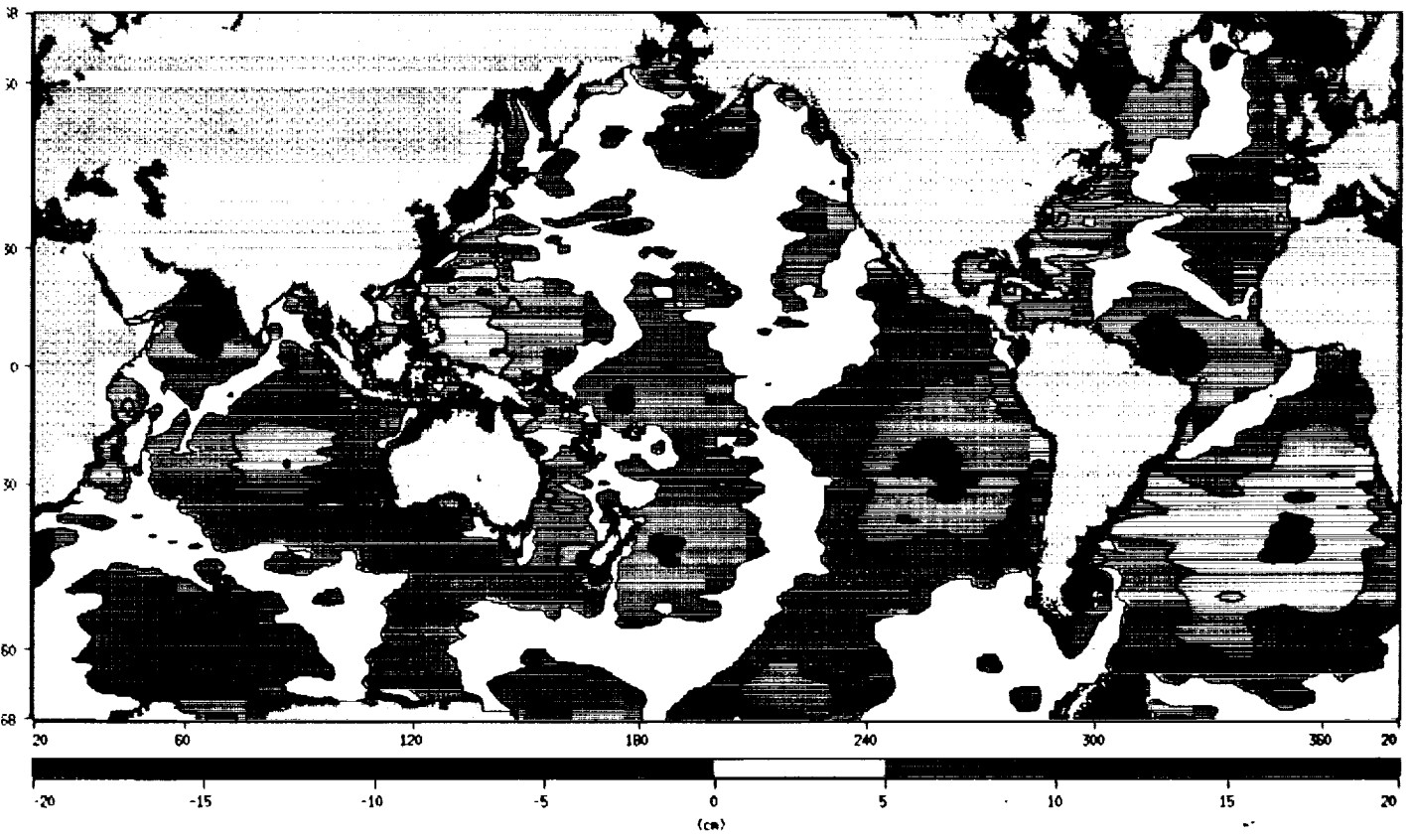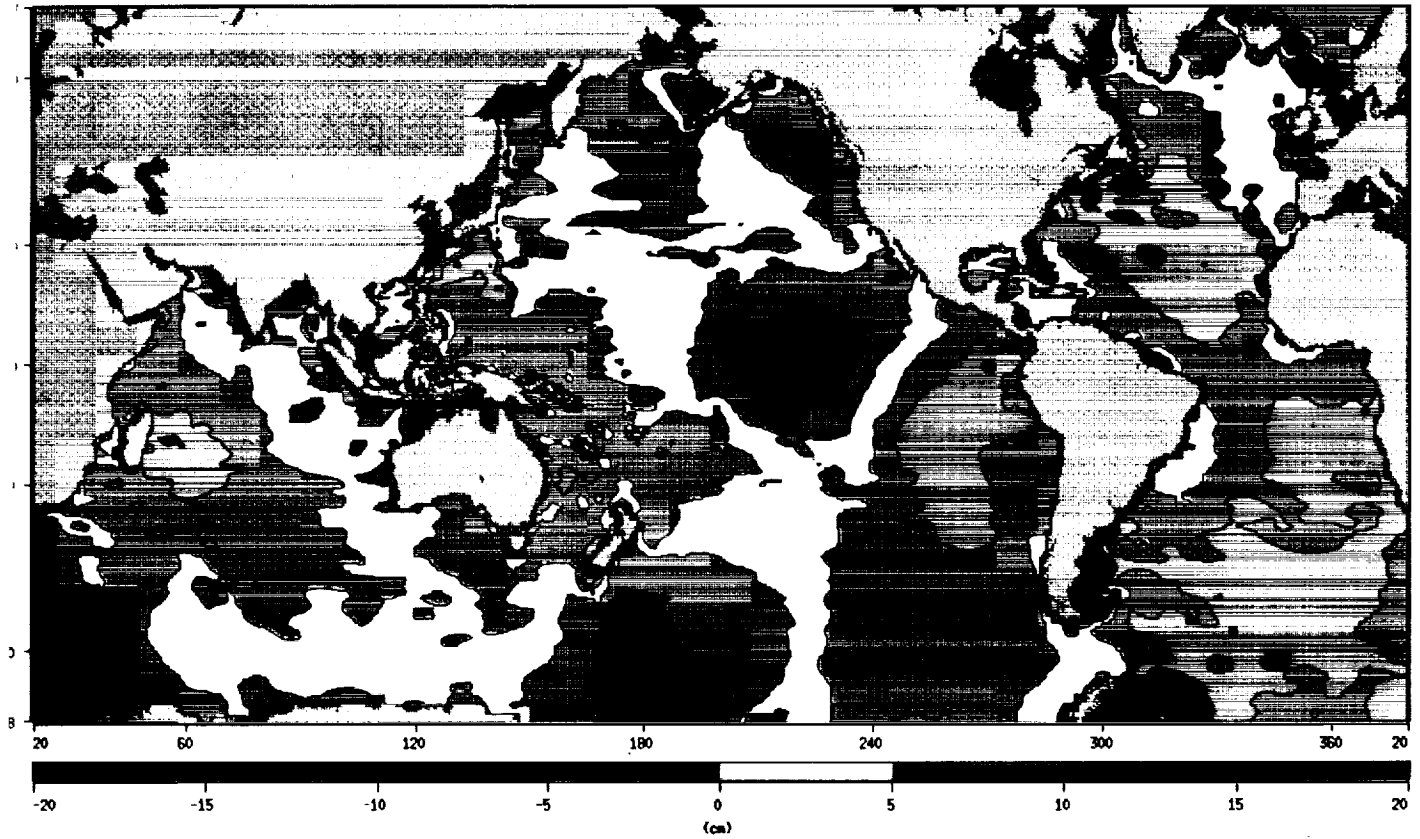
Plate 1

Plate 2
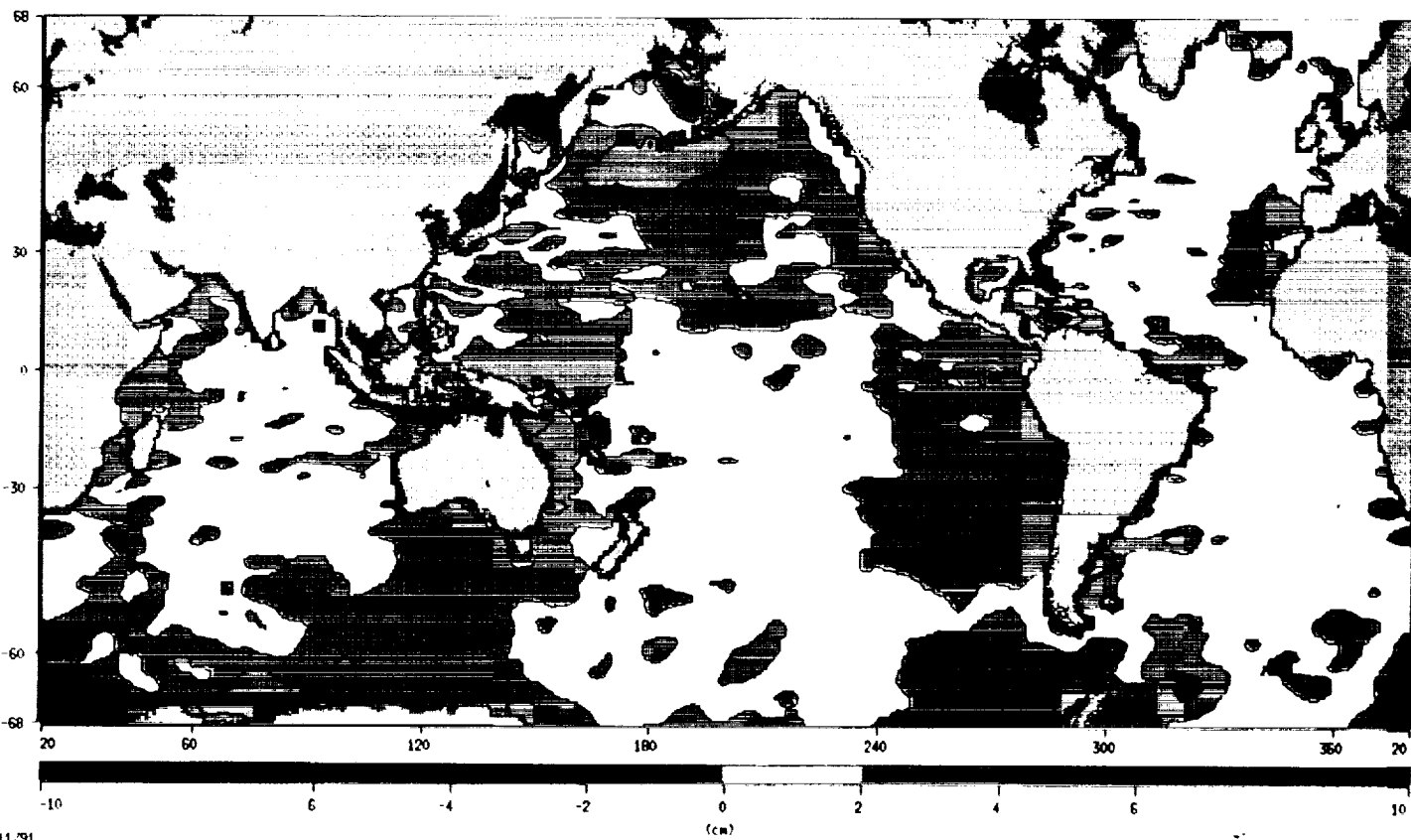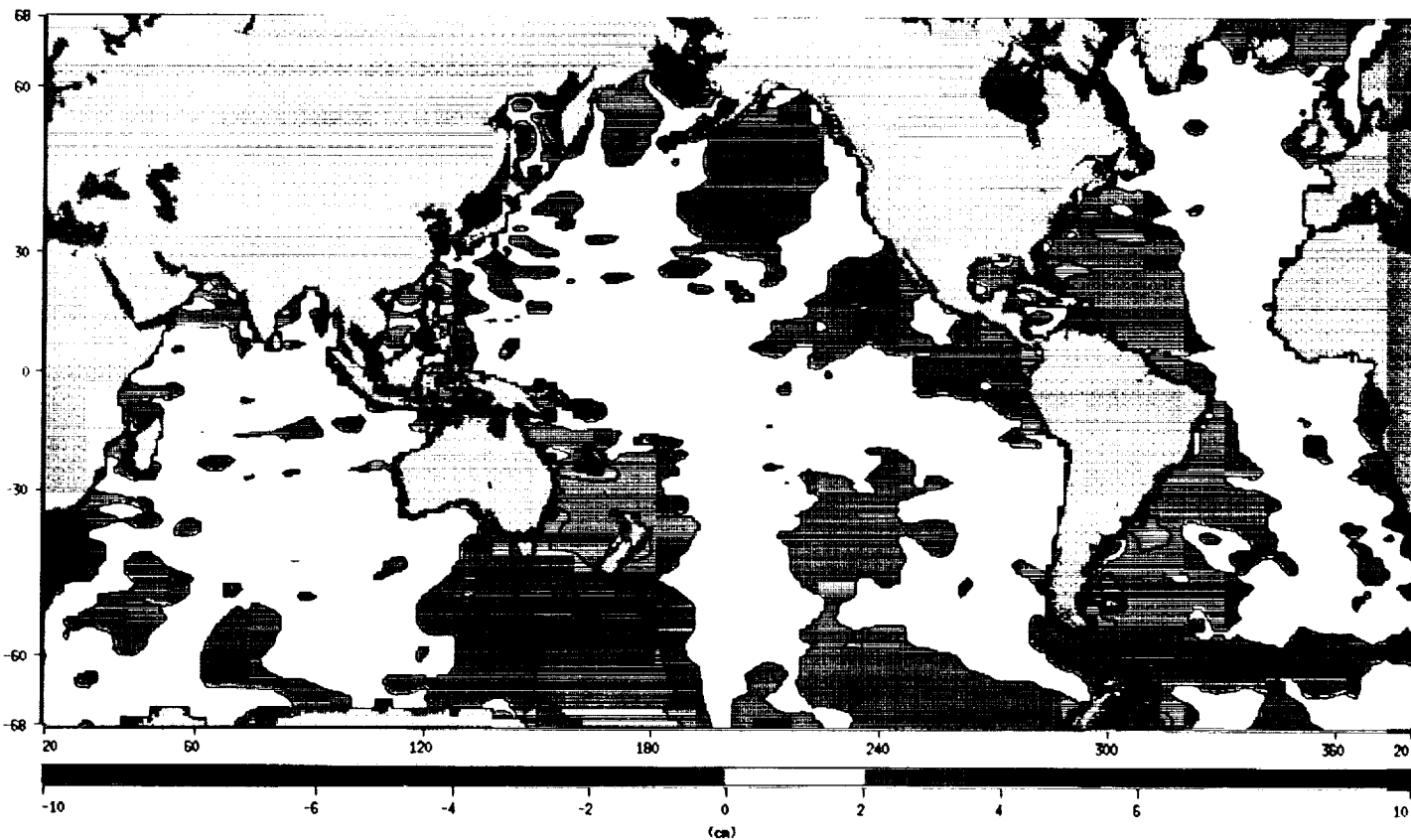
Report Documentation Page

1. Report No. NASA TM 104544	2. Government Accession No.	3. Recipient's Catalog No.

4. Title and Subtitle Oceanic Tide Maps and Spherical Harmonic Coefficients from Geosat Altimetry		5. Report Date July 1991
		6. Performing Organization Code 926.0

7. Author(s) D.E. Cartwright, R.D. Ray, and B.V. Sanchez		8. Performing Organization Report No. 91B00073
		10. Work Unit No.

9. Performing Organization Name and Address Goddard Space Flight Center Greenbelt, Maryland 20771		11. Contract or Grant No.
		13. Type of Report and Period Covered Technical Memorandum

12. Sponsoring Agency Name and Address National Aeronautics and Space Administration Washington, D.C. 20546-0001		14. Sponsoring Agency Code

15. Supplementary Notes

D.E. Cartwright and R.D. Ray: ST Systems Corporation, Lanham Maryland.
B.V. Sanchez: NASA/GSFC, Greenbelt, Maryland.

16. Abstract

This report presents maps and tables for the global ocean tides, 69° N to 68° S, derived from two years of Geosat altimetry. It supplements a paper by Cartwright and Ray which examines the energetics implied by the same data. Global maps of local and Greenwich admittance of the (altimetric) ocean tide, and maps of amplitude and Greenwich phase lag of the ocean tide are shown for M_2, S_2, N_2, O_1, and K_1. Larger scale maps of amplitude and phase are also shown for regional areas of special interest. Spherical harmonic coefficients of the ocean tide through degree and order 8 are tabulated for the six major constituents.

17. Key Words (Suggested by Author(s)) Tides, Ocean Tides, Geosat, Satellite Altimetry	18. Distribution Statement Unclassified - Unlimited Subject Category 47

19. Security Classif. (of this report) Unclassified	20. Security Classif. (of this page) Unclassified	21. No. of pages 75	22. Price

NASA FORM 1626 OCT 86